ADVANCED ENERGY MATERIALS
www.advenergymat.de

Recent Developments in Single-Atom Engineering Ir/Ru-Based Catalysts for the Oxygen Evolution Reaction in Acidic Media

*Qisheng Zeng, Jialin Tang, Yuan Ji, Qiu Jiang, and Chuan Xia**

Proton exchange membrane water electrolysis (PEMWE) is a critical technology for sustainable green hydrogen production, yet its efficiency and cost are severely constrained by the kinetically sluggish kinetics and material instability of the anodic oxygen evolution reaction (OER) in acidic media. Iridium (Ir)- and ruthenium (Ru)-based oxides remain the benchmark catalysts for this demanding reaction, but still face significant challenges such as the high cost and inadequate activity of Ir and the poor stability of Ru under harsh anodic conditions. In this review, recent breakthroughs in overcoming these limitations are comprehensively summarized through the strategic engineering of Ir- and Ru-based electrocatalysts via single-atom doping (SAD). Controllable synthetic methods for SAD Ir/Ru-based catalyst design are summarized, and their underlying reaction mechanisms in the acidic OER are discussed. This single-atom engineering method, as a promising strategy, shows exceptional potential and reliability for developing high-performance and durable Ir/Ru-based acidic OER catalysts, paving the way for more efficient and economically viable PEMWE systems.

1. Introduction

Proton exchange membrane water electrolysis (PEMWE) stands as a pivotal technology for sustainable, high-purity green hydrogen production, offering advantages such as rapid response, high efficiency, and compact system design.[1–5] However, the widespread commercialization of PEMWE is significantly impeded by the sluggish kinetics and harsh corrosion conditions of the anode oxygen evolution reaction (OER) in acidic environments.[6–9] Iridium oxide (IrO_2) and ruthenium oxide (RuO_2) represent state-of-the-art electrocatalysts for the acidic OER because of their inherent activities.[10–13] IrO_2 is stable under acidic oxidative conditions but suffers from relatively low intrinsic activity and, critically, extreme scarcity, leading to prohibitive costs (over US$60 000 kg^{-1}).[14–18] Conversely, RuO_2 demonstrates superior intrinsic activity but undergoes severe dissolution and structural degradation during prolonged OER operation, resulting in poor durability.[19–22] This fundamental trade-off between activity, stability, and cost represents the primary bottleneck for high-performance, economically viable PEMWE systems.

To address the limitations of conventional IrO_2 and RuO_2 catalysts, extensive research has focused on various optimization strategies (**Figure 1**).[23] These include the following: 1) Nanostructuring (e.g., nanoparticles, nanowires, and porous materials) to increase the electrochemically active surface area;[19,24–30] 2) Surface functionalization (e.g., defect sites or vacancies, adsorbates);[31] 3) Constructing an Ir/Ru single-atom catalyst (SAC)[32–36] to reduce noble metal usage; 4) Developing supported catalysts by employing conductive corrosion-resistant supports (e.g., doped MnO_2, CeO_2, TiO_2 and TaB_2), enhancing dispersion and stability;[37–42] 5) Bulk alloying Ir/Ru with other metals (e.g., intermetallic compounds/binary or ternary alloys[24,43–45] and high-entropy alloys (HEAs)[46–51]) enhances metal interactions; 6) Heteroatom doping (e.g., Ir–O–Sn, Ru–O–Co, and Ru–O–Ta) to form mixed solid solution materials.[52–58] Among these approaches, heteroatom doping enables atomic-scale tuning of electronic, chemical, and structural properties throughout entire bulk materials.[59–61] Compared with introducing defects, which can sometimes accelerate corrosion,[21,62] or constructing alloys,[43,47] which may introduce less stable elements prone to leaching, doping minimizes detrimental phase segregation and maintains structural integrity. Furthermore, unlike porous materials with inherently high surface areas but potentially compromised stability,[63,64] doping reinforces the bulk catalyst framework without sacrificing robustness, achieving a superior balance between activity and long-term durability. This targeted modification offers unparalleled synergy between precision, stability, and scalability, making it indispensable for OER applications requiring intrinsic electronic/chemical modifications. However, conventional heteroatom doping often results in non-uniform dopant aggregation and phase

Q. Zeng, Q. Jiang, C. Xia
Yangtze Delta Region Institute (Huzhou)
University of Electronic Science and Technology of China
Huzhou, Zhejiang 313001, P. R. China
E-mail: chuan.xia@uestc.edu.cn
J. Tang, Y. Ji, Q. Jiang, C. Xia
School of Materials and Energy
University of Electronic Science and Technology of China
Chengdu, Sichuan 611731, P. R. China

The ORCID identification number(s) for the author(s) of this article can be found under https://doi.org/10.1002/aenm.202504414

DOI: 10.1002/aenm.202504414

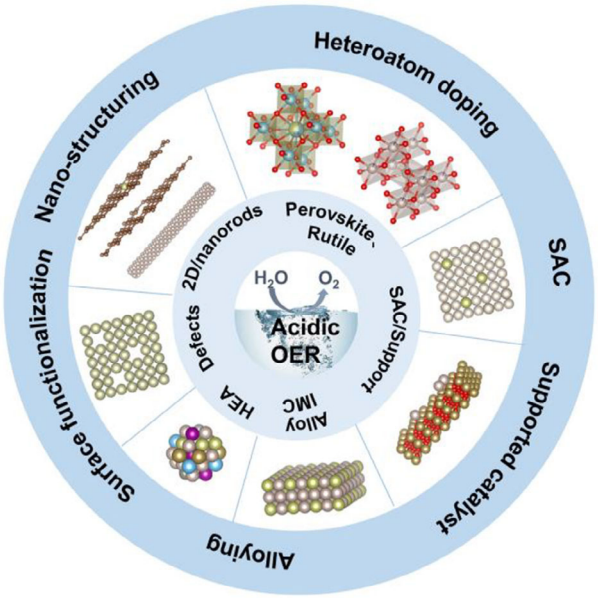

Figure 1. Schematic diagram of the mainstream modulation strategies of Ir- or Ru-based electrocatalysts for enhancing acidic OER performance.

segregation, limiting the exposure and utilization efficiency of the active sites. Furthermore, owing to the complexity and heterogeneity of this doped structure, elucidating the reaction mechanism of the catalyst remains challenging.[65]

In recent years, single-atom doping (SAD) through the precise incorporation of isolated heteroatoms into host oxides or alloy materials has emerged as a highly promising strategy to transcend these limitations.[66–73] This approach fundamentally differs from traditional bulk doping by creating well-defined, atomically dispersed active sites with unique coordination environments and strong metal-oxygen interactions,[65,73–76] which enables localized electronic structure modulation of the active centers and enhanced atom utilization efficiency (**Figure 2**).[77–79] Owing to these properties, this approach has been widely applied in electrocatalysis, driving reactions such as the hydrogen evolution reaction (HER),[80–85] CO_2/CO reduction reaction,[86] oxygen reduction reaction (ORR),[76,87] electrochemical NH_3 synthesis (NO_3RR)[88] and diverse electrocatalytic reactions.[78,89–91] This review comprehensively summarizes recent progress in SAD-engineered Ir/Ru-based catalysts for high-performance acidic OER. In this review, we begin by outlining synthetic methodologies, with an emphasis on advanced strategies for fabricating complex materials that incorporate single atoms in a controlled manner. We then explore the design principles for Ir/Ru-based single-atom doped (SAD) catalysts used in the acidic OER, focusing on the selection of doping elements to provide actionable insights for the rational design of high-performance SAD electrocatalysts. Subsequently, we delve into the mechanisms underlying performance enhancement, clarifying how single-atom doping improves both catalytic activity and stability. Finally, we address practical applications by summarizing key factors that influence the performance of PEM systems—including not only the catalysts but also other critical components such as the catalyst layer, porous transport layer, and gas/liquid interfaces. This section underscores the importance of bridging the gap between laboratory research and industrial implementation to accelerate the commercialization of PEM water electrolysis.

2. Synthesis Methods for SAD Ir- or Ru-Based OER Electrocatalysts

Ir/Ru-based oxides have garnered significant attention as OER catalysts because of their high activity and exceptional stability in acidic media. The synthesis methods for these catalysts are diverse, with the choice depending on the target structure (e.g., nanoparticles, porous catalysts, and supported catalysts), specific surface area, crystallinity, and metal atom utilization efficiency.[92,93] Current mainstream synthesis methods include conventional calcination, the molten salt method, the hydrothermal method, the impregnation method, the sol-gel method, the electrodeposition method, and the rapid thermal processing (RTP) (an emerging method). Research indicates that these methods are generally applicable for preparing reported SAD-type catalysts.[68,69,94–96] In this section, we classify these methods into three distinct classifications (**Table 1**) and highlight their respective characteristics with respect to representative studies, aiming to provide a systematic overview of current synthetic methodologies while motivating further exploration of more innovative and efficient strategies in this field.

2.1. Calcination Methods

2.1.1. Conventional Calcination Method

Conventional calcination remains a cornerstone method for heteroatom doping, particularly for bulk oxide material production and applications demanding thermally stable, crystalline doped materials. It enables the synthesis of diverse compounds with tunable compositions and morphologies by varying precursor types and calcination conditions. Precise control over the reaction parameters (e.g., raw materials, temperature, and atmospheric conditions) enables the transformation of precursor materials into atomically dispersed metal species, making it ideal for SAD catalyst synthesis.[67,97–100,113] For example, Harzandi et al. reported the synthesis of a Ru core–shell structure regulated by Ni single-atom dopants (Ni–Ru@RuO_x) via calcination at 400 °C for 2 h.[67] This catalyst achieved a high single-atom Ni loading of 16.3 wt.% and demonstrated long-term OER stability exceeding 200 h. Although effective in producing catalysts with high loading and thermal stability, prolonged thermal treatment can induce particle sintering and agglomeration, thereby reducing the surface area. To mitigate these limitations, conventional synthesis methods are often combined with strategies such as constructing single-atom alloy precursors[100] or employing carbon supports[14] to prevent undesirable particle aggregation, ensuring high atomic dispersion.

2.1.2. Molten Salt Method

The molten salt method is a versatile and efficient synthesis technique that overcomes high-temperature phase transition

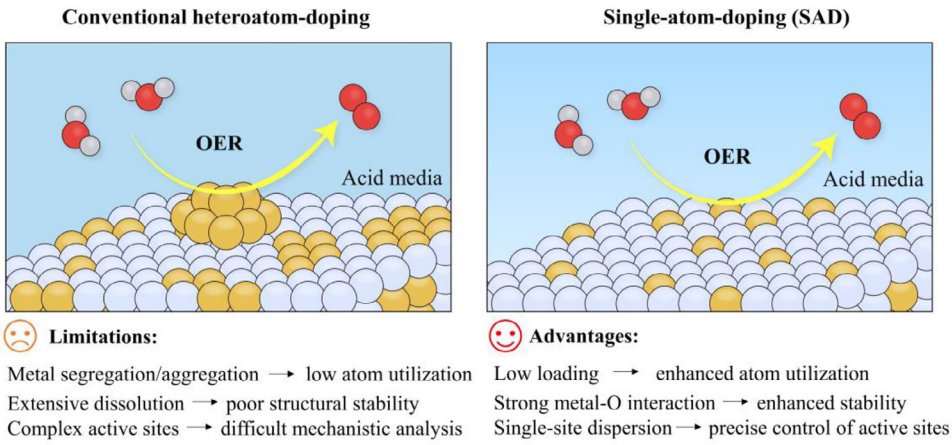

Figure 2. Comparisons of two types of metal doping strategies for acidic OER applications: conventional heteroatom doping and single-atom doping (SAD).

limitations by using molten salts as solvents and/or reaction promoters, which facilitates reactant mixing and diffusion, resulting in high-quality and phase structures.[114,115] This method enables reactions and crystal growth to occur at relatively low temperatures (<500 °C), such as when low-melting salts (e.g., $NaNO_3$ or KNO_3) are used as solvents,[23,94,69,95,116–119] lowering the processing temperature required by conventional solid-state methods.[120–122] Following this method, Wang et al. successfully synthesized tantalum (Ta) single-atom-doped RuO_2 (Ta–RuO_2, Ta: 2.5 wt.%) using molten $NaNO_3$ as the solvent at a processing temperature of 350 °C (**Figure 3a**).[69] High-resolution transmission electron microscopy (HRTEM) images (Figure 3b,c) revealed the existence of short-range ordered Ta atoms and isolated Ta atoms, indicating the high dispersion of incorporated Ta by substitutional doping. This finding indicates that the molten salt method allows a high dispersion

Table 1. Summary of the synthesis methods of representative SAD Ir- or Ru-based OER electrocatalysts.

Classification	Synthesis methods	Catalysts	Doping content	Refs.
Calcination methods	Conventional calcination method	Mn(SAs)–Ru/RuO_2	2.26 wt.%	[97]
		Ga–RuO_2	6.8 at.%	[98]
		Ni–Ru@RuO_x		[67]
		Ni–RuO_2	–	[99]
		Bi–RuO_2 SAAO	–	[100]
	Molten salt methods	$Zr_{0.01}W_{0.10}Ru_{0.89}O_x$	1 wt.%	[94]
		Ta–RuO_2	2.5 wt.%	[69]
		$Re_{0.06}Ru_{0.94}O_2$	–	[95]
		PdCo–RuO_2	Pd:0.9 wt.% Co: 0.38 wt.%	[101]
		$Nb_{0.05}Ir_{0.95}O_2$	5 wt.%	[96]
		$H_{3.8}Ir_{1-x}Ru_xO_4$	1.12 ± 0.13 at.%	[68]
Wet chemical methods	Hydrothermal method	C, Ta–RuO_2	15.62 wt.%	[102]
		V_n–RuO_2	2.25 at.%	[77]
		Co_{SA}–RuO_2–NUCN	–	[103]
		SS Pt–RuO_2 HNSs	2%	[104]
		Pt–RuO_2	0.94 at.%	[105]
	Sol-gel method	$Nb_{0.1}Ru_{0.9}O_2$	13.44 at.%	[106]
		a/c–RuO_2	0.1 wt.%	[107]
		Sb–RuO_2	–	[70]
	Co-precipitation method	LaRuIr	1.03 wt.%	[108]
		IrO_x/Ti	1.92 wt.%	[109]
	Electrochemical deposition method	RuSiW	–	[110]
Ultrafast synthesis methods	Thermal shock	Co–Ru@RuO_2	Ru:Co = 9.53:1	[111]
	Laser irradiation	Ag_1/IrO_x	6.5 at.%	[112]

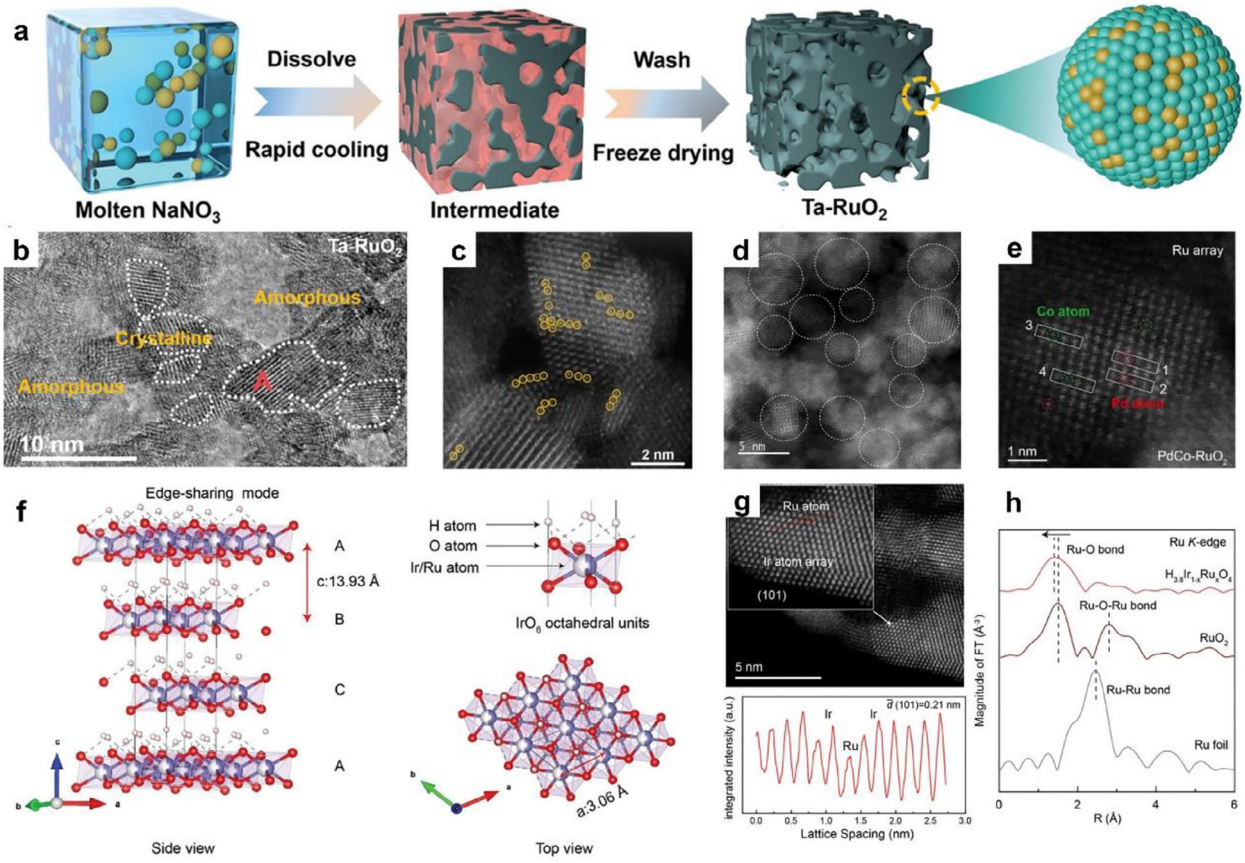

Figure 3. Representative studies of molten salt methods. a) Scheme diagram of the synthetic route of Ta–RuO_2. b) HRTEM image revealing that the amorphous and crystalline domains coexist in Ta–RuO_2. c) Aberration-corrected HAADF-STEM image of Ta–RuO_2. d) HAADF–STEM image of PdCo–RuO_2. e) Magnified HAADF-STEM image with an elemental line scanning profile confirming the incorporation of Pd and Co. f) Crystal structure diagram of $H_{3.8}Ir_{1-x}Ru_xO_4$. g) HAADF-STEM images with corresponding intensity analysis for $H_{3.8}Ir_{1-x}Ru_xO_4$. h) FT-EXAFS spectra at the Ru *K*-edge for $H_{3.8}Ir_{1-x}Ru_xO_4$ and the comparison samples.

of dopants in the host lattice owing to its relatively low synthesis temperature and faster nucleation rates, showing great potential for producing SAD catalysts. In another recent report, Tang et al. successfully achieved dual doping of RuO_2 using a mixture of molten $NaNO_3$ and KNO_3. The team revealed that both the incorporated palladium (Pd) and cobalt (Co) are highly monodisperse within the RuO_2 lattice (PdCo–RuO_2, Pd: 0.9 wt.%, Co: 0.38 wt.%) (Figure 3d,e),[101] indicating the potential of this method for producing multi-single-site doped materials.

Although the low-temperature molten salt method enables the efficient synthesis of monodisperse doped compounds, the low-temperature synthesis itself can lead to poor crystallinity of the oxides (e.g., small-sized nanoparticles) and even the formation of large amorphous domains. This jeopardizes the structural stability of the catalyst during the acidic OER at elevated current densities. Compared with low-temperature synthesis, molten salt processing at high temperatures (600–1000 °C) enables the synthesis of high-quality and phase products, which is applicable to the synthesis of a wide range of crystalline compounds (e.g., perovskites, nitrides, carbides, and chalcogenides). Through the use of high-melting-point salts, this process enables enhanced reactant melt and ion/atom diffusion, not only incorporating highly dispersed dopants but also simultaneously forming highly crystalline bulk materials.[114,123–130] Using this method, Tang et al. synthesized unique 3*R*-phase IrO_2 materials (group space: *R*3m No.166) that differ from the conventional rutile-phase structure (Figures 3f,g), in which a low loading of ruthenium (Ru) was doped into the lattice by substitutional doping ($H_{3.8}Ir_{1-x}Ru_xO_4$, Ru: 1.12 ± 0.13 at.%).[68] The product was obtained at 950 °C using Li_2CO_3 as the solvent. HRTEM combined with Ru *K*-edge extended X-ray absorption fine structure (EXAFS) analysis verified the dispersion of atomic Ru in the Ir–O lattice (Figure 3h). Similarly, Ke et al. prepared a type of 1T-phase IrO_2 by introducing a low loading of niobium (Nb) ($Nb_{0.05}Ir_{0.95}O_2$, Nb: 5 wt.%) using molten K_2CO_3 as the solvent at 800 °C. This catalyst possesses a flake-like nanosheet structure,[96] further demonstrating the ability of this approach to create high-surface-area catalysts. In summary, the molten salt method excels at producing high-purity, crystalline materials with controlled particle sizes and uniform atomic distributions of doped heteroatoms, showing great potential in the synthesis of SAD catalyst materials. Importantly, it enables faster reaction rates than solid-state methods and has greater versatility and potential for simpler scaling than conventional wet-chemical and thermal treatment techniques.

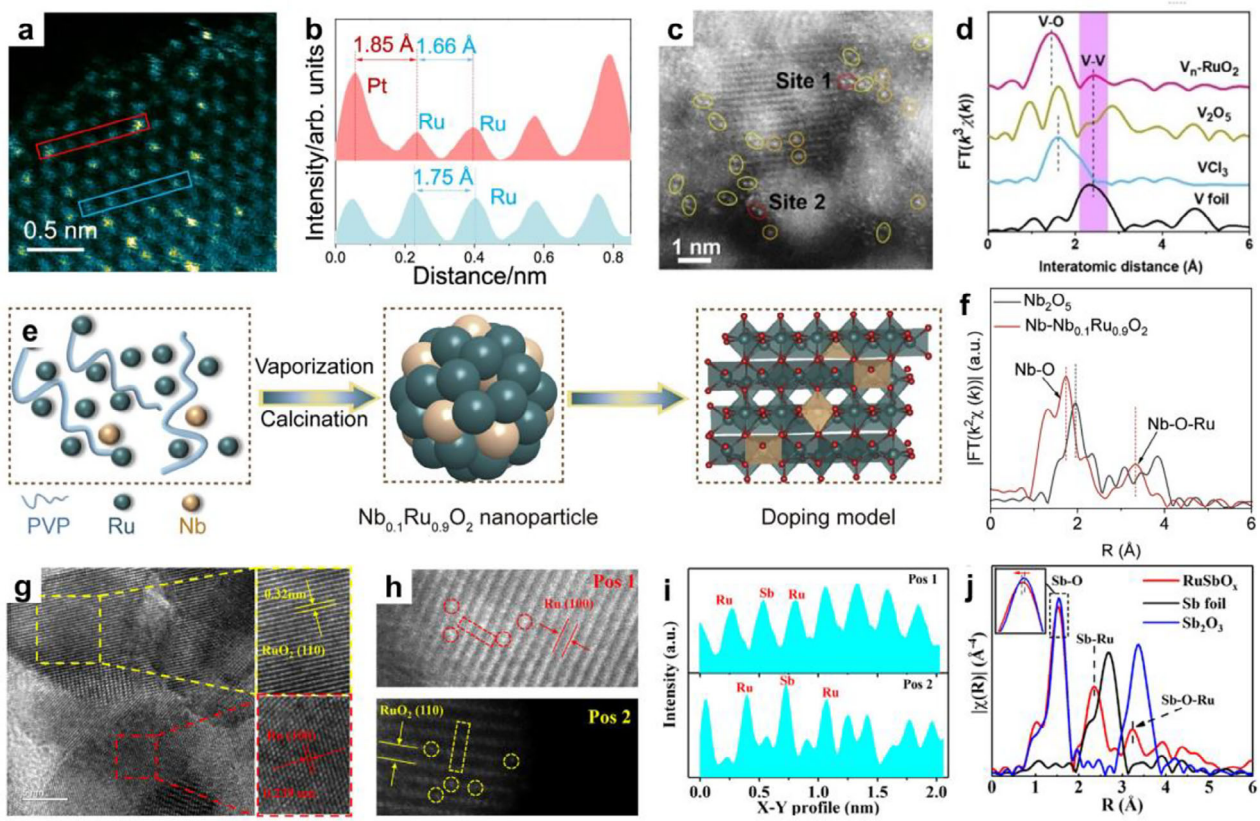

Figure 4. Representative studies of hydrothermal and sol–gel methods. a) HAADF-STEM image of Pt–RuO_2 with a temperature scale. b) Corresponding atomic intensity line profiles extracted from regions marked by red and blue rectangles. c) HAADF-STEM image confirming the atomic dispersion of V atoms. d) FT-EXAFS spectra for V_n–RuO_2 and other samples. e) Preparation scheme for $Nb_{0.1}Ru_{0.9}O_2$. f) Nb *K*–edge FT-EXAFS spectra for $Nb_{0.1}Ru_{0.9}O_2$ and the reference. g) HR-TEM image of $RuSbO_x$. h) Enlarged HAADF-STEM images with Sb single atoms marked by red and yellow cycles. i) Line-scan intensity profiles across the rectangular areas marked in (h). j) k^3-weight EXAFS spectra of $RuSbO_x$ and references.

2.2. Wet Chemical Methods

Wet chemical methods, including hydrothermal/solvothermal, sol-gel, coprecipitation, electrodeposition and chemical bath deposition, have been widely applied in the synthesis of nanomaterials for catalysis applications.[131–134] It offers significant advantages for material synthesis and processing, such as high compositional control, mild reaction conditions, scalability and cost effectiveness.[131,135,136] Recent research has demonstrated that adding metal salt precursors to a solution readily results in the incorporation of single-atom dopants or a second phase. This approach enables the separation of nucleation and growth stages, demonstrating significant practical advantages for synthesizing monodisperse nanoparticles with narrow size distributions.

2.2.1. Hydrothermal Synthesis

Hydrothermal synthesis typically operates at 130–250 °C where the water vapor pressure reaches 0.3-0.4 MPa, offering distinct advantages for fabricating heteroatom-doped precursor materials.[77,102–105,137] By using this method, Cao et al. constructed Pt single-atom-doped RuO_2 nanoparticles (Pt–RuO_2, Pt: 0.94 at.%) with average sizes of 15–19 nm, where hydrothermally synthesized Ru–Cl hydrate serves as a precursor.[105] HAADF-STEM confirmed atomic Pt substitution within the RuO_2 lattice, which induced compressive strain in the Ru–Ru distances near the Pt sites (**Figure 4a,b**). These structural modifications, induced by the incorporation of larger Pt atoms, were found to generate beneficial bulk tensile strain for better catalytic performance. Combining hydrothermal and subsequent pyrolysis treatments, Qin et al. fabricated a type of 2D RuO_2 materials by incorporating atomically dispersed V species (V_n–RuO_2, V: 2.25 at.%).[77] It reveals that the V atoms are incorporated into the Ru–O lattice by substitutional doping into two forms of species: isolated V atoms and V dimers (Figure 4c,d). These studies demonstrate precise control over particle sizes and highly exposed Ir/Ru-based catalyst surfaces via hydrothermal synthesis, resulting in greater exposure of atomically dispersed dopants within the host materials.

2.2.2. Sol–Gel Method

The sol-gel method is a versatile, low-temperature chemical process used to synthesize solid-state materials with excellent compositional control, wide doping flexibility, and uniform atomic dispersion.[70,106,107,138–142] Through this method, Liu et al. synthesized niobium (Nb)-doped RuO_2 nanoparticles ($Nb_{0.1}Ru_{0.9}O_2$,

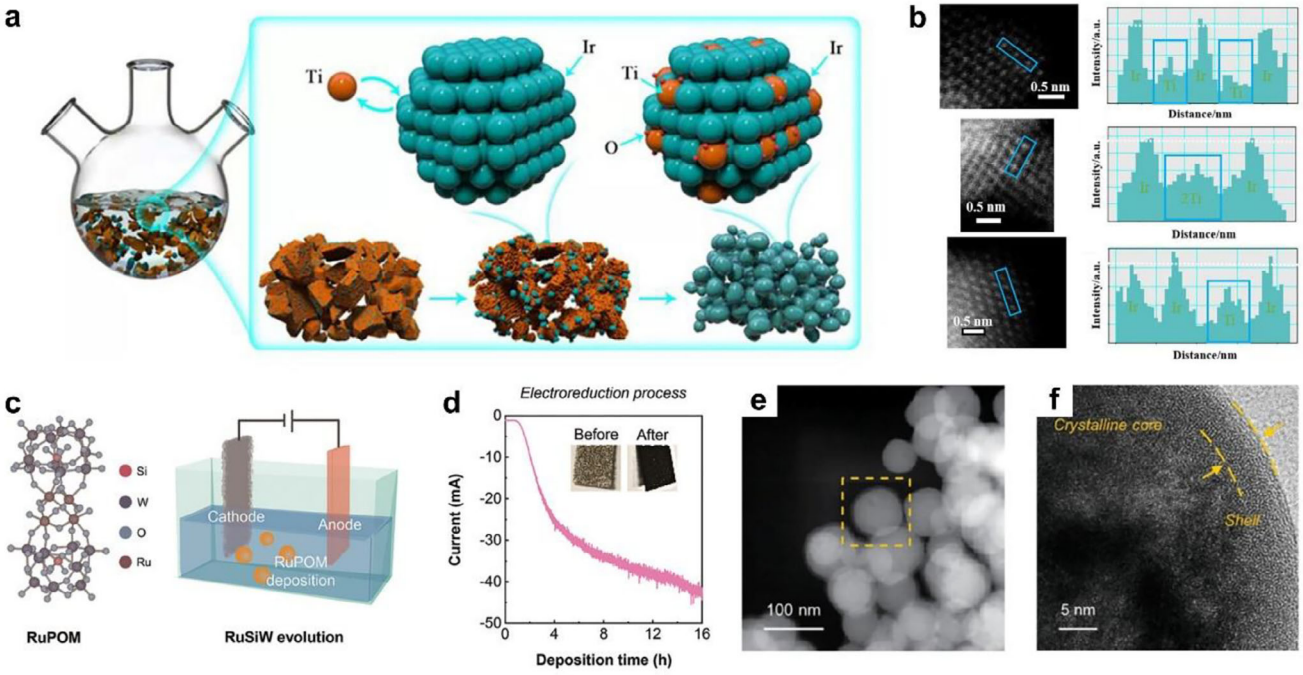

Figure 5. Representative studies of the coprecipitation method. a) Schematic illustration of the synthesis pathway for Ti–IrO_x/Ir. b) HAADF-STEM image of Ti–IrO_x/Ir with the corresponding line profile confirming the elemental distribution. c) Schematic illustrations of the electrochemical deposition of RuSiW using RuPOM as a precursor. d) Comparative characterization of the substrate before and after electrochemical deposition. e) Dark-field STEM image of the RuSiW. (f) HRTEM image of the core–shell structure of the RuSiW.

Nb: 13.44 at.%) using polyvinyl pyrrolidone (PVP) and ethanol as the coordination agent/solvent (Figure 4e).[106] Nb *K*-edge EXAFS spectra revealed the atomic dispersion of Nb in the RuO_2 lattice (Figure 4f). Similarly, Niu et al. fabricated a RuSb single-atom alloy (SSA) via the PVP-mediated sol-gel method.[70] Following post-calcination, the RuSb SSA surface was oxidized to the $RuSbO_x$ product, maintaining the high dispersion of Sb in the RuO_x matrix. HRTEM clearly revealed the coexistence of metal Ru and RuO_2 lattice structures (Figure 4g). TEM combined with FT-EXAFS (Figures 4h–j) verified the monodispersion of Sb atoms within the metal Ru and RuO_2 lattices.

2.2.3. Co-Precipitation Method

The co-precipitation method, which operates under mild temperature conditions, is a facile and scalable wet-chemical approach for synthesizing catalysts with narrow size distributions and uniformity.[108,109,143–145] Wang et al. obtained multi-crystalline spherical IrO_x nanoparticles with the incorporation of a low content of titanium (Ti–IrO_x/Ir, Ti:1.92 wt.%) (**Figure 5a**). The team applied CTAB as a cationic surfactant and TiB_2 as a Ti source, achieving a high dispersion of Ti in the IrO_x matrix. TEM and the scattering signals in the line profile confirmed the occurrence of atomic Ti through substitutional doping (Figure 5b).[109] The co-deposition method for preparing low-content element-doped catalysts possesses a series of significant advantages. Its strength lies in its ability to introduce heterogeneous metal species into the lattice or onto strong binding sites in situ and uniformly during the formation process of the host oxide material, thereby effectively stabilizing the single metal atoms.

2.2.4. Electrochemical Deposition

Electrochemical deposition uses an applied electric field to direct ionic migration while enabling real-time control over deposition kinetics through multiple operational modes, achieving precise regulation of both ion transport and interfacial redox processes.[146–148] As demonstrated by Jeon et al.'s fabrication of RuSiW films on carbon fiber paper via chronoamperometry (Figure 5c,d), isolated metal atoms can be anchored onto defect-rich supports by optimizing the deposition parameters (potential, current density, and pH). This method provides advantages, including simplicity and controllability of the morphology and particle sizes (Figure 5e,f).[110] Nevertheless, it suffers from several significant disadvantages, especially for issues such as weak catalyst-substrate adhesion, phase instability, low loading mass, and impurity sensitivity, which largely limit its scalability and practical OER application.

2.3. Ultrafast Synthesis Methods

2.3.1. Thermal Shock Method

Thermal shock is a type of ultrafast synthesis method that enables instantaneous high-temperature pulses while minimizing the

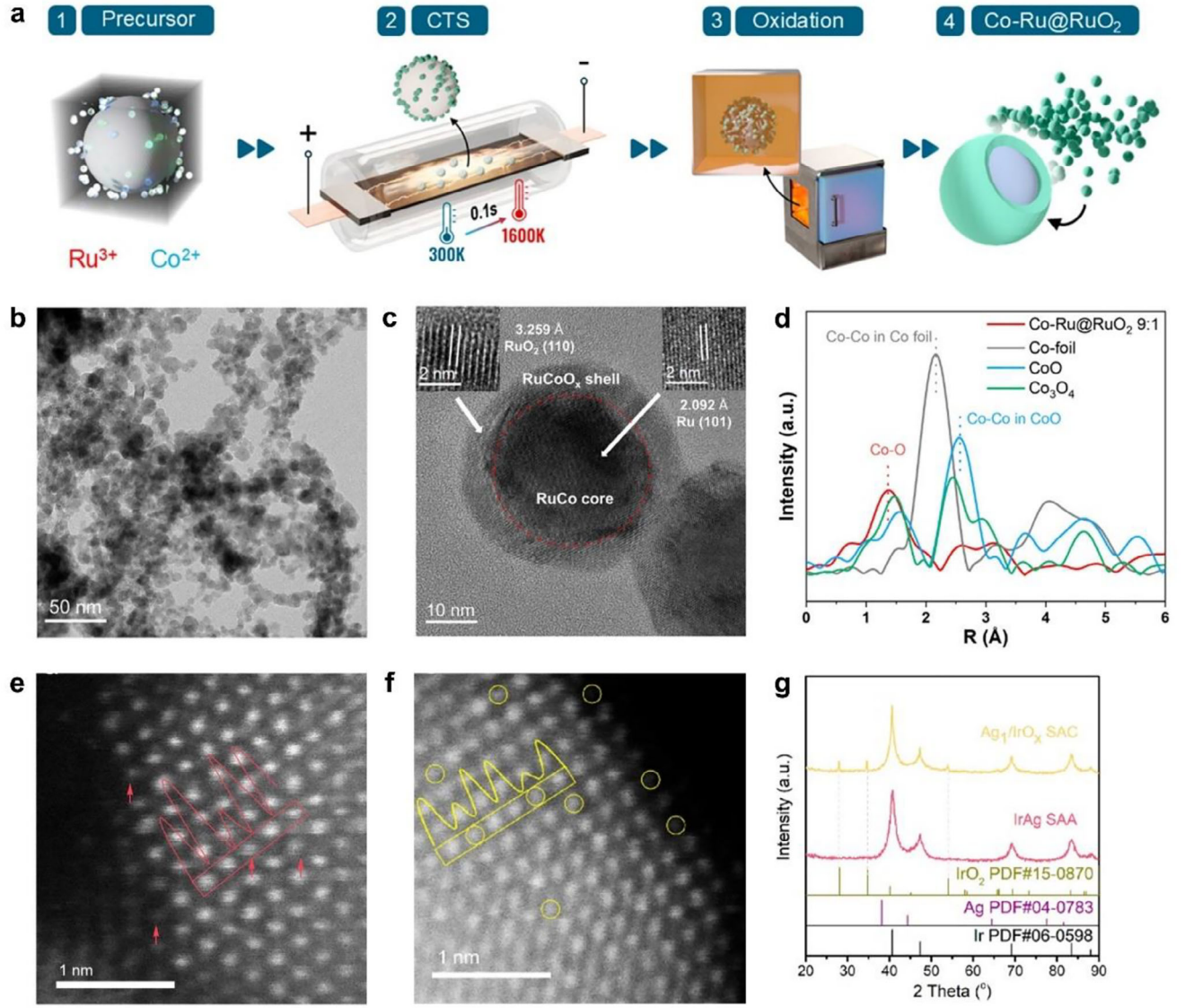

Figure 6. Representative studies of other ultra-fast heat treatment methods. a) Preparation route of the Co–Ru@RuO_2 catalyst. b) TEM image of the Co–Ru@RuO_2 nanoparticles. c) HRTEM image of the core–shell heterostructure of Co–Ru@RuO_2. d) Co *K*-edge EXAFS spectra of Co–Ru@RuO_2 and other reference samples. e) HAADF-STEM image of the Ag_1/IrO_x SAC catalyst. f) HAADF-STEM image of the Ag_1/IrO_x SAC with Ag atoms marked with yellow circles. g) XRD patterns of the Ag_1/IrO_x SAC and IrAg SAA.

heating duration to prevent both metal aggregation and substrate degradation, thereby maintaining atomic-level dispersion.[149–153] Thermal shock can achieve ultrahigh temperatures approaching 3000 K within seconds, surpassing the performance constraints of traditional heating approaches.[154] Recent advances have demonstrated its exceptional capability for synthesizing catalysts with atomic-scale precision. Chen et al. fabricated a Co–Ru@RuO_2 catalyst with core–shell structure via thermal shock. The synthesis involved nitric acid-treated Vulcan XC–72R adsorbing Ru^{3+}/Co^{2+} to form carboxylate complexes, which were then rapidly converted to supported nanoparticles through pulsed electrical heating (1400 K, 0.1 s pulses) with immediate cooling to prevent aggregation (**Figure 6a**).[111] HRTEM images confirmed the formation of core–shell structure (Figures 6b–c). Co *K*-edge XANES (Figure 6d) revealed the oxidation state of atomically dispersed Co atoms, suggesting a stabilized Co–O–Ru structure. In essence, thermal shock synthesis enables rapid atomic dispersion while suppressing metal aggregation, stabilizing single atoms in the lattice.

2.3.2. Laser–Pulse Method

The laser-pulse method excels in producing ultra-pure, defect-engineered (e.g., oxygen vacancies, lattice distortion and surface defects) catalysts that increase the number of active sites for catalytic reactions, making it ideal for the rapid synthesis of nanomaterials.[155–157] Zhang et al. reported a Ag

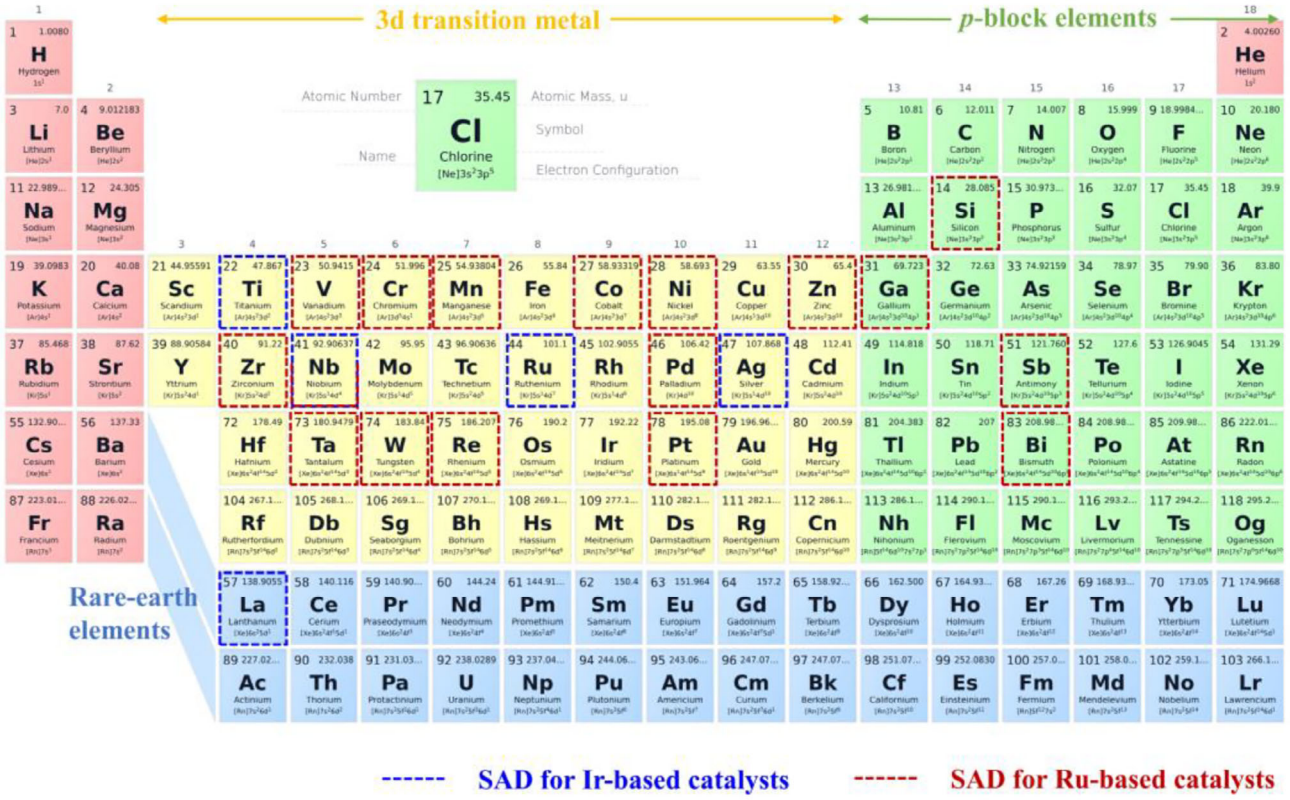

Figure 7. Rational selection of single atoms of SAD Ir- or Ru-based OER catalysts. This schematic illustration is reproduced by referring the periodic table image from PubChem: https://pubchem.ncbi.nlm.nih.gov/periodic-table/#view=table.

single-atom-doped IrO_x catalyst (Ag_1/IrO_x, Ag: 6.5 at.%) for improving acidic OER activity.[112] The team first synthesized AgIr single-atom alloy nanoparticles via laser irradiation and obtained the Ag_1/IrO_x product through post-thermal oxidation. HAADF-STEM images and intensity profile analysis along the lattice confirmed the existence of single Ag atoms (Figure 6e,f). The XRD patterns where metallic Ag-related peaks are not found prove the presence of single-atom Ag in the Ag_1/IrO_x SAC catalyst (Figure 6g). These ultrafast synthesis methods enable the creation of a wide range of composite materials—including alloys, oxides, and high-entropy materials—but face significant limitations, such as low yields and harsh operational conditions (e.g., high-power lasers), hindering their industrial deployment for large-scale synthesis of homogeneous materials.

Above all, researchers have systematically explored the use of the periodic table to synthesize various single-atom-doped Ir- or Ru-based catalysts for the acidic OER (**Figure 7**) via three streamlined synthetic approaches, including molten salt methods, wet chemical methods, and thermal treatment. These methods demonstrate broad applicability for achieving highly atomically dispersed substitutional doping with diverse metals, including 3d transition metals (Ti, V, Cr, Mn, Co, Ni, Zn, Zr, W, Re, Ta), rare earth metals (Nd, La), and *p*-block elements (Ga, Sb, Bi). Among these techniques, the molten salt method and conventional pyrolysis represent scalable routes for SAD catalyst design. They allow optimization of the reaction environment for specific precursors and control over product morphology, enabling the synthesis of materials with tailored microstructures (e.g., high specific surface areas) and high atomic dispersion of dopants. Consequently, rational catalyst design is crucial for selecting the most appropriate synthetic methodology.

3. Rational Design of SAD Ir/Ru-Based Catalysts

3.1. Ir-Based SAD Catalysts

Currently, Ir-based oxides stand as the leading candidate for catalyzing the OER in an acidic environment for a practical PEMWE system. The conventional rutile-type IrO_2 facilitates a stable OER through the adsorption evolution mechanism (AEM) pathway, attributed to its robust Ir–O bonding;[158] however, its insufficient intrinsic activity typically leads to a high overpotential (~370 mV at 10 mA cm^{-2}).[159–161] Motivated by the goal of enhancing intrinsic catalytic activity, SAD strategies have been used to precisely modulate the electronic structure of Ir sites. **Table 2** summarizes the OER performances of state-of-the-art SAD-engineering catalysts in acidic OER. As expected, developed SAD Ir-based catalysts such as LaRuIr,[108] $Nb_{0.05}Ir_{0.95}O_2$,[96] and Ag_1IrO_x[66] have demonstrated high OER activities with low overpotentials of 184, 191, and 224 mV, respectively. The enhanced OER activities of $Nb_{0.05}Ir_{0.95}O_2$ and Ag_1IrO_x exemplify the efficacy of asymmetric coordination structures (e.g., Ir–O–Nb and Ir–O–Ag), which disrupt the charge symmetry of Ir active sites and

Table 2. Comparison of the acidic OER performance of newly reported SAD Ir- or Ru-based oxide catalysts in a three-electrode electrochemical system and PEM electrolyzer.

Catalysts	Electrolyte	Overpotential @10 mA cm^{-2} [mV]	Tafel slope	Stability [h]@10 mA cm^{-2}	Refs.
Ag_1/IrO_x	0.5 M H_2SO_4	224	50.43	50	[66]
$H_{3.8}Ir_{1-x}Ru_xO_4$	0.5 M H_2SO_4	255	56.5	1100	[68]
Ti–IrO_x/Ir	0.5 M H_2SO_4	254	48	100	[109]
Ir/TiN	0.5 M H_2SO_4	277	37.84	1000	[163]
LaRuIr	0.5 M H_2SO_4	184	37.9	60 (50 mA cm^{-2})	[108]
$Nb_{0.05}Ir_{0.95}O_2$	0.5 M H_2SO_4	191	60.5	1100 (1.4 V)	[96]
Bi–RuO_2 SAAO	0.5 M H_2SO_4	192	33.9	650	[100]
Co–Ru@RuO_2	0.5 M H_2SO_4	203	49.73	400	[111]
Ga–RuO_2	0.5 M H_2SO_4	217.5	47.9	150	[98]
$iGa_{0.2}Ru_{0.8}O_2$	0.5 M H_2SO_4	188	44	800 (100 mA cm^{-2})	[71]
$Nb_{0.1}Ru_{0.9}O_2$	0.1 M $HClO_4$	204	51	360 (200 mA cm^{-2})	[106]
Ni–Ru@RuO_x	0.5 M H_2SO_4	184	45.5	200 (20 mA cm^{-2})	[67]
SS Pt–RuO_2 HNSs	0.5 M H_2SO_4	260	61.3	100	[167]
$Re_{0.06}Ru_{0.94}O_2$	0.1 M $HClO_4$	190	55	200	[95]
RuSiW	0.5 M H_2SO_4	142	86.17	100	[110]
Ta–RuO_2	0.1 M $HClO_4$	201	57.7	280	[69]
Mn(SAs)–Ru/RuO_2	0.5 M H_2SO_4	158	59	120	[82]
$Mn_{(SA)}/RuO_2$	0.5 M H_2SO_4	213	55.5	1000	[176]
V_n–RuO_2	0.1 M $HClO_4$	227	51	1050	[77]
C,Ta–RuO_2	0.5 M H_2SO_4	171	53.6	1300	[166]
$Zr_{0.01}W_{0.10}Ru_{0.89}O_x$	0.5 M H_2SO_4	212	47.88	100	[94]
PdCo–RuO_2	0.5 M H_2SO_4	190	43	480	[101]
Sb–RuO_2	0.5 M H_2SO_4	217	56	150 (100 mA cm^{-2})	[70]
SA Zn–RuO_2	0.1 M $HClO_4$	210	58.83	43	[73]
Pt-RuO_2	0.5 M H_2SO_4	215	63.89	1500	[168]

optimize the adsorption of reaction intermediates. These asymmetric orbital hybridizations lower the energy barrier of the rate-determining step, significantly boosting OER activity. In the synthesized LaRuIr catalyst, La doping activates lattice oxygen to participate directly in the OER, inducing the lattice oxygen oxidation mechanism (LOM) and thereby accelerating reaction kinetics. Thus, constructing asymmetric coordination structures and activating the LOM pathway are proposed as effective strategies for enhancing the intrinsic activity of Ir-based single-atom catalysts for the acidic OER.

Despite the progress achieved in catalytic activity, rutile-type Ir oxides still suffer from inevitable degradation and dissolution at high anodic potentials (>1.6 V),[53] primarily due to the formation of soluble high-valent species (e.g., IrO_3 derivatives).[68,96] Catalysts like Ag_1/IrO_x and LaIrRu thus show limited stability (<100 h) despite higher activity. A more promising route lies in unique crystal phases such as 1T- and 3R-phase IrO_2. Their edge-shared IrO_6 octahedra create a cross-linked Ir–O network that stabilizes lattice oxygen, contrasting with the mixed-sharing mode in rutile-IrO_2. This structural advantage enables exceptional longevity, as shown by Ke's $Nb_{0.05}Ir_{0.95}O_2$ (with a 1T-IrO_2 structure)[96] and Tang's $H_{3.8}Ir_{1-x}Ru_xO_4$ (with a 3R-IrO_2 structure),[68] which stably operate for over 1000 h. These results underscore that intrinsic crystal phase stability—exemplified by 1T and 3R structures—offers a greater improvement in OER durability than single-atom doping alone.

Additionally, the use of support materials—such as metal oxides,[39,40,162] nitrides,[163] and diborides[158]—provides an effective strategy to stabilize IrO_x active centers while reducing the loading of precious Ir metal.[42,164] For example, Yang et al. demonstrated that stabilizing IrO_x nanoparticles on a TiN support significantly enhances electrochemical stability (**Figure 8a**).[163] Their study revealed that under applied potential, the leaching of TiN leads to the trapping of trace Ti atoms within the anchored IrO_x particles, resulting in the formation of stable and active Ti-doped IrO_x species. In another study, Strasser and co-workers highlighted the metal/metal-oxide support interaction (MMOSI) effect,[165] which facilitates a strong electronic and structural interplay between an antimony-doped tin oxide (ATO) support and IrO_x catalysts (Figure 8b). This interaction markedly improves the corrosion resistance of IrO_x during the acidic oxygen evolution reaction.

3.2. Ru-Based SAD Catalysts

In recent years, cost considerations have motivated extensive research into doping strategies for the acidic OER, with a

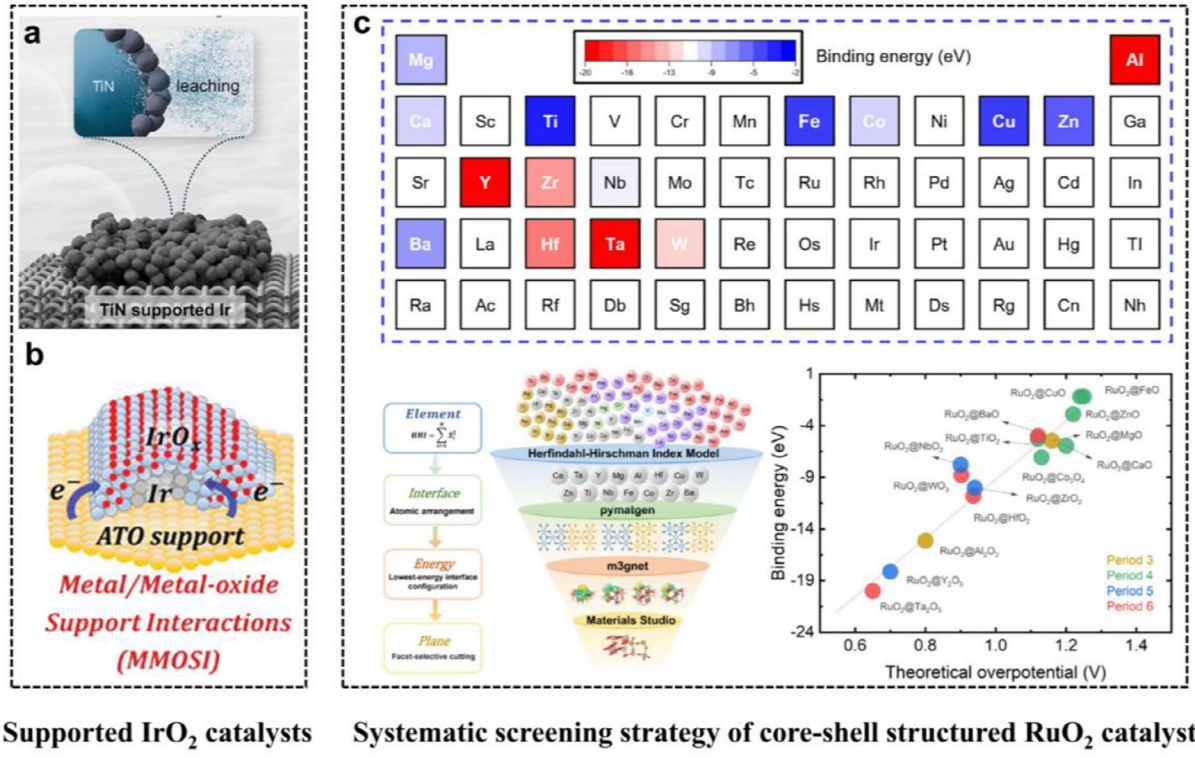

Figure 8. a) Schematic illustration of the TiN support in stabilizing surface amorphous IrO_x catalysts for oxygen evolution. b) Schematic illustration of the IrO_x particles on ATO support.[160] c) Schematic illustration of the systematic screening strategy for guiding the rational design of core–shell structured RuO_2 catalysts.

growing emphasis on Ru-based catalysts. However, conventional doping methods often encounter issues such as element segregation, particle agglomeration, and leaching of dopant ions. The single-atom doping (SAD) strategy effectively overcomes these limitations and offers distinct advantages for optimizing Ru-based catalysts. As summarized in Table 2, most SAD-modified catalysts exhibit high OER activity with low overpotentials (<200 mV), substantially outperforming conventional RuO_2 catalysts. More notably, prominent examples such as Mn(SA)/RuO_2,[82] C,Ta–RuO_2,[166] and Pt–RuO_2[167] have demonstrated exceptional durability in acidic media, maintaining stable performance for over 1000 h at 10 mA cm^{-2}. Apart from the intrinsic activity performed in a three-electrode configuration system, the high-current density stability (≥500 mA cm^{-2}) in PEM device is critical for evaluating the potential of those catalysts for industrial applications. **Table 3** summarizes the performances of those SAD-engineering Ir/Ru-based catalysts in PEMWE. Impressively, a Pt-doped RuO_2 catalyst (Pt–RuO_2) achieved a low cell voltage of 1.673 V at 2 A cm^{-2} and maintained long-term stability for 500 h at 500 mA cm^{-2} in a PEM electrolyzer.[168] The Mn(SA)/RuO_2 catalyst can operate stably under a high current density of 1 A cm^{-2} for 180 h in PEM device. These works represent a significant breakthrough in laboratory-level research for Ru-based catalysts in PEM electrolyzer applications.

To rationally design advanced SAD Ru-based catalysts for acidic OER, the key principle lies in enhancing the resistance of Ru sites to acid and oxidative corrosion during OER. From the perspective of element selection, several strategies have been proposed to address this challenge. Introducing high-valent dopants with high electronegativity (e.g., Re,[95] Nb[106]) has proven effective in suppressing Ru over-oxidation via electron transfer effects, thereby mitigating Ru dissolution and improving OER stability. Corrosion-resistant dopants such as Sb,[70] Ta,[69] and Zr[94] can stabilize the Ru–O framework and reinforce the overall lattice structure. Certain low-valent dopants, including Na,[169] Pt,[167] and Pd,[94] have been reported to act synergistically with oxygen vacancies, weakening Ru–O covalency and lowering the Ru *d*-band center, which suppresses the LOM pathway. In some cases, steering the reaction pathway from the conventional AEM route to the oxide path mechanism (OPM) route by constructing local structural symmetry (e.g., $Mn^{4+\delta}$–O–$Ru^{4+\delta}$) offers a promising route to enhance both catalytic activity and stability.[137] This unique pathway promotes direct coupling of adsorbed oxygen species (*O–*O), bypassing the thermodynamic scaling limitations of AEM while maintaining structural integrity. Additionally, engineering dual-atom (e.g., PdCo-RuO_2,[101] $Zr0_{.01}W_{0.10}Ru_{0.89}O_x$[94]) or multi-atom doping sites (e.g., M-RuIrFeCoNiO_2,[23] RuIrNiCoCrO_2[170]) with defined geometry for synergistic effects offers new opportunities for balancing the OER activity and stability.

Current design principles offer valuable insights for the rational selection of doping elements to stabilize RuO_2 catalysts and fine-tune their electronic structure. However, persistent challenges remain, including the surface corrosion of Ru atoms and degradation of SAD sites. To address these issues, growing attention has been directed toward constructing

Table 3. Comparison of the acidic OER performance of newly reported SAD Ir- or Ru-based oxide catalysts in PEM electrolyzer.

Catalysts	Noble metal [mgIr/Ru cm−2]	Cell voltage	Stability	Operational temperature [°C]	Refs.
$H_{3.8}Ir_{1-x}Ru_xO_4$	0.75	2.11 V@2 A cm^{-2}	1280 h@2 A cm^{-2}	80	[68]
Ti–IrO_x/Ir	0.42	1.774 V@2 A cm^{-2}	220 h@2 A cm^{-2}	80	[109]
Ir/TiN	0.087	1.80 V@2 A cm^{-2}	500 h@1 A cm^{-2}	80	[163]
LaRuIr	–	1.84 V@0.7 A cm^{-2}	50 h@0.05 A cm^{-2}	80	[108]
$Nb_{0.05}Ir_{0.95}O_2$	3.3	1.634 V@1 A cm^{-2}	1200 h@1.2 A cm^{-2}	60	[96]
Bi–RuO_2 SAAO	2.0	1.97 V@3 A cm^{-2}	24 h@0.2 A cm^{-2}	60	[100]
Co–Ru@RuO_2	0.34	1.65 V@1 A cm^{-2}	200 h@0.5 A cm^{-2}	60	[111]
$iGa_{0.2}Ru_{0.8}O_2$	–	1.788 V@3 A cm^{-2}	200 h@0.5 A cm^{-2}	80	[71]
$Nb_{0.1}Ru_{0.9}O_2$	1.38	1.69 V@1 A cm^{-2}	100 h@0.3 A cm^{-2}	80	[106]
SS Pt–RuO_2 HNSs	–	–	100 h@0.1 A cm^{-2}	25	[167]
$Mn_{(SA)}/RuO_2$	1.12	2.06 V@2 A cm^{-2}	180 h@1 A cm^{-2}	80	[176]
C,Ta–RuO_2	1.0	1.81 V@2 A cm^{-2}	100 h@1 A cm^{-2}	60	[166]
$Zr_{0.01}W_{0.10}Ru_{0.89}O_x$	3.0	1.44 V@0.1 A cm^{-2}	650 h@0.1 A cm^{-2}	50	[94]
PdCo–RuO_2	1.52	1.688 V@2 A cm^{-2}	160 h@0.2 A cm^{-2}	80	[101]
Sb–RuO_2	0.626	1.95 V@2 A cm^{-2}	200 h@0.2 A cm^{-2}	80	[70]
Pt-RuO_2	1.45	1.791 V@3 A cm^{-2}	500 h@0.5 A cm^{-2}	80	[168]

protective overlayers on RuO_2.[171–174] A notable example is the core–shell RuO_2@TaO_x nanorod electrocatalyst developed by Li et al., which demonstrates superior OER activity and stability.[175] The corrosion-resistant TaO_x shell helps suppress Ru dissolution and promotes charge transfer via interfacial effects. Notably, the selection of TaO_x as the optimal shell material was guided by a multi-step systematic screening strategy introduced by the research team, which involved the evaluation of multiple high-melting-point metal oxides (Figure 8c). This methodology not only facilitates rapid assessment of material candidates but also enables the rational design of high-performance electrocatalysts.

4. Theoretical Calculations and Descriptor for Mechanistic Study

Elucidating the reaction mechanism of OER catalysts requires a synergistic approach that combines advanced in situ/operando characterization with theoretical modeling. Techniques such as *operando* X-ray absorption spectroscopy (XAS), in situ Raman spectroscopy, in situ infrared spectroscopy (FTIR), and differential electrochemical mass spectrometry (DEMS) provide atomic-scale insights into the evolution of active sites' electronic structures and the formation of reactive intermediates. Theoretical calculations, particularly density functional theory (DFT), are indispensable for interpreting these complex processes and validating the experimental findings. This section focuses on DFT calculations to summarize key computational tools and descriptors for rationalizing the mechanisms of enhanced catalytic activity and stability.

4.1. Volcano Plot and Free Energy Diagram

According to the Sabatier principle, the ideal catalyst binds intermediates neither too strongly nor too weakly.[177] Weak binding of the reaction intermediate renders the first step thermodynamically unfavorable, whereas strong binding prevents the second step from proceeding spontaneously. For electrochemical reactions like the OER, the most direct activity descriptors are the adsorption free energies (ΔG_{-ads}) of critical intermediates (e.g., *OH, *O, *OOH). Due to scaling relationships between these energies, the entire reaction pathway can often be described by a single descriptor. This allows for the calculation of the theoretical overpotential (η), which serves as a quantitative activity metric; a lower η signifies higher activity. The overpotentials for a series of materials (e.g., lanthanide-doped and undoped RuO_2)[56] can be analyzed by plotting them against a descriptor such as $\Delta G_{O^*} - \Delta G_{OH^*}$, establishing a volcano plot that visually highlights the most promising candidates (**Figure 9a**). Complementing this thermodynamic overview, reaction energy barriers (E_a) offer crucial kinetic information. Free energy diagram calculations for the optimal catalyst reveal that the rate-determining step (RDS) is the formation of *OOH (Figure 9b),[56] an assessment vital for understanding the kinetics of materials near the volcano apex.

4.2. Bader Charge

Bader charge serves as a pivotal descriptor that links the electronic structure at atomic-scale of catalyst and its macroscopic performance metrics (e.g., overpotential and volcano plot of activity). In the Er–RuO_2 catalyst,[56] for instance, Bader analysis reveals pronounced charge accumulation around the *OH intermediate, signifying substantial electron donation from the Er–O–Ru moiety to *OH (Figure 9c). This electron redistribution strengthens the subsequent *OH adsorption. In the Bi-RuO_2 SAAO catalyst, Bader charge revealed the Ru cations is more positively charge within the asymmetry Bi-O-Ru structure, leading to shorter Ru-O bond length, consistent with their experimental proves of Raman, EXAFS,

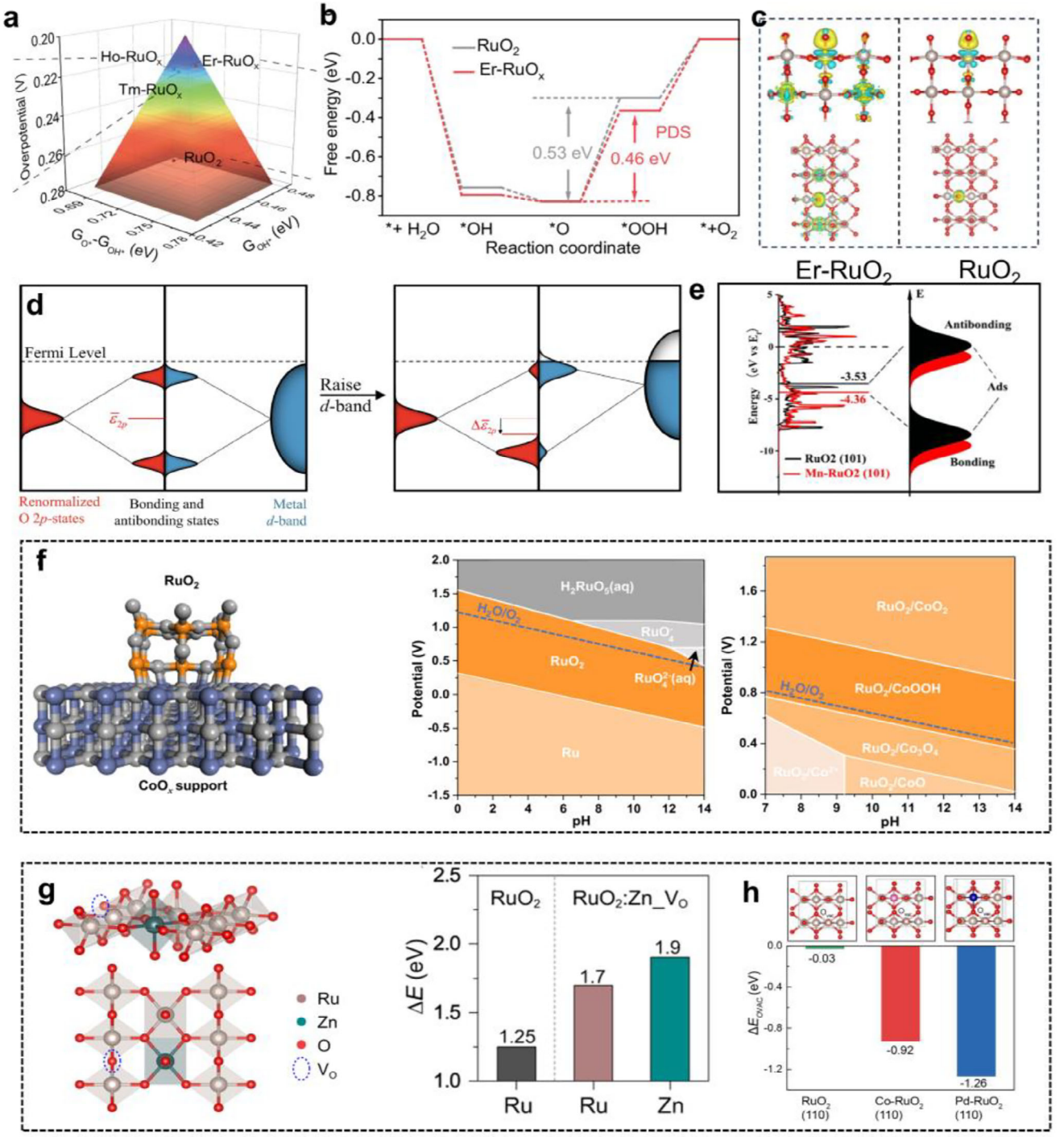

Figure 9. Theoretical calculations and descriptors. a) Volcano plot for different doped RuO_2 (Er, Tm, Ho) and undoped RuO_2 samples. b) Free energy diagram of the optimal Er-RuO_2 and RuO_2 reference catalysts. c) Bader charge analysis of the optimal Er-RuO_2 and RuO_2 reference catalysts. d) Schematic illustration of the *d*-band center theory. e) Examples of PDOS analysis revealing the *d*-band center position of Mn-doped RuO_2 sample. f) DFT Pourbaix diagram of the RuO_2/CoO_x catalyst compared with the RuO_2. g) The calculation of dissolution energy of metal elements of Zn/V_o-doped RuO_2 and pure RuO_2 samples. h) The calculation of the oxygen vacancy formation of different doped RuO_2 and pure RuO_2 samples.

and XPS.[100] Overall, Bader charge serves as a powerful tool for quantifying adsorption strength and interfacial electron transfer.

4.3. *d*-Band Center Theory

The *d*-band center theory is a powerful conceptual framework in DFT calculations that explains and predicts the strength of adsorbate binding on transition metal surfaces.[178] Introduced by Hammer and Nørskov,[179] it provides a bridge between electronic structure and catalytic activity. A higher-lying (more-positive) *d*-band center closer to the Fermi level indicates a higher density of electronic state available at energies favorable for interaction with adsorbate orbitals, leading to stronger bonding with adsorbates (*OH, *O, and *OOH) (Figure 9d). For example, Chen et al. reported a Mn-doped RuO_2 catalyst for enhanced acidic OER and investigate the effect of Mn dopants in regulating the *d*-band center of Ru sites. The partial density of states (PDOS) revealed the E_d of RuO_2 is down-shifted from Fermi level after Mn incorporation, indicating the weakened adsorption of intermediates (Figure 9e). This contributes to enhance the deprotonation process of oxy-intermediates and reduce the free energy of RDS, resulting in improved activity.[180] Overall, this *d*-band center theory helps in understanding activity trends and rationally designing new catalysts with improved performance and stability.

4.4. Pourbaix Diagram

To assess catalytic stability, computational tools focus on thermodynamic descriptors. The DFT Pourbaix diagram is the definitive tool for determining electrochemical stability, identifying the thermodynamically stable phases of a material under specific pH and potential conditions. Typically, Du et al. calculated the Pourbaix diagram of RuO_2 and developed a RuO_2/CoO_x catalyst to evaluate its thermodynamic stability (Figure 9f).[19] Their findings demonstrate that RuO_2 constructs a more stable interface on an oxidized CoO_x support than unsupported RuO_2, thereby forming a robust Co–O–Ru interaction throughout the OER potential range. This metal–support interaction reduces the total energy of the hybrid system and suppresses RuO_2 dissolution, significantly enhancing structural stability.

4.5. Dissolution Energy and Formation Energy

DFT calculations can also assess the thermodynamic favorability of structural evolution under harsh OER conditions, including processes such as metal dissolution and the formation of oxides or hydroxides. Specifically, the dissolution energy (ΔE_{-diss}) serves as a useful atomistic descriptor for evaluating the tendency of metal dissolution in acidic OER environments, helping to unveil the origin of enhanced catalyst stability. For instance, Zhang et al. synthesized Zn-doped RuO_2 nanowires with oxygen vacancies, which exhibited improved stability during acidic OER.[58] Their results showed that Ru sites in the Zn/O_{vac}-doped RuO_2 possess a more positive ΔE_{-diss} value than those in pure RuO_2, indicating greater resistance to dissolution (Figure 9g). This suggests that the co-incorporation of Zn and oxygen vacancies contributes to the enhanced OER stability of RuO_2. Additionally, bulk thermodynamic properties such as the cohesive energy[181] (for metal) or formation energy (for compounds)[56] offer insight into the intrinsic stability of the material against decomposition. Tang et al. calculated the oxygen vacancy (O_{vac}) formation energy for three models: RuO_2, Co-RuO_2, and Pd-RuO_2[101] (Figure 9h). These calculations revealed that the Pd-RuO_2 model has the most negative E_{vac} value, indicating that surface oxygen vacancy formation is most facile in this structure. This evidence corroborates that oxygen vacancy formation is enhanced in specific doping scenarios.

Through DFT calculations, it is possible to evaluate the adsorption energies of OER intermediates on different materials and establish activity descriptors (such as adsorption energy of intermediates, *d*-band center position, oxygen vacancy formation energy, etc.), thereby guiding experimental synthesis. This integrated approach is vital for navigating the common trade-off between activity and stability to identify truly optimal and durable catalysts.

5. OER Performance Enhancement Mechanism

By reviewing recent advances in SAD-engineering Ir/Ru-based catalysts, we highlight that the SAD strategy offers distinct advantages in manipulating the catalyst structure to achieve high performance in acidic OER. Although significant progress has been made, the mechanistic understanding of how activity and stability are improved remains insufficient for the rational design of advanced SAD catalysts. This section provided a detailed summary of several types of performance enhancement mechanisms in conjunction with research methodologies, coupled with the analysis of advanced ex/in-situ characterization techniques and theoretical calculation methods.

5.1. Lattice Strain Modulation

Lattice distortion—atomic displacement from ideal crystal lattice sites—tunes electrocatalysts' electronic structures by altering bond lengths, angles, symmetry, and orbital overlap, thus adjusting key catalytic properties such as adsorption energies and charge transfer.[182–187] Recent advances in tailoring metal lattice distortion through the SAD strategy have opened new frontiers in optimizing the electrocatalytic performance for the acidic OER.[14,66,69,108,109,100,111,167] By deliberately engineering lattice tensile strain or compressive strain via single-atom doping, electrocatalysts can be tuned to optimize intermediate binding energies, accelerating OER kinetics and stabilizing catalysts.[184,185,188–193]

In a typical study, Gao et al. developed a lanthanide (La)-based microalloying strategy utilizing trace lanthanum (La, 0.85 at.%) to engineer LaRuIr nanocrystalline catalysts.[108] Crucially, the large-sized La atoms preferentially occupy edge sites, forming a La-stabilized Cottrell atmosphere.[194,195] This configuration induces both compressive and tensile strain within the Ru–Ir system (**Figure 10a**). According to molecular dynamics (MD) simulations, the compressive strain caused by La incorporation downshifts the *d*-band centers of Ir and Ru active metals. This shift promotes overlap with the O-*p* band of oxygen ligands and reduces

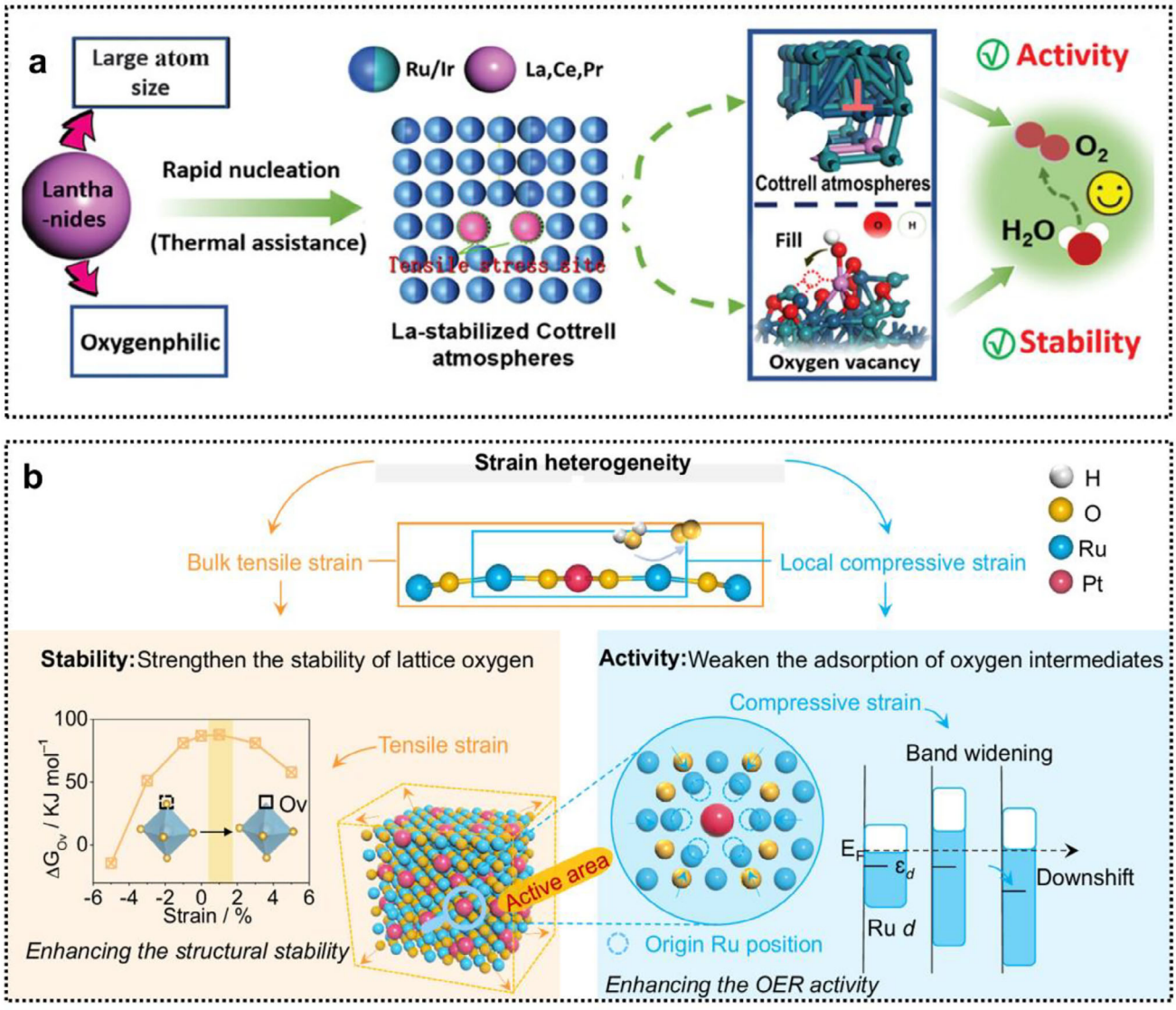

Figure 10. Lattice strain mechanism. a) Schematic diagram of the synthesis strategy for La microalloying RuIr nanocrystal catalysts. The large-sized La toms introduce Cottrell atmosphere in the tensile stress site. d) Schematic diagram of Pt single-atom-doped RuO_2 (Pt–RuO_2) that induces bulk tensile strain and local compressive strain for the enhancement of the acidic OER.

the activation energy for the OER. In contrast, tensile strain in other regions upshifts the *d*-band centers of Ir/Ru, increasing the electron density near the Fermi level. This facilitates the adsorption of more OER reactants and accelerates the reaction kinetics. As a result, the synergistic interplay between compressive and tensile strain enhances OER activity through both the AEM and LOM pathways. More importantly, the MD simulations revealed that H_2O preferentially adsorbs onto the Ru-Ir bridge site in the AEM calculation. Based on this finding, this site was therefore selected as the active center for OER.

More recently, Cao et al. proposed a strategy of strain heterogeneity engineering to improve the OER performance of RuO_2 by incorporating single Pt atoms (Pt–RuO_2, Pt: 0.94 at.%).[168] Likewise, the incorporation of large-sized Pt atoms introduces bulk tensile strain and local compressive strain into the RuO_2 structure (Figure 10b). To explore the influence of bulk tensile strain, the team performed DFT calculations to evaluate the enthalpy change associated with lattice oxygen loss. The results indicate that bulk tensile strain increases the thermodynamic stability of lattice oxygen, thereby enhancing the overall structural stability of RuO_2. Further PDOS calculations revealed that the localized compressive strain downshifts the Ru *d*-band center, weakening the adsorption of oxygen intermediates and optimizing their binding energies. Based on these findings, the team proposed that the Pt-induced compressive-strain regions act as highly active centers for promoting OER activity. To identify the true active sites, the energy barriers for OER on various Ru atoms within the compressive-strain region were compared. It was found that Ru sites in close proximity to Pt dopants possess a pronouncedly lower energy barrier, confirming them as the most active

centers for OER in the Pt-RuO_2 system. Overall, these studies exemplify the emerging paradigm of "lattice strain engineering" through SAD in electrocatalyst design, highlighting how atomic-level lattice manipulation can systematically stabilize the active centers and optimize both thermodynamic kinetics in multistep OER processes.

5.2. Dynamic Electron Donor Modulation Mechanism

The instability of Ir- or Ru-based oxides under high oxidative potentials (>1.6 V vs. RHE) has been extensively studied and is attributed primarily to the formation of soluble high-valent species (e.g., IrO_3 and RuO_4 species) and excessive participation of lattice oxygen in the acidic OER.[196–199] These processes ultimately lead to irreversible structural collapse and severe performance degradation.[200–202] Recent advances in catalyst stabilization strategies have revealed that metal doping as an electron donor enables precise electronic modulation through dynamically replenishing electron density during the OER.[60,95] The primary function of electron donors is to anchor and protect catalytically active sites, thereby preventing their oxidation or dissolution.[73,82]

High-valent metals, such as Re,[61,95] Hf,[3] W,[8,21] Ta,[55,117] are regarded as ideal electron donors in acidic OER catalysts due to their unique advantages, including strong electronegativity, oxidation resistance, and corrosion resistance. Sun et al. developed atomically dispersed niobium (Nb)-doped RuO_2 ($Nb_{0.1}Ru_{0.9}O_2$, Nb: 5 wt.%), demonstrating the efficacy of high-valent transition metal doping for enhancing both activity and stability in the acidic OER.[106] Notably, the inherent stability of pentavalent Nb^{5+} ions against oxidation helps to stabilize the RuO_2 lattice structure. X-ray absorption near-edge spectroscopy (XANES) at the Ru *K*-edge and Nb *K*-edge revealed an increase in the valence state of Ru and a decrease in that of Nb, indicating electron transfer from Nb to Ru sites (**Figure 11**a,b). Cyclic voltammetry (CV) analysis further showed a markedly lower current response for the Ru^{6+}/Ru^{8+} redox couples in $Nb_{0.1}Ru_{0.9}O_2$ compared to pristine RuO_2, directly confirming the suppression of Ru oxidation (Figure 11c). This strong electronic interaction between Nb and Ru helps immobilize the active sites within the lattice. As a result, $Nb_{0.1}Ru_{0.9}O_2$ exhibited long-term stability under a high current density of 200 mA cm^{-2} in a three-electrode system.

In a parallel breakthrough, Xing et al. proposed an electron-donating modification strategy to stabilize tungsten-doped ruthenium oxide ($WRuO_x$) under harsh oxidative conditions by incorporating acid-resistant zirconium (Zr) ($Zr_{0.01}W_{0.10}Ru_{0.89}O_x$, Zr: 1 wt.%) (Figure 11d).[94] XPS and Raman spectroscopy (Figure 11e) collectively demonstrate that the valence state of Ru active sites and the Ru–O bond length remain largely unchanged during OER, indicating that doping can create stable active sites. This implies that well-designed Zr-O-Ru coordination environments can yield true, stable active sites without reconstruction. Bader charge analysis further reveals an increased electron density and a reduced chemical valence of Ru sites, confirming electron transfer from Zr to Ru (Figure 11f). Moreover, the formation energy of oxygen vacancies (ΔG_{-OV}) in Zr-doped $RuWO_x$ is found to be higher than in other comparable materials, indicating that Zr doping effectively stabilizes the lattice oxygen. Together, these results underscore that the electron-donating role of Zr and the robust Zr–O–Ru structure jointly contribute to the enhanced long-term OER stability. Impressively, the $Zr_{0.01}W_{0.10}Ru_{0.89}O_x$ catalysts can stably operate in PEM device for over 600 h at a current density of 100 mA cm^{-2}.

In some cases, high-valence metal dopants play a dual role, acting not only as stabilizers but also simultaneously serving as electronic modulators, achieving a well-balance for the OER activity and stability. Qiao et al. demonstrated a remarkable dynamic electron-regulatory mechanism in Re-doped RuO_2 ($Re_{0.06}Ru_{0.94}O_2$),[95] where single Re atoms exhibit dual functionality: acting as electron acceptors at low overpotentials to activate Ru sites and then transitioning to electron donors at elevated potentials to prevent Ru overoxidation (Figure 11g). *Operando* XAFS techniques have captured these coordination changes, indicating that the Re single sites reconstruct dynamically to optimize intermediate adsorption. DFT calculations revealed that Re-doped RuO_2 exhibits the lowest energy barrier for the OER via the AEM pathway (Figure 11h). Furthermore, the simulations provided critical insight into the identification of the actual active sites. The results demonstrate that the unsaturated Re sites in Re-RuO_2 are inactive for OER due to the excessively strong adsorption of key oxygen intermediates.

Extensive research, as mentioned previously, has demonstrated the effectiveness of high-valent metals as electron donors in stabilizing OER catalysts under acidic conditions. In contrast, other studies have shown that incorporating low-valence metals as charge modulators is a viable strategy for enhancing catalytic activity.[21,137,167–169,203–207] This approach, often seen in metal oxide catalysts, involves the introduction of cations like Na,[169] Ag,[66] Pt,[167] and Pd,[101] which promotes the formation of oxygen vacancies to maintain crystal lattice neutrality. These oxygen vacancies can then function as highly active sites or act synergistically with dopants to improve the catalyst's intrinsic activity. A typical paradigm was demonstrated by Luo et al. through the rational design of bismuth (Bi) single-atom-doped RuO_2 nanocrystal (Bi-RuO_2 SAAO) catalysts for improving acidic OER performance.[100] The team demonstrated the incorporation of Bi single atoms contributes to increase the Ru valence through electron donor effect (**Figures 12**a–b) and generate extra oxygen vacancies (Figure 12c). These highly active Ru^{x+} ($x > 4$) species[165,208–210] coordinated with oxygen vacancies contributes to reduce the OER energy barrier in AEM pathway, as evidenced by the DFT simulation.

A critical trade-off of using low-valence metal dopants for enhanced activity is their inherent instability. Under harsh acidic OER conditions, these species are susceptible to oxidation or dissolution, resulting in rapid catalyst deactivation. Consequently, achieving a balance between high activity and long-term stability remains a significant challenge. Multi-element doping is a promising strategy to concurrently address both requirements.[21,44,117,211] For instance, Tang et al. engineered dual single-atom doping by introducing Pd and Co atoms into a RuO_2 matrix (PdCo–RuO_2) to significantly increase the acid OER stability.[101] The enhanced OER performance originates from the synergistic cooperation of Pd, Co, and oxygen vacancies. Specifically, *operando* XANES (Figure 12d) revealed that Pd^{2+} serves as an electron donor to prevent Ru over-oxidation, while EPR

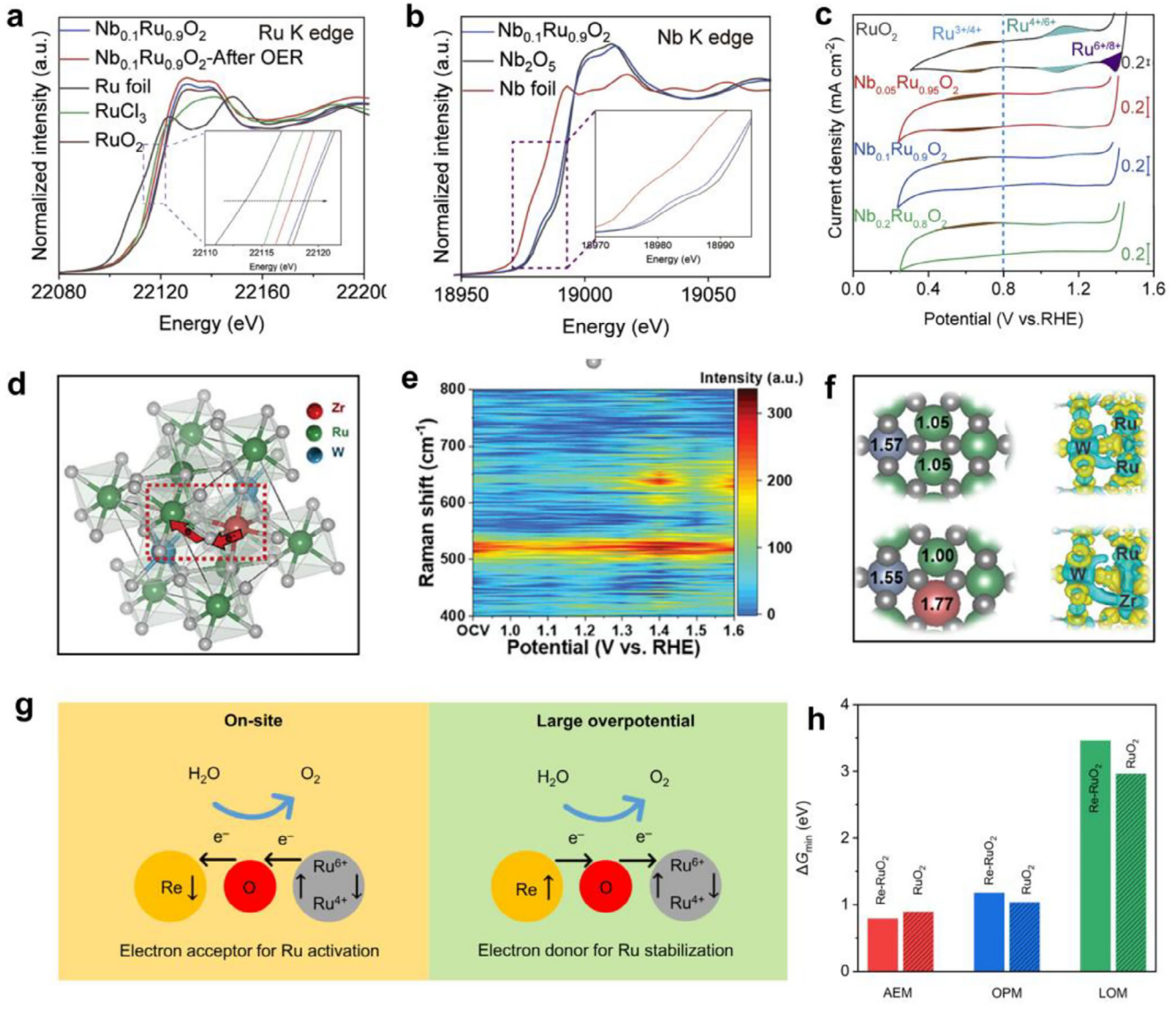

Figure 11. Dynamic electron donor modulation. a) XANES Ru *K*-edge results of Nb–doped RuO_2 samples. b) XANES Nb *K*-edge results of Nb–doped RuO_2 samples. c) CV curves of a series of Nb–doped RuO_2 samples and pure RuO_2. d) Schematic diagram of the electron transfer process from Zr to adjacent Ru sites in the $Zr_{0.01}W_{0.10}Ru_{0.89}O_x$ catalyst. e) Contour map of the in situ Raman analysis of the $Zr_{0.01}W_{0.10}Ru_{0.89}O_x$. f) Bader charge analysis of Zr and W doped RuO_2. g) Schematic diagram of the dynamic electron transfer between Re and Ru sites of Re-RuO_2 catalyst. h) Minimum activation energy of Re-RuO_2 and RuO_2 in three reaction pathways (AEM, LOM, and OPM).

analyses (Figure 12e) confirmed the generation of oxygen vacancies induced by Pd^{2+}, whereas the theoretical 2D overpotential map demonstrates that Co incorporates optimize intermediate adsorption and reduce the OER overpotential (Figure 12f). Working together, these components suppress the LOM pathway and optimize intermediate adsorption for enhanced activity and stability. In parallel, Huang et al. developed single-site Pt-doped RuO_2 hollow nanospheres (SS Pt–RuO_2 HNSs, Pt: 2%) with the presence of interstitial C that demonstrated superior overall water splitting performance in acidic electrolytes (Figure 12g).[167] The team revealed the interstitial C elongate the Pt–O and Ru–O bond, regulating the metal-O covalency for the optimization of reaction intermediates binding. Build on this, DFT calculations further revealed that the single-site Pt configuration elevates the *O dissociation energy by 1.22 eV (ΔG_o) relative to that of pristine RuO_2 (Figure 12h), thereby stabilizing the lattice oxygen atoms for enhanced stability. Moreover, the calculated ΔG for PDS revealed the incorporation of isolated Pt atoms reduces the energy barrier of *OOH formation by 0.282 eV (Figure 12i), identifying the enhanced OER activity.

For the doping system, the catalytic performance is more generally influenced by a combination of multiple mechanisms. For instance, Liu and colleagues constructed a short-range-ordered tantalum (Ta) single atoms to modify coordination environments and enhance the catalytic activity of RuO_2

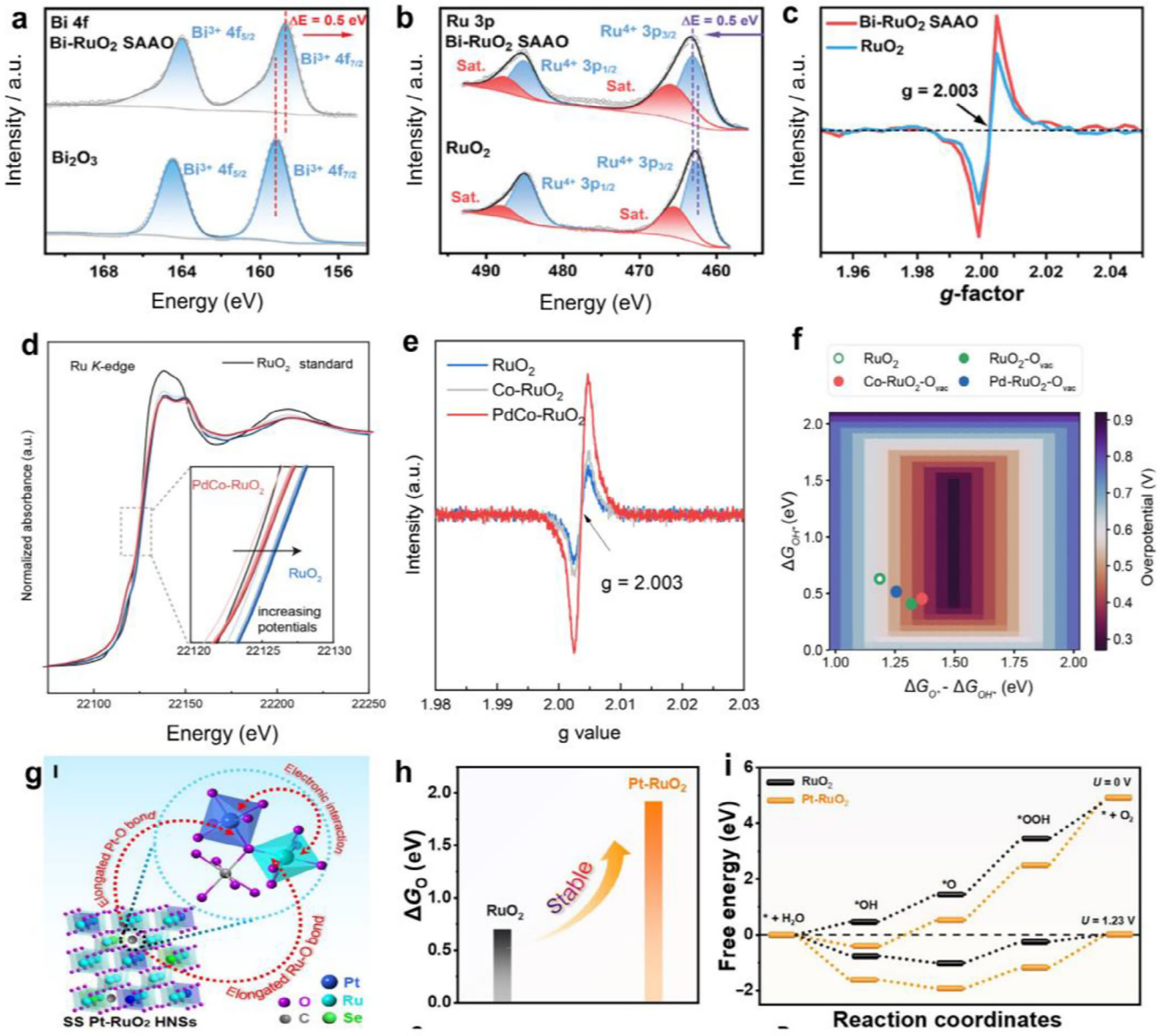

Figure 12. Dynamic electron donor modulation. a) Bi 4*f* XPS spectra of Bi single-atom-doped RuO_2 (Bi–RuO_2 SAAO) and the Bi_2O_3 reference. b) Ru 3*p* XPS spectra of Bi–RuO_2 SAAO and the RuO_2 reference. c) EPR analysis of the Bi-doped RuO_2 and undoped RuO_2. d) *Operando* XANES Ru *K*-edge of PdCo-RuO_2 and RuO_2 samples. e) EPR analysis of RuO_2, Co-RuO_2, and PdCo-RuO_2 samples. (f) DFT 2D overpotential map of different structure models. g) Schematic diagram of the interstitial C modulating the Ru-O and Pt-O bond length of SS Pt-RuO_2. h) The energy of oxygen vacancy formation of RuO_2 and Pt-doped RuO_2. (i) Free energy diagram of the RuO_2 and Pt-doped RuO_2.

(Ta–RuO_2, Ta: 2.5 wt.%).[69] TEM analysis indicated that doping with large-sized Ta atoms expanded the crystal lattice by ≈2% (**Figure** 13a). Furthermore, Ru and Ta *K*-edge XANES spectra confirmed electron transfer from Ta to Ru, as evidenced by the energy shifts of the absorption edges. This transfer resulted in a decreased valence state of Ru and a corresponding increase for Ta (Figure 13b,c). Together, this synergy between electron transfer and strain effects boosts both activity and stability. Likewise, a recent demonstration by Yang and colleagues employed a titanium nitride (TiN) substrate that undergoes controlled electrochemical oxidation,[163] facilitating Ti leaching into surface amorphous iridium oxide (IrO_x) clusters (Ir/TiN, Ti: 2.9%) (Figure 13d). Mechanistic analysis revealed that the dispersed Ti–O species induce lattice tensile strain by strategically elongating Ir–O bonds (Figure 13e). This effect arises primarily because of the electron transferring from Ti to Ir (Figure 13f), which weakens the Ir–O covalency. The isolated Ti atoms in Ir/TiN catalyst remain stabilized within the IrOx lattice even upon oxidation, which can be attributed to the strong Ti–O–Ru bonding interaction. Consequently, the energy barrier for the OER is reduced, and lattice oxygen activation is suppressed—both critical factors for enhancing OER activity and stability.

Existing research on SAD has outlined key regulatory effects like lattice strain, electron transfer, and defect engineering. In

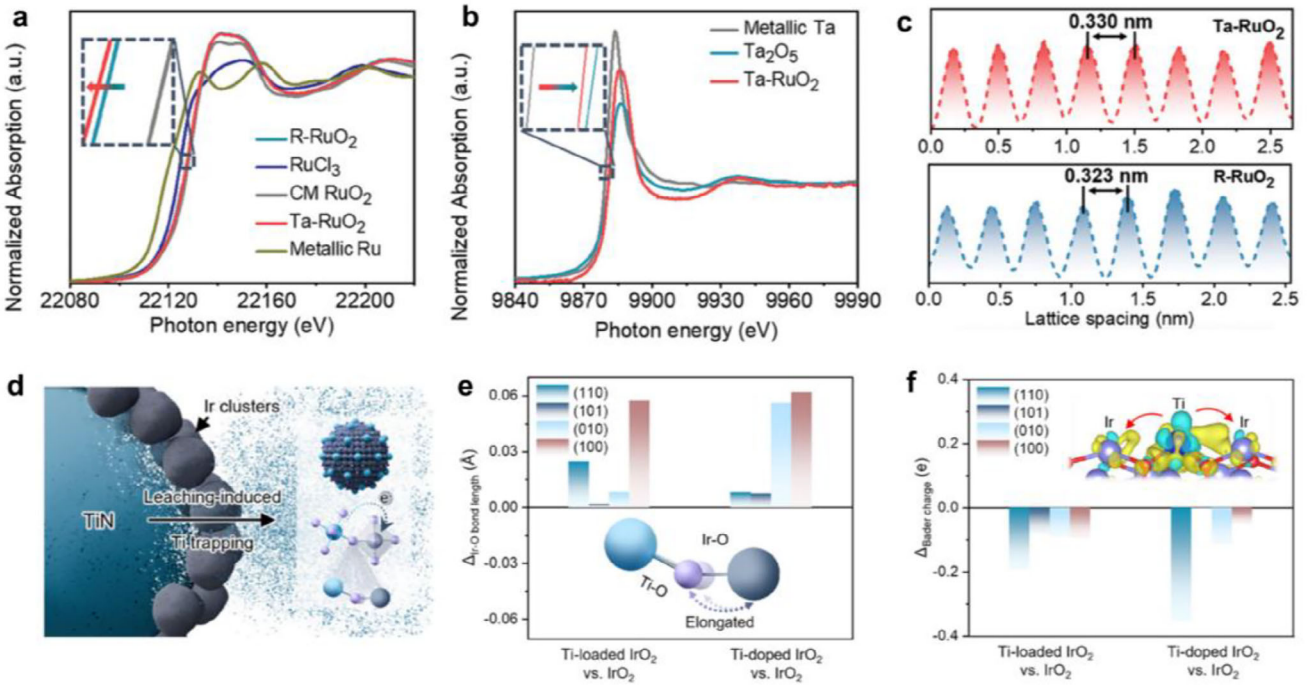

Figure 13. Synergetic effect modulation effect. a) XANES spectra at Ru K-edge of Ta-RuO2 and other reference samples. b) XANES spectra at Ta K-edge of Ta-RuO2 and other reference samples. c) Intensity profile of (110) planes of Ta-RuO2 and R-RuO2. d) Schematic diagram of the process of Ti leaching into IrO_x clusters during OER. e) Calculation of the Ir-O bond length of the Ti-doped IrO_2 system on different lattice planes. f) Calculation of Bader charge of the Ti-doped IrO_2 system on different lattice planes.

practice, however, synergistic effects beyond these individual mechanisms must be considered. The potential existence of multiple active sites, such as grain boundaries, uneven crystalline degree, lattice distortion and defect site on the catalyst surface, which may act synergistically, adds further complexity to the reaction mechanism. Overall, it is the synergistic interplay that universally leads to a more optimal adsorption-energy landscape, drastically improving both the activity and stability of these OER electrocatalysts.

5.3. OER Reaction Pathway Modulation

5.3.1. AEM Pathway Optimization

The conventional AEM pathway in the acidic OER involves four concerted proton-electron transfer (CPET) processes.[185,212] In this mechanism, protons are desorbed from oxo-intermediates and subsequently released into the electrolyte.[213,214] However, under proton-rich conditions (low pH), proton accumulation on the catalyst surface hinders the deprotonation of oxo-intermediates, thereby slowing the CPET kinetics.[215] To accelerate the deprotonation pathway and maximize the efficiency of the CPET step, introducing heteroatoms or bridging oxygen atoms as proton acceptors has proven to be effective.[54,93,212,216–218] For example, Peng et al. reported a proton-transfer-promoted AEM (PAEM) mechanism involving the introduction of acid-resistant *p*-block metal sites (Sb, In, Sn) into a RuO_2 matrix, resulting in an asymmetric Ru–O–M structure.[219] In this configuration, protons desorbed from oxo-intermediates adsorb onto the dopant metal atoms, thus accelerating the deprotonation process. The authors proposed that this asymmetric structure has a low proton binding energy, which further facilitates deprotonation, according to the Sabatier principle (**Figure 14a**). In situ FTIR spectroscopy revealed a shift in the characteristic peak to a higher wavenumber, indicating the accelerated deprotonation of *OOH intermediates on the $Ru_{0.8}Sb_{0.2}O_2$ catalyst (Figure 14b). Consequently, the Ru–O–Sb unit facilitates electron accumulation around the Sb sites, promoting the formation of active high-valent Ru species and thereby enhancing the OER activity.

In parallel, Jiang et al. constructed a 3D interstitial-substitutional mixed structure by incorporating carbon (C) and tantalum (Ta) atoms into RuO_2 (denoted C,Ta–RuO_2).[166] In this structure, interstitial carbon atoms serve as proton acceptors, modifying the reaction path from a conventional AEM to a new one-termed proton acceptor-electron donor mechanism (PAEDM) (Figure 14c). DFT calculations revealed that these C atoms promote the PAEDM pathway by accepting protons, resulting in a lower energy barrier than that of the conventional AEM pathway (Figure 14d). To optimize proton transfer, Ke et al. introduced acid-resistant niobium (Nb) into edge-shared 1T phase iridium oxide (1T–IrO_2) ($Nb_{0.05}Ir_{0.95}O_2$, Nb: 5 wt.%).[96] Incorporating Nb shifts the rate-determining step (RDS) from *OOH deprotonation to *O–OH coupling. This shift results in a substantially lower energy barrier of 0.50 V, representing a clear reduction from the 0.67 V barrier observed for IrO_x (Figure 14e). Thus, deliberate control of this proton transfer process addresses

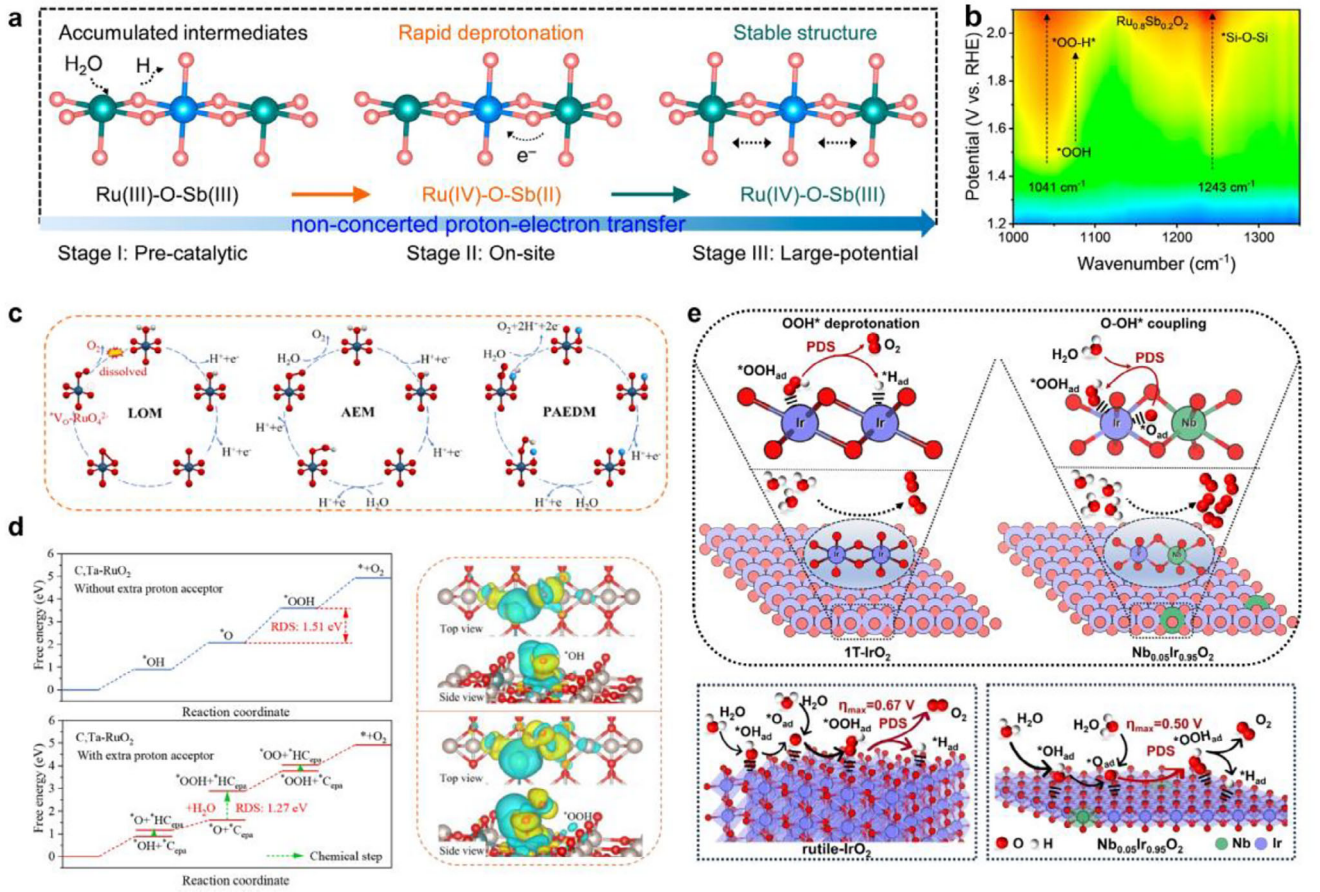

Figure 14. Proton transfer promotion mechanism. a) Schematic diagram of the incorporated Sb single atom in the $Ru_{0.8}Sb_{0.2}O_2$ catalyst serving as a proton acceptor for accelerating the OER deprotonation process. b) In situ FTIR spectrum of the $Ru_{0.8}Sb_{0.2}O_2$ catalyst. c) The proposed PAEDM pathways of the C,Ta–RuO_2 catalyst. d) Comparison of the free energy diagram and charge density difference for C,Ta–RuO_2 without an extra proton acceptor and with an extra proton acceptor. e) Schematic diagram of the different potential determining step (PDS) and energy barrier values for 1T–IrO_2 and Nb–doped IrO_2 ($Nb_{0.05}Ir_{0.95}O_2$).

both the activity and stability challenges inherent in the harsh acidic OER environment.

5.3.2. Oxide Pathway Mechanism (OPM) Modulation

More recently, the oxide path mechanism (OPM) has been identified as an alternative OER pathway (**Figure 15a**).[57,220] OPM enables the direct coupling of *O–*O radicals at dual-metal sites without consuming lattice oxygen, thus facilitating O_2 release while maintaining structural stability.[36,58,221,222] However, designing high-performance OPM catalysts remains challenging because the precise structural requirements for OPM are still unclear. Researchers previously demonstrated that Ru atom arrays with shorter interatomic distances promote oxygen radical generation and direct *O–*O coupling, activating the OPM pathway.[221,223] For example, Yan et al. doped Mn into RuO_2 ($Mn_{0.2}RuO_2$), forming an asymmetric $Mn^{4-\delta}$–O–$Ru^{4+\delta}$ structure that served as the active center for the acidic OER. Combined in situ FTIR, DEMS, and XAFS analyses revealed the occurrence of the OPM pathway via charge redistribution within the Mn–O–Ru configuration. This conclusion was supported by two key observations. First, the formation of M–*O–O*–M intermediates was indicated by a vibration peak at ~1100 cm^{-1}, which suggested the direct coupling of *O–O* species. Second, O_2 production occurred without the involvement of lattice oxygen.

Following this paradigm, a single-atom-doping strategy was proposed to implement an OPM-like pathway for the acidic OER. More recently, Liu et al. introduced dispersed vanadium (V) atoms into a RuO_2 lattice (V_n–RuO_2, V: 2.25 at.%) to increase the OER activity, which induces two types of active sites, V dimers and single V atoms.[77] The FTIR spectra revealed a distinct adsorption band at ≈1108 cm^{-1}, assignable to O–O stretching modes of M–*O–O* species (Figure 15b). This feature suggests O-bridge formation between Ru–V dual-metal sites via an OPM pathway. To further verify this, the team conducted two-step *operando* DEMS with isotope labeling in 0.1 M $HClO_4$ using alternating $H_2{}^{[18]}O$ and $H_2{}^{[16]}O$ solvents (Figures 15c-d). The OPM-dominated ^{18}O-labeled catalyst principally enables direct coupling of surface-bound ^{18}O adsorbates from adjacent dual-metal sites to release[36] O_2. As anticipated, the DEMS results revealed dominant $^{36}O_2$ signals (^{18}O–^{18}O) from the ^{18}O-labeled

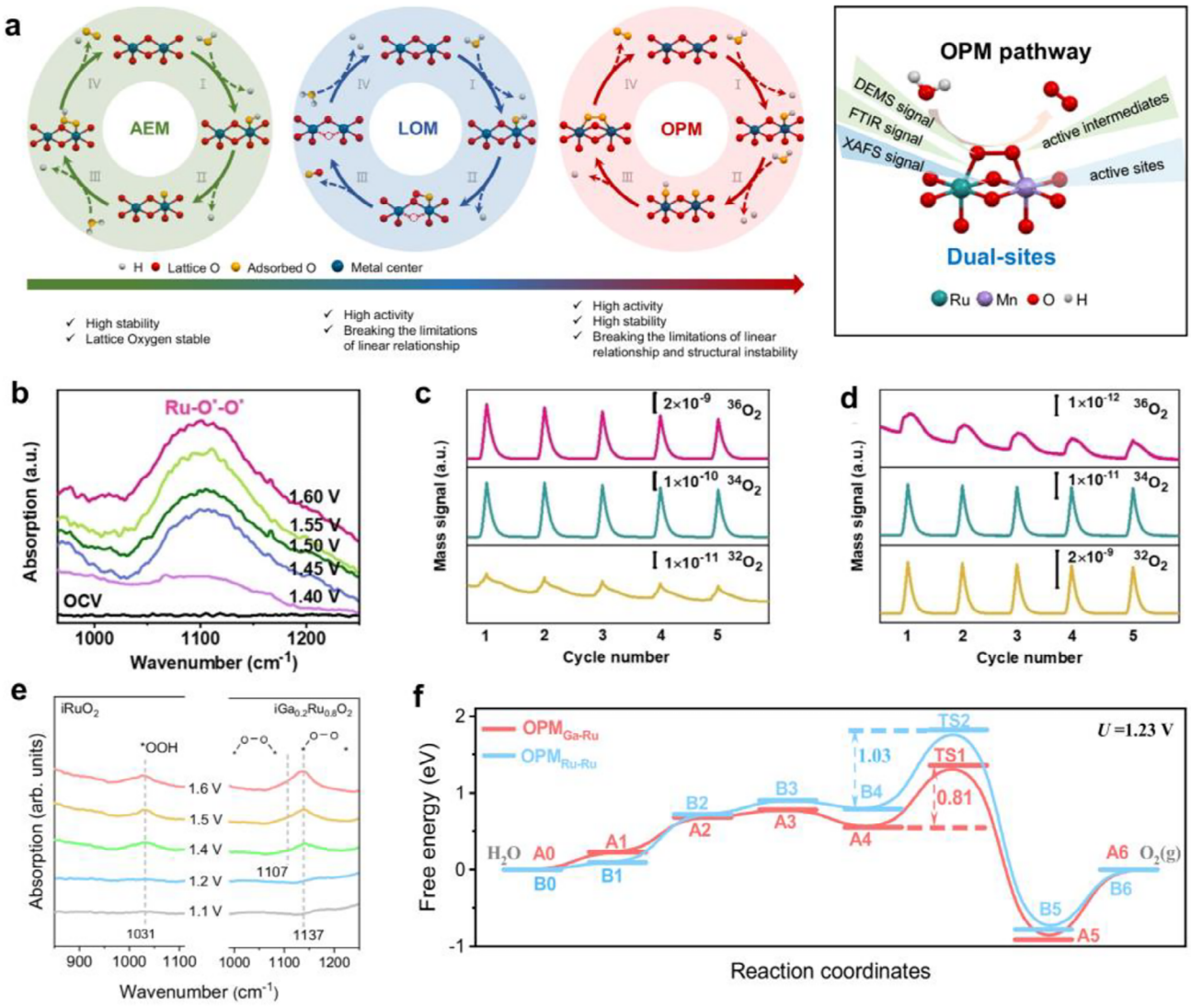

Figure 15. Oxide path mechanism (OPM). a) Three typical reaction pathways for the acidic OER: AEM, LOM and OPM. OPM pathway identification involves the application of various characterization methods, including DEMS, FTIR and XAFS techniques. b) In situ FTIR spectra showing the occurrence of –O*–O* intermediates, which are characteristic of the OPM pathway. Operando DEMS detection of[18] O–labeled V_n–RuO_2 tested in c) H_2[18]O and d) H_2[16]O solvents in 0.1 M $HClO_4$. e) In situ FTIR spectra of Ga single-atom-doped RuO_2 ($iGa_{0.2}Ru_{0.8}O_2$). Operando DEMS detection of f) RuO_2 and g) $iGa_{0.2}Ru_{0.8}O_2$ samples in 0.5 M H_2SO_4–H_2[18]O and 0.5 M H_2SO_4–H_2[16]O electrolytes.

V^n–RuO_2, confirming the OPM-driven OER. This work highlights the crucial role of V dimer sites in reducing the Ru–V interatomic distance and weakening *O intermediate adsorption at V sites, thereby promoting the energetically favored OPM. Wang and colleagues recently reported that incorporating atomic Ga into RuO_2 ($iGa_{0.2}Ru_{0.8}O_2$, Ga: 6.8 wt.%) enhances the spatiotemporal coordination of oxygen radicals, thereby promoting *O–O* coupling for improved OER activity and stability.[71] Through operando FTIR measurements, the team identified the OPM pathway on $iGa_{0.2}Ru_{0.8}O_2$ by detecting characteristic intermediates, including M–*O–O*–M and M–*O–O* species (Figure 15e). Furthermore, DFT calculations indicated that the kinetic overpotential of the AEM pathway 0.57 eV higher than the OPM pathway, confirming the $iGa_{0.2}Ru_{0.8}O_2$ preferentially favors the OPM pathway (Figure 15f). Based on these findings, we conclude that the SAD strategy offers unique advantages in steering the catalytic pathway toward the OPM route for enhanced OER performance, owing to its ability to precisely modulate the electronic structure of metal active sites at the atomic level.

5.3.3. Other Proposed Reaction Pathways

Beyond the three widely discussed reaction mechanisms (AEM, LOM, and OPM), ongoing research is dedicated to exploring novel pathways to further advance the mechanistic study of OER catalysts. Yang et al. proposed a bridging-oxygen-assisted deprotonation (BOAD) pathway in $Zr_{0.01}W_{0.10}Ru_{0.89}O_x$ catalysts.[94] Specifically, the team calculated the hydrogen adsorption energy on bridging-oxygen (O_bri) sites and demonstrated that it

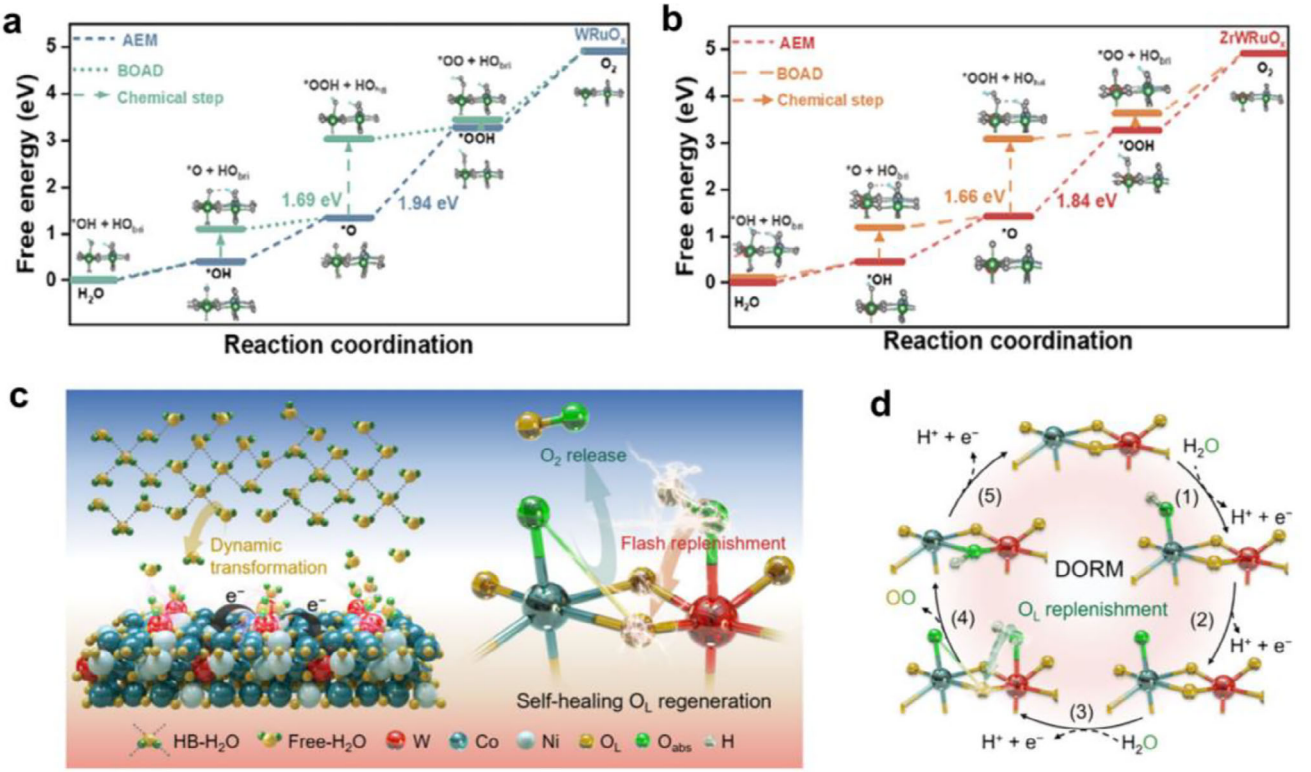

Figure 16. Other proposed reaction pathway. Bridging-oxygen-assisted deprotonation (BOAD) pathway of a) W-doped RuO_x and b) Zr- and W-doped RuO_x catalysts. c) Schematic illustration of the electrochemical interface during water oxidation. d) Schematic illustration of DORM pathway.

is lower on Ru–O_bri–W sites than on undoped RuO_2. This reduction is primarily attributed to the stronger Brønsted acidity of O_bri induced by W dopants, which accelerates the deprotonation process. As a result, the BOAD pathway exhibits a lower energy barrier compared to the AEM pathway (**Figure 16**a,b). To stabilize the lattice oxygen, Li et al. developed an innovative oxophilic-site-mediated dynamic oxygen replenishment mechanism (DORM) in a non-noble W–$NiCo_2O_4$ catalyst (Figure 16c). This mechanism facilitates rapid and continuous healing of oxygen vacancies generated by the LOM process through the optimization of interfacial water species (Figure 16d). Remarkably, this approach mitigates uncontrolled lattice oxygen loss while promoting oxygen exchange via facilitated water dissociation, thereby establishing a self-sustaining redox cycle that surpasses the limitations of conventional AEM or LOM pathways. This work introduces a new paradigm for local electronic regulation by synergistically coordinating lattice dynamics with interfacial reactivity.

5.3.4. Co-Existing Reaction Pathways Modulation

Based on these insights, we emphasize that elucidating reaction pathways is crucial for understanding the complex mechanism of the acidic OER. This complexity arises from the coexistence of multiple possible pathways—such as AEM, LOM, OPM, BOAD, and DORM—governed by the distinct electronic and coordination structures of the active sites. These mechanisms often compete or coexist under varying catalytic conditions or applied potentials, making it challenging to identify the dominant route. For instance, both AEM and LOM pathways often coexist in doped Ir- or Ru-based catalysts (*e.g.*, $H_{3.8}Ir_{1-x}Ru_xO_4$,[68] LaRuIr[108]). In doped Ir-based systems, AEM is generally considered the dominant OER pathway, enabling stable operation though limited by sluggish kinetics. Doping can activate lattice oxygen within asymmetric Ir–O–M motifs, inducing a localized LOM pathway that enhances intermediate adsorption and improves OER activity. In contrast, doped Ru-based catalysts exhibit a different behavior: the pronounced presence of the LOM pathway increases the risk of structural instability (e.g., Pt-RuO_2[167]). Therefore, suppressing LOM and promoting AEM is essential to achieve high stability.

It is recognized that in doped catalysts, the OER pathway—whether governed by a single mechanism or shaped by multiple coexisting ones—is ultimately a consequence of electronic modulation arising from doping effects. These include lattice strain, electron donation, defect engineering, and interfacial microenvironment regulation, as discussed subsequently. A precise understanding of the OER mechanism therefore, hinges on establishing a clear causal chain: doping induces charge redistribution at the active site, which shifts the adsorption energy of intermediates, thereby steering the reaction pathway and ultimately determining the catalytic performance. A reliable investigation of these pathways requires combining advanced in situ techniques—such as Raman and infrared spectroscopy coupled with DEMS—to monitor reactive intermediates and oxygen

products, along with DFT simulations to identify the most favorable reaction mechanism.

5.4. Interfacial Water Microenvironment Modulation

Rather than taking place at isolated active sites, the reaction occurs via a complex interfacial process. It involves proton-coupled electron transfer (PCET), a mechanism whose dependence on the interfacial electric field, local pH, and hydrogen-bond network remains incompletely understood. The interfacial water environment—referring to the structured layers of water molecules formed at the catalyst-electrolyte boundary—plays a critical role in determining the overall efficacy of electrocatalytic processes.[35,224–227] This interfacial water acts as an active mediator in PCET, profoundly influencing the reaction pathways and kinetics of electrocatalytic reactions such as CO_2 reduction and OER, which involve concurrent proton and electron transfers. Nevertheless, the mechanistic relationship between changes in the interfacial water environment and the enhancement of catalytic activity remains inadequately understood.

Vibrational spectroscopy techniques, such as infrared and Raman spectroscopy, are widely used to investigate the chemical environment of interfacial water.[226,228,229] These techniques enable the extraction of vibrational signals from adsorbed species through appropriate data processing. Based on such analyses, researchers have proposed several structural models of interfacial water, including tetrahedrally coordinated water, trihedrally coordinated water, and weakly hydrogen-bonded free water (free-OH).[227,230] In the context of acidic OER, the water network facilitates proton and electron transfer by shuttling protons to and from the active sites. A weak hydrogen-bond network tends to promote water adsorption and dissociation but may also cause proton enrichment on the catalyst surface.[224,231] This can hinder intermediate deprotonation and subsequently slow down O_2 evolution (**Figure 17a**). On the other hand, an overly strong hydrogen-bond network, while beneficial for proton transfer, introduces a high energy barrier for OER activation.[232,233] Therefore, precisely engineering the interfacial water microenvironment is crucial for optimizing OER performance.

In a representative study, Luo et al. developed a series of p-block metal (Ga, In, Sn) single-atom-doped RuO_2 catalysts to modulate the hydrogen-bonding network of RuO_2 for enhanced OER activity.[98] *Operando* ATR-SEIRAS measurements showed that Ga–RuO_2 (with 6.8 wt.% Ga) exhibited a higher proportion of free water compared to other variants, indicating a weakened hydrogen-bonding structure (Figure 17b). PDOS analysis combined with a volcano plot revealed that Ga–RuO_2 possesses higher Ru–O covalency than pure RuO_2 and Sn–RuO_2, though lower than that of In–RuO_2, correlating with its lowest OER overpotential. These findings suggest that modifying the interfacial water network can optimize Ru–O covalency to enhance OER performance. Further DFT calculations demonstrated that a higher concentration of interfacial free water significantly reduces the energy barrier of the rate-determining step (RDS), underscoring the facilitative role of interfacial water in the OER process.

Similarly, Cao et al. reported that Sb single atoms can tailor the interfacial water environment in $RuSbO_x$ catalysts, leading to improved activity in acidic OER.[70] Operando ATR–SEIRAS results indicated a higher concentration of free water at the catalyst surface in $RuSbO_x$ compared to RuO_x. Based on Bader charge analysis, the team revealed that the adsorption energy of oxygen intermediates—particularly the *O species (ΔG_{-*O})—is higher on $RuSbO_x$ than on RuO_x. This optimization promotes the migration of interfacial water from the electrolyte to the catalyst surface and accelerates the interaction between interfacial water and *O to form *OOH, thereby boosting catalytic activity (Figure 17c). These results demonstrate that single-atom doping sites can optimize the electronic structure of active centers by tailoring the local hydrogen-bond network, leading to more favorable adsorption of reaction intermediates and improved OER kinetics.

6. Practical Guidelines for PEM Application

To date, the performance of OER catalysts in PEMWE has also garnered significant interest in the pursuit of commercial-scale electrolysis. Although those single-atom dispersed (SAD) Ir- or Ru-based catalysts have demonstrated remarkable intrinsic activity and stability in three-electrode systems (Table 1), their implementation under practical PEM operating conditions remains a considerable challenge (Table 2). The U.S. Department of Energy (DOE)'s 2026 targets for industrial PEM water electrolysis require operating at a current density of 3 A cm^{-2} with a cell voltage of 1.8 V, with a system lifetime exceeding 80,000 h. Current laboratory research remains far from meeting these benchmarks, constrained by factors such as high equipment costs, lack of standardized testing protocols, and limited research timelines. That said, several recent studies have demonstrated acidic OER catalysts capable of stable operation for thousands of hours at high current densities (>500 mA cm^{-2}), marking considerable progress at the lab scale. Nonetheless, direct comparison of these performance metrics is challenging due to inconsistencies in catalyst loading, electrode surface area, cell design, and operating conditions across different studies. Therefore, the fundamental objective is to bridge the gap between academic evaluation methods and industrial standards to accelerate the PEMWE commercialization.

In laboratory-level research, the overpotential at a current density of 10 mA cm^{-2} performed in three-electrode systems is widely used as a benchmark for evaluating the intrinsic activity of electrocatalysts. This relatively mild condition helps minimize bubble formation and mass transport limitations, thereby providing a more accurate reflection of the dynamic kinetic behavior of catalysts. However, under the high current densities (>1 A cm^{-2}) and elevated temperatures typical of PEM electrolysis configurations, vigorous gas evolution leads to substantial bubble accumulation on catalyst surfaces. This can severely impede mass transport and result in significant performance deviation. Additionally, under such harsh operating conditions, catalysts are susceptible to structural reconstruction, migration, and dissolution, further degrading their catalytic performance. Therefore, the rational design of advanced Ir/Ru-based catalysts must prioritize long-term stability at high current densities (>1 A cm^{-2}) to meet the requirements for future PEM applications. Given this objective, evaluating catalyst performance within actual PEM configurations becomes indispensable for laboratory research, unde rscoring the urgent need for standardized testing protocols.

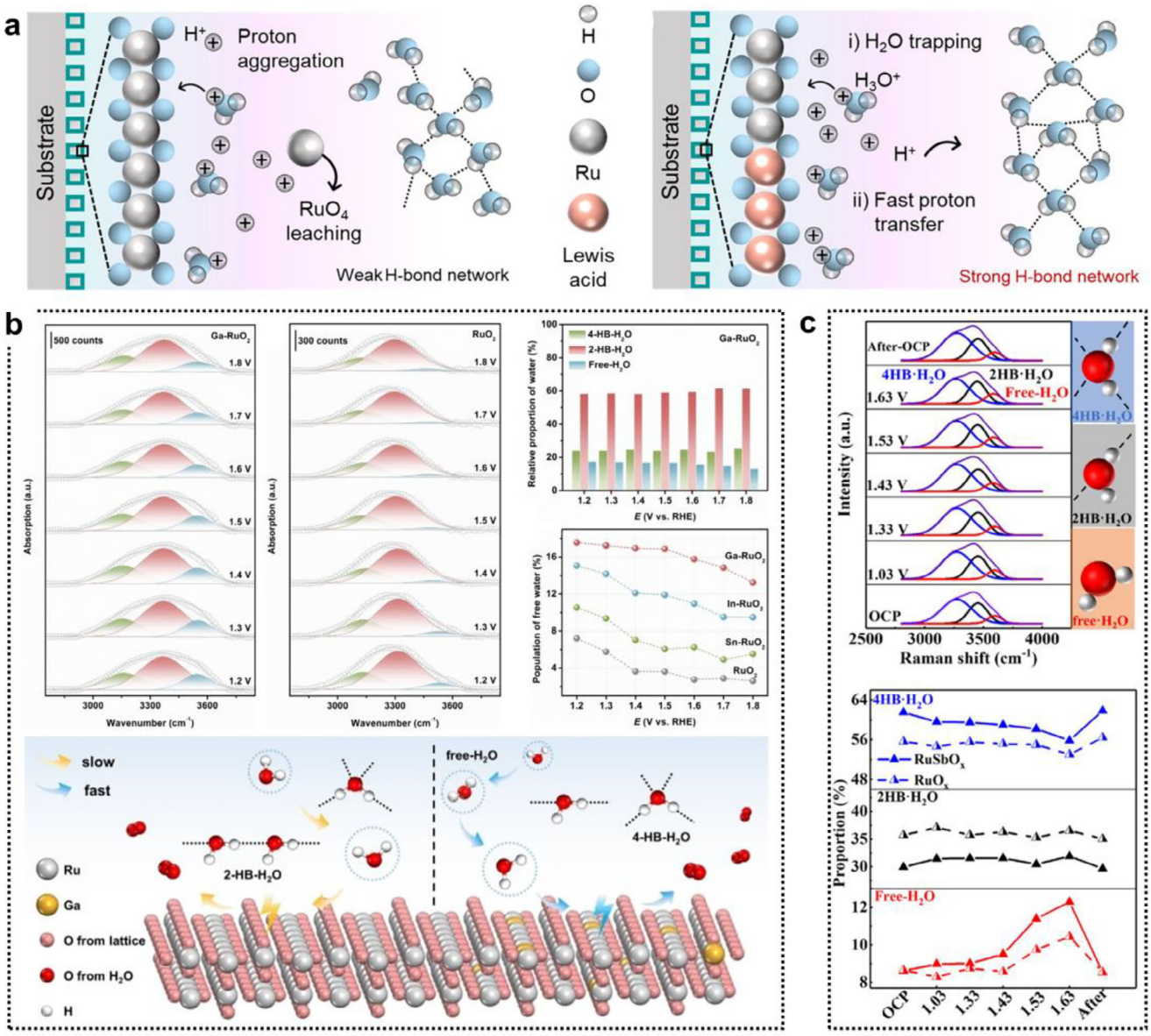

Figure 17. Interfacial water microenvironment mechanism. a) Schematic diagram of the proton transfer process in different H-bond environments. b) In situ Raman analysis of Ga–RuO_2 and RuO_2 samples. The H_2O vibration peak can be divided into three components: 4–HB–H_2O, 4–HB–H_2O and free–H_2O. c) In situ Raman analysis of Sb single-atom-doped RuO_x ($RuSbO_x$) and RuO_x.

Beyond the catalyst itself, other critical components of PEM systems—such as the catalyst layer (CL) integration, porous transport layer (PTL), gas diffusion layer (GDL), and bipolar plate (BPP)—also play vital roles in determining device performance (**Figure** 18a).[234–236] These elements crucially affect overall conductivity and mass transport, which are essential for efficient operation, yet are often overlooked in fundamental laboratory studies. Consequently, many catalysts that exhibit excellent performance in three-electrode systems suffer from rapid degradation under high current densities in PEM electrolyzers. Therefore, optimizing key components is critical to enhancing the performance and durability of PEM systems. Such optimization not only helps reveal the intrinsic activity of catalysts under industrially relevant conditions but also offers crucial insights into their practical applicability. Here, we focus specifically on the anode sites, including the CL, PTL, and their interfacial contact, offering guidance for performance optimization in laboratory-scale PEM devices.

6.1. Catalyst Layers (CLs)

Catalyst layers (CLs) integration plays a critical role in determining the activity and durability of the MEA (Figure 18b).[237] Under harsh reaction conditions—such as high temperature, high pressure, and high current density—the CL produces abundant

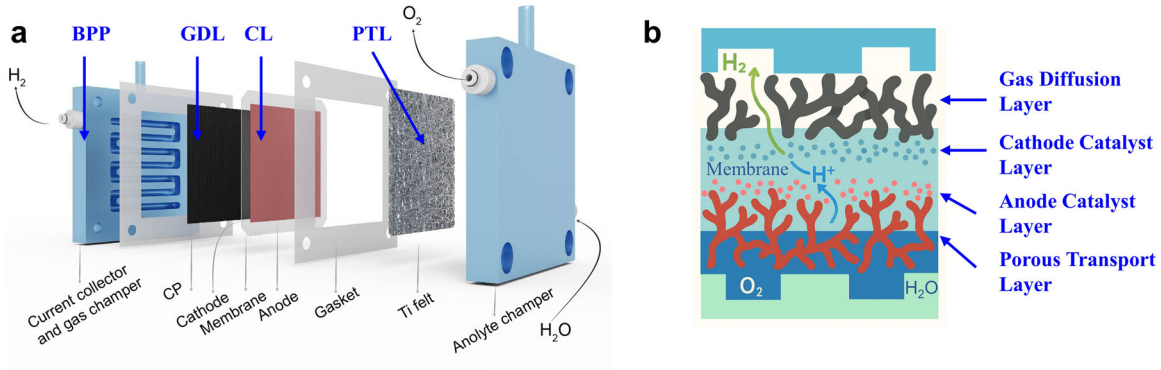

Figure 18. PEM device and components. a) Schematic illustration of PEM water electrolyzer. This figure is obtained permission for reproduction. b) Schematic illustration of the PEM components, including GDL, CL, and PTL.

bubbles that accumulate on the catalyst surface. This bubble coverage not only blocks active sites but also obstructs proton transport pathways, resulting in performance decay. Furthermore, the catalyst surface is susceptible to structural reconstruction, migration, and metal dissolution under high operational current densities, shortening the catalyst's lifespan and compromising its activity due to the leaching of impurity elements into the electrolyte. The primary goal is to engineer a catalyst structure that maximizes the accessibility of active sites while ensuring efficient transport of protons, electrons, water, and oxygen. For instance, researchers have developed proton-abundant H_xIrO_y nanosheet catalysts.[238] These ultrathin layer with rich protons enables high conductivity, thereby reducing the CL's dependency on ionomers for proton conduction. As a result, ≈85% of the catalyst layer remains free of ionomer, maximizing the exposure of active sites and accelerating electron transfer and gas release. Another study incorporated nanochannels into an Ir-based catalyst to improve mass transport.[239] The nanochannel electrode achieved a voltage reduction of 190 mV at 9 A cm^{-2} compared to a counterpart without nanochannels. These nanochannels were found to facilitate the transport of water and oxygen across the CL/PTL interface, leading to enhanced membrane hydration and reduced contact resistance. Furthermore, the nanochannel electrode exhibits a larger electrochemically active area and higher catalyst utilization, which effectively lowers the Ir loading. These results are of significant value for the development and design of catalyst layers (CLs), offering a promising low-iridium electrode material for the large-scale production of clean hydrogen.

6.2. Porous Transport Layer (PTL)

Titanium-based materials—such as Ti felt, Ti mesh, and Ti foam are commonly used as PTLs owing to their high electrical conductivity and excellent corrosion resistance in an acidic environment. However, under the harsh operational conditions in PEMWE, a passive titanium oxide layer forms, increasing interfacial contact resistance and reducing system efficiency. Surface deposition of noble metals (Au, Pt etc.)[240,241] or oxides[242] on Ti-PTLs has been proven effective in reducing interfacial resistance, suppressing surface passivation, and enhancing durability. In addition, PTL properties, including pore size and porosity, significantly influence contact resistance.[243,244] Studies indicate that optimal PTL performance is achieved with pore diameters between 10 and 13 µm and a porosity of ≈30%, which minimizes the interfacial contact resistance between the PTL and CL.

Moreover, non-uniform catalyst thickness can cause poor interfacial contact with the PTLs, leading to higher ohmic losses.[245] Several factors influence the quality of the catalyst coating on MEA, including ionomer content, dispersion stability, viscosity, choice of slurry solvent, hydrophilicity of the gas diffusion layer (GDL) substrate, spray gun parameters, and so on. To achieve high-quality and uniform MEAs, laboratories may employ syringe or peristaltic pumps to ensure precise and steady slurry delivery. Or, mounting the spray gun on a computer-controlled XYZ three-axis motion stage enables raster-scanning deposition, eliminating the variability inherent in manual spraying and ensuring consistent, reproducible spraying.

The high cost of PEM electrolyzers is also a major barrier to the widespread adoption of green hydrogen production. In PEM system, the catalyst materials are platinum groups metals (PGM), accounting for 25% of the stack cost.[246] A primary contributor to this expense is the anode catalyst, which typically utilizes Ir—a precious metal that is extremely scarce and expensive. Commercial stacks require Ir loadings of ≈1–2 mg_{Ir} cm^{-2} to achieve the necessary activity and durability, resulting in low catalyst utilization efficiency.[247,248] Thus, reducing both the iridium loading and developing alternative, low-cost catalyst materials is not merely an economic imperative but a fundamental necessity.[249] To tackle this issue, strategies such as highly dispersed supported catalysts or nanostructured thin-film catalysts have been proposed to significantly lower iridium content. For instance, Tao et al. introduced a hierarchical catalyst layer composed of sub-nanosheets on nanowires, which effectively reduced the iridium loading to 0.35 mg_{Ir} cm^{-2} while simultaneously enhancing the overall performance of PEM water electrolyzers.[250]

In summary, we have outlined the key components of PEMWE systems—namely, catalyst layers (CLs) and porous transport layers (PTLs)—and discussed critical factors such as catalysts design, interfaces contact, ionomers, and impurities that require attention in laboratory-scale research. Future academic studies should focus on reducing the reliance on precious Ir metals,

enhancing operational durability, and lowering overall system costs. Through advances in the design of low-cost catalysts and integrated optimization of core components, PEMWE technology is poised to enable wider commercial adoption in large-scale green hydrogen production.

7. Conclusion and Perspectives

This paper comprehensively summarizes the development of single-atom-doping (SAD) methods for regulating Ir- and Ru-based electrocatalysts for the acidic OER. By significantly increasing the intrinsic activity and, crucially, long-term stability under harsh acidic OER conditions, these SAD-engineered Ir/Ru-based catalysts directly address the major bottlenecks of high precious metal cost and insufficient durability, which hinder widespread PEMWE commercialization.

In this review, we summarize common synthetic strategies developed for precisely anchoring isolated heteroatoms—such as transition metals, rare-earth metals, and p-block elements—into Ir- or Ru-based oxide matrices. These approaches create unique catalytic sites with tailored electronic and geometric structures. Crucially, such single-atom sites are incorporated into the crystal lattice via substitutional doping, forming localized Ir(Ru)–O–M interactions and inducing a range of regulatory effects. For instance, doping with metal atoms that differ significantly in atomic size (e.g., Pt, La) can introduce lattice strain (compressive or tensile), which modulates the *d*-band center of the active metal and optimizes the adsorption strength of reaction intermediates, thereby enhancing catalytic activity. High-valence metal dopants (e.g., Zr^{4+}, Ta^{4+}, Nb^{5+}, Re^{7+}) enable electron transfer to Ru sites owing to their strong electronegativity, suppressing overoxidation and dissolution of Ru and thus improving structural stability. Low-valent dopants (e.g., Pt^{+}, Ag^{+}, Zn^{+}, Pd^{2+}) can facilitate the formation of high-valent active species and additional oxygen vacancies, synergistically optimizing the binding energy of intermediates and enhancing intrinsic catalytic activity. Several reports emphasize the role of single-atom sites (e.g., Sb, Ta) in optimizing the AEM pathway by serving as proton-acceptor sites, accelerating proton transfer and improving OER reaction kinetics. Other studies highlight that certain dopants (e.g., V, Ga) can alter the reaction pathway from the conventional AEM to the direct O–O coupling route (OPM) by forming localized symmetric structures. This shift lowers the energy barrier of RDS and reduces lattice oxygen participation, simultaneously enhancing OER activity and stability. Additionally, attention has been drawn to the regulation of the interfacial water environment (e.g., by Sb, Ga) for facilitating water dissociation, reducing the driving force for OER activation. In cases of dual-atom or multi-atom doping catalysts, the active sites may be governed by a specific reaction mechanism; however, their behavior is not attributable to a single factor alone. Rather, it is more likely the result of a synergistic enhancement arising from the interplay of multiple elements—such as lattice strain, electron transfer, and defect/vacancy engineering. Investigating these synergistic mechanisms offers a clearer blueprint and deeper insights into the complexity of heterogeneous interfaces.

Given these design protocols for advanced SAD catalysts, the research community has turned its attention to the structural evolution of the SAD sites, seeking to answer two fundamental mechanistic questions: How do these sites reconstruct during the OER, and are they truly the active sites? In fact, most of these SAD sites are generally inactive toward OER and function primarily as structural stabilizers or electronic modulators to enhance the catalytic performance of active sites. This is particularly evident for corrosion- and oxidation-resistant high-valence elements such as Zr and Nb, which form strong interactions within the crystal lattice and resist structural reconstruction. In contrast, certain low-valence elements may undergo oxidation during electron transfer, potentially leading to dissolution in extreme cases. Here, the use of SAD with low loading and uniform dispersion helps control the extent of dopant dissolution, thereby maintaining the overall structural integrity. However, since catalytic reactions occur predominantly at surfaces and interfaces, the dissolution of doped elements from the catalyst surface remains a critical challenge. In specific scenarios—such as when functioning as proton acceptors to optimize the AEM pathway or to establish an OPM—SAD sites can serve as adsorption sites for certain oxy-intermediates within Ir/Ru-O-M structure, facilitating more efficient adsorption-desorption processes. In summary, the structural reconstruction of those SAD sites can be mitigated by precise coordination control. The combination of synchrotron radiation techniques (e.g., XAFS) with theoretical modeling (e.g., DFT, MDs) is indispensable for unraveling their true nature and dynamic evolution under operating conditions.

Despite significant progress, single-atom dispersed (SAD) catalysts still face inherent challenges, including low dopant loading, high loading non-uniformity, and susceptibility to surface leaching. Moreover, the complexity of the OER—driven by the dynamic evolution of active sites, SAD sites, and the interfacial microenvironment—necessitates more advanced characterization techniques to elucidate the mechanistic details of the synergetic effect, SAD regulation, and degradation process. Furthermore, establishing standardized testing protocols, integrated with rational catalyst design and proton exchange membrane (PEM) component optimization, is crucial for translating laboratory-developed catalysts into practical PEM water electrolysis (PEMWE) applications. Therefore, concerted efforts are essential to overcome these barriers, with priority given to the following key directions:

1) **High loading and dispersion of SAD sites**

To prevent the aggregation of single atoms into nanoparticles, the metal loading is typically kept very low (often below 1–5 wt%). This limitation on the SAD sites density per unit area compromises their systematic modulation of the host metal and hampers the establishment of a reliable catalytic mechanism. Consequently, securing a high and uniform loading of isolated SAD atoms is a critical premise for the rational design of next-generation SAD catalysts. Beyond the selection of a synthesis strategy, successful implementation hinges on addressing two critical factors. First, the pyrolysis or annealing process requires precise control, with an optimal temperature range of 500–800 °C to stabilize single-atom sites without inducing sintering. Second, it is essential to establish a strong metal-support interaction (SMSI) by utilizing defect sites (e.g., vacancies, edges) or functional groups (e.g., —OH, —COOH)

to form coordination bonds that effectively prevent atomic aggregation.

1) **Suppressing surface leaching of SAD sites**

Single-atom dopants in the Ir/Ru oxides are prone to dissolution and aggregation under harsh acidic and oxidizing conditions, leading to rapid performance decay. Exploring novel architecture to act as a trap or cage that immobilizes the dispersed doping atoms is highly recommended. For example, architectures rich in atomic vacancies (e.g., cation vacancies in spinel oxides) or edge sites provide strong anchoring points, drastically increasing the energy required for a single atom to detach or migrate. The use of support materials and core–shell architectures serves as a robust physical barrier that isolates the internal SAD active sites from the corrosive electrolyte, thereby effectively suppressing their leaching and aggregation.

1) **Deepening the mechanistic understanding**

Doping in many cases might introduce extraneous lattice boundaries, defects, or oxygen vacancies into the lattice, which can perturb catalytic activity and stability. This dynamic restructuring makes it extremely challenging to identify the true catalytic active sites—a state that is often unstable and difficult to isolate. Meanwhile, the dynamic evolution of dopant sites under operational conditions, coupled with issues such as, atoms agglomeration, segregation, and leaching, further complicates mechanistic studies. Thus, relying on current characterization techniques (XPS, operando XAS, in situ FTIR, in situ Raman, DEMS etc.) is often insufficient. Techniques like nano-tomography, atom probe tomography (APT), and time of flight mass spectrometer (TOF-MS) are promising to pinpoint the exact chemical composition and geometric structure. Correlation of multimodal operando techniques (4D operando TEM and high-energy-resolution time-resolved X-ray spectroscopy)[251] serves as a powerful platform to comprehensively investigate the structural dynamics under electrochemical conditions. Future research will need to integrate these next-generation techniques to deepen our fundamental understanding of the complex structural evolution of catalysts.

1) **Advancing theoretical methodologies**

Machine learning (ML) and high-throughput computational screening have emerged as powerful tools in catalyst design, overcoming the fundamental constraints of traditional "trial-and-error" approaches. Machine learning can handle more complex material descriptors and experimental conditions, predicting new material combinations with desirable properties, such as high-entropy alloy catalysts.[252] Complementarily, high-throughput screening efficiently identifies optimal dopant-host pairs, as exemplified by the MgIrRu oxide catalyst, which has been experimentally validated to achieve a low overpotential of 191 mV and outstanding mass activity.[253] The integration of ML and high-throughput computational screening with experimental validation is revolutionizing electrocatalyst development—significantly accelerating discovery, reducing costs, and yielding deeper mechanistic insights. These approaches have become essential to the rational design of sophisticated, next-generation catalysts.

1) **Developing testing protocols**

PEM water electrolyzers entail more complex degradation mechanisms than traditional aqueous electrolyte systems. These include substrate passivation, metal dissolution, catalyst detachment, bubble accumulation, and the degradation of membranes and ionomers. This complexity underscores the pressing need to establish consistent testing protocols, incorporating accelerated degradation procedures, standardized decay assessment (e.g.,μV/h), real-time resistance monitoring, and uniform data reporting guidelines. Furthermore, these standardization efforts must align with practical PEMWE operating conditions—such as active area, temperature, pressure, and electrolyte flow rate—to ensure relevance. Ultimately, MEA-level validation is indispensable to ensure that lab-scale research possesses practical relevance and is translatable to real devices.

Acknowledgements

Q.Z. and J.T. contributed equally to this work. C.X. acknowledges the "Pioneer" and "Leading Goose" R&D Program of Zhejiang (No. 2023C03017), the National Key Research and Development Program of China (2024YFB4105700), NSFC (52171201), and the Natural Science Foundation of Sichuan Province (2025NSFJQ0017). J.T. acknowledges the National Natural Science Foundation of China (22305029). J.T. acknowledges the University Fundamental Research Funding (ZYGX2025XJ013). Q.J. acknowledges the National Natural Science Foundation of China (22405035), the Natural Science Foundation of Sichuan Province (No. 2024NSFSC1104), the Huzhou Science and Technology Bureau (No. 2023GZ02).

Conflict of Interest

The authors declare no conflict of interest.

Keywords

proton exchange membrane water electrolysis (PEMWE), oxygen evolution reaction (OER), iridium (Ir)- and ruthenium (Ru)-based oxides, single-atom doping, reaction mechanisms

Received: August 7, 2025
Revised: October 1, 2025
Published online:

[1] R. Ram, L. Xia, H. Benzidi, A. Guha, V. Golovanova, A. Garzón Manjón, D. Llorens Rauret, P. Sanz Berman, M. Dimitropoulos, B. Mundet, E. Pastor, V. Celorrio, C. A. Mesa, A. M. Das, A. Pinilla-Sánchez, S. Giménez, J. Arbiol, N. López, F. P. García de Arquer, *Science* **2024**, *384*, 1373.
[2] S. Chu, A. Majumdar, *Nature* **2012**, *488*, 294.
[3] F. Zhao, B. Wen, W. Niu, Z. Chen, C. Yan, A. Selloni, C. G. Tully, X. Yang, B. E. Koel, *J. Am. Chem. Soc.* **2021**, *143*, 15616.
[4] M. Carmo, D. L. Fritz, J. Mergel, D. Stolten, *Int. J. Hydrogen Energy* **2013**, *38*, 4901.
[5] J. Gao, C.-Q. Xu, S.-F. Hung, W. Liu, W. Cai, Z. Zeng, C. Jia, H. M. Chen, H. Xiao, J. Li, Y. Huang, B. Liu, *J. Am. Chem. Soc.* **2019**, *141*, 3014.

[6] Y.-R. Zheng, J. Vernieres, Z. Wang, K. Zhang, D. Hochfilzer, K. Krempl, T.-W. Liao, F. Presel, T. Altantzis, J. Fatermans, S. B. Scott, N. M. Secher, C. Moon, P. Liu, S. Bals, S. Van Aert, A. Cao, M. Anand, J. K. Nørskov, J. Kibsgaard, I. Chorkendorff, *Nat. Energy* **2022**, *7*, 55.
[7] Y. Lin, Y. Dong, X. Wang, L. Chen, *Adv. Mater.* **2022**, *35*, 2210565.
[8] X. Wang, H. Jang, S. Liu, Z. Li, X. Zhao, Y. Chen, M. G. Kim, Q. Qin, X. Liu, *Adv. Energy Mater.* **2023**, *13*, 2301673.
[9] O. Diaz-Morales, S. Raaijman, R. Kortlever, P. J. Kooyman, T. Wezendonk, J. Gascon, W. T. Fu, M. T. M. Koper, *Nat. Commun.* **2016**, *7*, 12363.
[10] Z. Shi, Y. Wang, J. Li, X. Wang, Y. Wang, Y. Li, W. Xu, Z. Jiang, C. Liu, W. Xing, J. Ge, *Joule* **2021**, *5*, 2164.
[11] H. N. Nong, T. Reier, H.-S. Oh, M. Gliech, P. Paciok, T. H. T. Vu, D. Teschner, M. Heggen, V. Petkov, R. Schlögl, T. Jones, P. Strasser, *Nat. Catal.* **2018**, *1*, 841.
[12] Z. Lei, T. Wang, B. Zhao, W. Cai, Y. Liu, S. Jiao, Q. Li, R. Cao, M. Liu, *Adv. Energy Mater.* **2020**, *10*, 2000478.
[13] G.-Q. Liu, Y. Yang, X.-L. Zhang, H.-H. Li, P.-C. Yu, M.-R. Gao, S.-H. Yu, *Small* **2024**, *20*, 2306914.
[14] Z.-Y. Wu, F.-Y. Chen, B. Li, S.-W. Yu, Y. Z. Finfrock, D. M. Meira, Q.-Q. Yan, P. Zhu, M.-X. Chen, T.-W. Song, Z. Yin, H.-W. Liang, S. Zhang, G. Wang, H. Wang, *Nat. Mater.* **2023**, *22*, 100.
[15] G. Gao, Z. Sun, X. Chen, G. Zhu, B. Sun, Y. Yamauchi, S. Liu, *Appl. Catal., B* **2024**, *343*, 123584.
[16] S. Geiger, O. Kasian, M. Ledendecker, E. Pizzutilo, A. M. Mingers, W. T. Fu, O. Diaz-Morales, Z. Li, T. Oellers, L. Fruchter, A. Ludwig, K. J. J. Mayrhofer, M. T. M. Koper, S. Cherevko, *Nat. Catal.* **2018**, *1*, 508.
[17] S. Hao, H. Sheng, M. Liu, J. Huang, G. Zheng, F. Zhang, X. Liu, Z. Su, J. Hu, Y. Qian, L. Zhou, Y. He, B. Song, L. Lei, X. Zhang, S. Jin, *Nat. Nanotechnol.* **2021**, *16*, 1371.
[18] L. Zhou, Y. Shao, F. Yin, J. Li, F. Kang, R. Lv, *Nat. Commun.* **2023**, *14*, 7644.
[19] K. Du, L. Zhang, J. Shan, J. Guo, J. Mao, C.-C. Yang, C.-H. Wang, Z. Hu, T. Ling, *Nat. Commun.* **2022**, *13*, 5448.
[20] Y. Yao, S. Hu, W. Chen, Z.-Q. Huang, W. Wei, T. Yao, R. Liu, K. Zang, X. Wang, G. Wu, W. Yuan, T. Yuan, B. Zhu, W. Liu, Z. Li, D. He, Z. Xue, Y. Wang, X. Zheng, J. Dong, C.-R. Chang, Y. Chen, X. Hong, J. Luo, S. Wei, W.-X. Li, P. Strasser, Y. Wu, Y. Li, *Nat. Catal.* **2019**, *2*, 304.
[21] S. Hao, M. Liu, J. Pan, X. Liu, X. Tan, N. Xu, Y. He, L. Lei, X. Zhang, *Nat. Commun.* **2020**, *11*, 5368.
[22] Z. W. Seh, J. Kibsgaard, C. F. Dickens, I. Chorkendorff, J. K. Nørskov, T. F. Jaramillo, *Science* **2017**, *355*, aad4998.
[23] C. Hu, K. Yue, J. Han, X. Liu, L. Liu, Q. Liu, Q. Kong, C.-W. Pao, Z. Hu, K. Suenaga, D. Su, Q. Zhang, X. Wang, Y. Tan, X. Huang, *Sci. Adv.* **2023**, *9*, adf9144.
[24] R. Li, H. Wang, F. Hu, K. C. Chan, X. Liu, Z. Lu, J. Wang, Z. Li, L. Zeng, Y. Li, X. Wu, Y. Xiong, *Nat. Commun.* **2021**, *12*, 3540.
[25] F. Liao, K. Yin, Y. Ji, W. Zhu, Z. Fan, Y. Li, J. Zhong, M. Shao, Z. Kang, Q. Shao, *Nat. Commun.* **2023**, *14*, 1248.
[26] Q. Dang, H. Lin, Z. Fan, L. Ma, Q. Shao, Y. Ji, F. Zheng, S. Geng, S.-z. Yang, N. Kong, W. Zhu, Y. Li, F. Liao, X. Huang, M. Shao, *Nat. Commun.* **2021**, *12*.
[27] T. Zhao, R. Du, Q. Fang, G. Hao, G. Liu, Zhong, J. Li, Q. Zhao, *Small* **2024**, *21*, 2410311
[28] S. Chen, C. Wang, F. Gao, Y. Yang, M. Huang, H. Tong, Z. Cheng, P. Wang, P. Wang, J. Tu, X. Zeng, Q. Chen, *J. Mater. Chem. A* **2022**, *10*, 3722.
[29] W. Zhu, X. Song, F. Liao, H. Huang, Q. Shao, K. Feng, Y. Zhou, M. Ma, J. Wu, H. Yang, H. Yang, M. Wang, J. Shi, J. Zhong, T. Cheng, M. Shao, Y. Liu, Z. Kang, *Nat. Commun.* **2023**, *14*, 5365.
[30] K. Miao, W. Jiang, Z. Chen, Y. Luo, D. Xiang, C. Wang, X. Kang, *Adv. Mater.* **2024**, *36*, 2308490.
[31] J. Zheng, Z. Wang, *Chem Catalysis* **2024**, *4*, 101091.
[32] J. Yin, J. Jin, M. Lu, B. Huang, H. Zhang, Y. Peng, P. Xi, C.-H. Yan, *J. Am. Chem. Soc.* **2020**, *142*, 18378.
[33] J. Shan, C. Ye, S. Chen, T. Sun, Y. Jiao, L. Liu, C. Zhu, L. Song, Y. Han, M. Jaroniec, Y. Zhu, Y. Zheng, S.-Z. Qiao, *J. Am. Chem. Soc.* **2021**, *143*, 5201.
[34] F. Luo, H. Hu, X. Zhao, Z. Yang, Q. Zhang, J. Xu, T. Kaneko, Y. Yoshida, C. Zhu, W. Cai, *Nano Lett.* **2020**, *20*, 2120.
[35] X.-P. Yang, Z.-Z. Wu, Y.-C. Li, S.-P. Sun, Y.-C. Zhang, J.-W. Duanmu, P.-G. Lu, X.-L. Zhang, F.-Y. Gao, Y. Yang, Y.-H. Wang, P.-C. Yu, S.-K. Li, M.-R. Gao, *Nat. Commun.* **2025**, *16*, 2811.
[36] Y. Hao, S.-F. Hung, W.-J. Zeng, Y. Wang, C. Zhang, C.-H. Kuo, L. Wang, S. Zhao, Y. Zhang, H.-Y. Chen, S. Peng, *J. Am. Chem. Soc.* **2023**, *145*, 23659.
[37] Z. Shi, J. Li, J. Jiang, Y. Wang, X. Wang, Y. Li, L. Yang, Y. Chu, J. Bai, J. Yang, J. Ni, Y. Wang, L. Zhang, Z. Jiang, C. Liu, J. Ge, W. Xing, *Angew. Chem., Int. Ed.* **2022**, *61*, 202212341.
[38] S. Wu, Z. Chen, Z. Qian, Z. Zhang, Y. Sun, X. Zhang, H. Tao, Q. Zhang, S. Xie, Y. Wang, *Adv. Funct. Mater.* **2025**, *35*, 2417766.
[39] M. van der Merwe, R. Garcia-Diez, L. Lahn, R. E. Wibowo, J. Frisch, M. Gorgoi, W. Yang, S. Ueda, R. G. Wilks, O. Kasian, M. Bär, *ACS Catal.* **2023**, *13*, 15427.
[40] W. Zhao, F. Xu, L. Liu, M. Liu, B. Weng, *Adv. Mater.* **2023**, *35*, 2308060.
[41] S. Zhao, S.-F. Hung, L. Deng, W.-J. Zeng, T. Xiao, S. Li, C.-H. Kuo, H.-Y. Chen, F. Hu, S. Peng, *Nat. Commun.* **2024**, *15*, 2728.
[42] Y. Wang, M. Zhang, Z. Kang, L. Shi, Y. Shen, B. Tian, Y. Zou, H. Chen, X. Zou, *Nat. Commun.* **2023**, *14*, 5119.
[43] X. Xiong, J. Tang, Y. Ji, W. Xue, H. Wang, C. Liu, H. Zeng, Y. Dai, H.-J. Peng, T. Zheng, C. Xia, X. Liu, Q. Jiang, *Adv. Energy Mater.* **2024**, *14*, 2304479.
[44] K. Lee, J. Shim, H. Y. Jang, H. S. Lee, H. Shin, B.-H. Lee, M. S. Bootharaju, K.-S. Lee, J. Lee, S. Lee, Y.-H. Lee, C. W. Lee, Y. Jung, G. Deng, S. Yoo, S. Back, Y.-E. Sung, T. Hyeon, *Chem* **2023**, *9*, 3600.
[45] Z.-X. Qian, C.-K. Peng, M.-F. Yue, L.-C. Hsu, J.-S. Zeng, D.-Y. Wei, Z.-Y. Du, G.-Y. Xu, H. Zhang, J.-H. Tian, S.-Y. Chen, Y.-G. Lin, J.-F. Li, *Small Methods* **2024**, *8*, 2301504.
[46] M. Long, S. Lai, K. Miao, W. Jiang, W. Fan, X. Kang, *Angew. Chem., Int. Ed.* **2025**, *64*, 202419956.
[47] L. Yao, F. Zhang, S. Yang, H. Zhang, Y. Li, C. Yang, H. Yang, Q. Cheng, *Adv. Mater.* **2024**, *36*, 2314049.
[48] J. Chen, J. Ma, T. Huang, Q. Liu, X. Liu, R. Luo, J. Xu, X. Wang, T. Jiang, H. Liu, Z. Lv, T. Yao, G. Wang, X. Zheng, Z. Li, W. Chen, *Angew. Chem., Int. Ed.* **2025**, *64*, 202503330.
[49] A. L. Maulana, P.-C. Chen, Z. Shi, Y. Yang, C. Lizandara-Pueyo, F. Seeler, H. D. Abruña, D. Muller, K. Schierle-Arndt, P. Yang, *Nano Lett.* **2023**, *23*, 6637.
[50] H.-J. Qiu, G. Fang, J. Gao, Y. Wen, J. Lv, H. Li, G. Xie, X. Liu, S. Sun, *ACS Mater. Lett.* **2019**, *1*, 526.
[51] Z. Jin, J. Lv, H. Jia, W. Liu, H. Li, Z. Chen, X. Lin, G. Xie, X. Liu, S. Sun, H.-J. Qiu, *Small* **2019**, *15*, 1904180.
[52] Y. Wen, P. Chen, L. Wang, S. Li, Z. Wang, J. Abed, X. Mao, Y. Min, C. T. Dinh, P. D. Luna, R. Huang, L. Zhang, L. Wang, L. Wang, R. J. Nielsen, H. Li, T. Zhuang, C. Ke, O. Voznyy, Y. Hu, Y. Li, W. A. Goddard Iii, B. Zhang, H. Peng, E. H. Sargent, *J. Am. Chem. Soc.* **2021**, *143*, 6482.
[53] X. Zheng, J. Yang, P. Li, Q. Wang, J. Wu, E. Zhang, S. Chen, Z. Zhuang, W. Lai, S. Dou, W. Sun, D. Wang, Y. Li, *Sci. Adv.* **2023**, *9*, adi8025.
[54] S. Chen, S. Zhang, L. Guo, L. Pan, C. Shi, X. Zhang, Z.-F. Huang, G. Yang, J.-J. Zou, *Nat. Commun.* **2023**, *14*, 4127.

[55] J. Zhang, X. Fu, S. Kwon, K. Chen, X. Liu, J. Yang, H. Sun, Y. Wang, T. Uchiyama, Y. Uchimoto, S. Li, Y. Li, X. Fan, G. Chen, F. Xia, J. Wu, Y. Li, Q. Yue, L. Qiao, D. Su, H. Zhou, W. A. Goddard, Y. Kang, *Science* **2025**, *387*, 48.
[56] L. Li, G. Zhang, C. Zhou, F. Lv, Y. Tan, Y. Han, H. Luo, D. Wang, Y. Liu, C. Shang, L. Zeng, Q. Huang, R. Zeng, N. Ye, M. Luo, S. Guo, *Nat. Commun.* **2024**, *15*, 4974.
[57] W. Zhu, F. Yao, K. Cheng, M. Zhao, C.-J. Yang, C.-L. Dong, Q. Hong, Q. Jiang, Z. Wang, H. Liang, *J. Am. Chem. Soc.* **2023**, *145*, 17995.
[58] D. Zhang, M. Li, X. Yong, H. Song, G. I. N. Waterhouse, Y. Yi, B. Xue, D. Zhang, B. Liu, S. Lu, *Nat. Commun.* **2023**, *14*, 2517.
[59] W. Liu, G. Long, Z. Xiang, T. Ren, J. Piao, K. Wan, Z. Fu, Z. Liang, *Angew. Chem., Int. Ed.* **2024**, *63*, 202411014.
[60] N. Zhang, J. Du, N. Zhou, D. Wang, D. Bao, H. Zhong, X. Zhang, *Chin. J. Catal.* **2023**, *53*, 134.
[61] W. Zhu, M. Ma, D. Gao, J. Chen, H. Huang, K. Feng, Q. Wang, J. Wu, P. Li, J. Guo, Z. Fan, J. Zhong, Q. Shao, F. Liao, Y. Liu, M. Shao, Z. Kang, *Angew. Chem., Int. Ed.* **2025**, *64*, 202423353.
[62] S.-Y. Lu, B. Huang, M. Sun, M. Luo, M. Jin, H. Yang, Q. Zhang, H. Liu, P. Zhou, Y. Chao, K. Yin, C. Shang, J. Wang, Y. Wang, F. Lv, L. Gu, S. Guo, *Nat. Synthesis* **2023**.
[63] L. Li, Z. Cheng, J. Su, B. Song, H. Yu, Y. Ji, Q. Shao, J. Lu, *J. Mater. Chem. A* **2023**, *11*, 25268.
[64] W. He, X. Tan, Y. Guo, Y. Xiao, H. Cui, C. Wang, *Angew. Chem., Int. Ed.* **2024**, *63*, 202405798.
[65] Y. H. Yun, J. Choi, Y. Park, H. Park, G. Doo, M. Kim, S. S. Han, J. H. Park, S. Lee, C. Lee, H.-S. Cho, *Small* **2025**, 2503601.
[66] F.-F. Zhang, C.-Q. Cheng, J.-Q. Wang, L. Shang, Y. Feng, Y. Zhang, J. Mao, Q.-J. Guo, Y.-M. Xie, C.-K. Dong, Y.-H. Cheng, H. Liu, X.-W. Du, *ACS Energy Lett.* **2021**, *6*, 1588.
[67] A. M. Harzandi, S. Shadman, A. S. Nissimagoudar, D. Y. Kim, H.-D. Lim, J. H. Lee, M. G. Kim, H. Y. Jeong, Y. Kim, K. S. Kim, *Adv. Energy Mater.* **2021**, *11*, 2003448.
[68] J. Tang, X. Liu, X. Xiong, Q. Zeng, Y. Ji, C. Liu, J. Li, H. Zeng, Y. Dai, X. Zhang, C. Li, H. Peng, Q. Jiang, T. Zheng, C.-W. Pao, C. Xia, *Adv. Mater.* **2024**, *36*, 2407394.
[69] X. Wang, Z. Li, H. Jang, C. Chen, S. Liu, L. Wang, M. G. Kim, J. Cho, Q. Qin, X. Liu, *Adv. Energy Mater.* **2025**, *15*, 2403388.
[70] Z. Niu, Z. Qiao, P. Sun, J. Chen, S. Wang, F. Huo, D. Cao, *Small* **2025**, *21*, 2502088.
[71] H. Wang, C. Lin, L. Tan, J. Shen, X. Wu, X. Pan, Y. Zhao, H. Zhang, Y. Sun, B. Mei, H.-D. Um, Q. Xiao, W. Jiang, X. Li, W. Luo, *Nat. Commun.* **2025**, *16*, 3976.
[72] C. Liu, J. Qian, Y. Ye, H. Zhou, C.-J. Sun, C. Sheehan, Z. Zhang, G. Wan, Y.-S. Liu, J. Guo, S. Li, H. Shin, S. Hwang, T. B. Gunnoe, W. A. Goddard, S. Zhang, *Nat. Catal.* **2021**, *4*, 36.
[73] Q. Qin, T. Wang, Z. Li, G. Zhang, H. Jang, L. Hou, Y. Wang, M. Gyu Kim, S. Liu, X. Liu, *J. Energy Chem.* **2024**, *88*, 94.
[74] T. Gao, X. Tang, X. Li, S. Wu, S. Yu, P. Li, D. Xiao, Z. Jin, *ACS Catal.* **2023**, *13*, 49.
[75] C. Zhou, X. Chen, S. Liu, Y. Han, H. Meng, Q. Jiang, S. Zhao, F. Wei, J. Sun, T. Tan, R. Zhang, *J. Am. Chem. Soc.* **2022**, *144*, 2694.
[76] X. Yao, Z. Song, X. Yao, Y. Guan, N. Hamada, J. Zhang, Z. Huo, L. Zhang, C. V. Singh, X. Sun, *Angew. Chem., Int. Ed.* **2024**, *63*, 202318872.
[77] Q. Qin, Z. Li, X. Zhao, H. Zhao, L. Zhai, M. Gyu Kim, J. Cho, H. Jang, S. Liu, X. Liu, *Angew. Chem., Int. Ed.* **2025**, *64*, 202413657.
[78] L. Cao, W. Liu, Q. Luo, R. Yin, B. Wang, J. Weissenrieder, M. Soldemo, H. Yan, Y. Lin, Z. Sun, C. Ma, W. Zhang, S. Chen, H. Wang, Q. Guan, T. Yao, S. Wei, J. Yang, J. Lu, *Nature* **2019**, *565*, 631.
[79] X.-M. You, B. Xu, H. Zhou, H. Qiao, X. Lv, Z. Huang, J. Pang, L. Yang, P. F. Liu, X. Guan, H. G. Yang, X. Wang, Y.-F. Yao, *ACS Nano* **2024**, *18*, 9403.
[80] F. Shen, Z. Zhang, Z. Wang, H. Ren, X. Liang, Z. Cai, S. Yang, G. Sun, Y. Cao, X. Yang, M. Hu, Z. Hao, K. Zhou, *Nat. Commun.* **2024**, *15*, 448.
[81] M. Li, X. Wang, H. Du, W. Dong, S. Ye, H. Liu, H. Sun, K. Huang, H. Li, Y. Tang, G. Fu, *Adv. Energy Mater.* **2024**, *14*, 2401716.
[82] S. Dong, P. Wang, Z. Li, L. Wei, S. Liu, Y. Yang, F. Zheng, *Adv. Funct. Mater.* **2024**, *35*, 2422166.
[83] Z. Luo, Y. Guo, C. He, Y. Guan, L. Zhang, Y. Li, Q. Zhang, C. He, X. Sun, X. Ren, *Angew. Chem., Int. Ed.* **2024**, *63*, 202405017.
[84] L. Zeng, Z. Zhao, Q. Huang, C. Zhou, W. Chen, K. Wang, M. Li, F. Lin, H. Luo, Y. Gu, L. Li, S. Zhang, F. Lv, G. Lu, M. Luo, S. Guo, *J. Am. Chem. Soc.* **2023**, *145*, 21432.
[85] H. Wang, C. Zhang, D. Zhang, L. Jiang, Y. Gao, T. Zhuang, Z. Lv, *Small* **2024**, *20*, 2403170.
[86] J. Bok, S. Y. Lee, B.-H. Lee, C. Kim, D. L. T. Nguyen, J. W. Kim, E. Jung, C. W. Lee, Y. Jung, H. S. Lee, J. Kim, K. Lee, W. Ko, Y. S. Kim, S.-P. Cho, J. S. Yoo, T. Hyeon, Y. J. Hwang, *J. Am. Chem. Soc.* **2021**, *143*, 5386.
[87] L. Zhang, Q. Wang, L. Li, M. N. Banis, J. Li, K. Adair, Y. Sun, R. Li, Z.-J. Zhao, M. Gu, X. Sun, *Nano Energy* **2022**, *93*, 106813.
[88] J. Yu, R.-T. Gao, X. Guo, N. Truong Nguyen, L. Wu, L. Wang, *Angew. Chem., Int. Ed.* **2025**, *64*, 202415975.
[89] C. Wan, Z. Zhang, S. Wang, Q. Sun, E. Liu, H. Pu, A. Zhang, Z. Chen, A. H. Shah, X. Fu, A. N. Alexandrova, Q. Jia, Y. Huang, X. Duan, *J. Am. Chem. Soc.* **2025**, *147*, 12162.
[90] W. Jiao, Z. Ren, Z. Cui, C. Ma, Z. Shang, G. Chen, R. Lu, T. Gan, Z. Wang, Y. Xiong, Y. Han, *Nat. Commun.* **2025**, *16*, 883.
[91] L. Jin, Y. Wang, Q. Li, N. Nanayakkara, Y. Liu, Q. Wang, *Appl. Catal. B: Environ. Energy* **2025**, *373*, 125328.
[92] H. Wu, Y. Wang, Z. Shi, X. Wang, J. Yang, M. Xiao, J. Ge, W. Xing, C. Liu, *J. Mater. Chem. A* **2022**, *10*, 13170.
[93] H. Wu, J. Chang, J. Yu, S. Wang, Z. Hu, G. I. N. Waterhouse, X. Yong, Z. Tang, J. Chang, S. Lu, *Nat. Commun.* **2024**, *15*, 10315.
[94] M. Yang, X. Guan, Z. Shi, H. Wu, Y. Cheng, Z. Wang, W. Liu, F. Xiao, M. Shao, M. Xiao, C. Liu, W. Xing, *Small* **2025**, 2411117.
[95] H. Jin, X. Liu, P. An, C. Tang, H. Yu, Q. Zhang, H.-J. Peng, L. Gu, Y. Zheng, T. Song, K. Davey, U. Paik, J. Dong, S.-Z. Qiao, *Nat. Commun.* **2023**, *14*, 354.
[96] J. Ke, W. Zhu, Y. Ji, J. Chen, C. Li, Y. Wang, Q. Wang, W. H. Huang, Z. Hu, Y. Li, Q. Shao, J. Lu, *Angew. Chem., Int. Ed.* **2025**, *64*, 202422740.
[97] S. Dong, P. Wang, Z. Li, L. Wei, S. Liu, Y. Yang, F. Zheng, *Adv. Funct. Mater.* **2025**, *35*, 2422166.
[98] L. Wu, W. Huang, D. Li, H. Jia, B. Zhao, J. Zhu, H. Zhou, W. Luo, *Angew. Chem., Int. Ed.* **2025**, *64*, 202413334.
[99] Z.-Y. Wu, F.-Y. Chen, B. Li, S.-W. Yu, Y. Z. Finfrock, D. M. Meira, Q.-Q. Yan, P. Zhu, M.-X. Chen, T.-W. Song, Z. Yin, H.-W. Liang, S. Zhang, G. Wang, H. Wang, *Nat. Mater.* **2023**, *22*, 100.
[100] Z. Yang, Y. Ding, W. Chen, S. Luo, D. Cao, X. Long, L. Xie, X. Zhou, X. Cai, K. Liu, X. Z. Fu, J. L. Luo, *Adv. Mater.* **2025**, *37*, 2417777.
[101] J. Tang, Q. Zeng, Q. Jiang, H. Wang, S. Hu, Y. Ji, H. Zeng, C. Liu, H.-J. Peng, X. Li, T. Zheng, C.-W. Pao, X. Liu, C. Xia, *Chem Catalysis* **2025**, *5*, 101441.
[102] X. Jiang, J. Zhu, M. Jiang, P. Zhang, W. Wen, W. Cai, Y. Ding, P. Sun, M. Cao, *Adv. Mater.* **2025**, *37*, 2503354.
[103] X. Ma, M. Liu, Q. Li, X. Xiao, J. Liu, X. Xu, Y. Yin, P. Qiao, L. Zhang, X. Zou, R. Wang, B. Jiang, *J. Mater. Chem. A* **2023**, *11*, 16889.
[104] J. Wang, H. Yang, F. Li, L. Li, J. Wu, S. Liu, T. Cheng, Y. Xu, Q. Shao, X. Huang, *Sci. Adv.* **2022**, *8*, abl9271.
[105] X. Cao, L. Miao, W. Jia, H. Qin, G. Lin, R. Ma, T. Jin, L. Jiao, *Nat. Commun.* **2025**, *16*, 3976.
[106] H. Liu, Z. Zhang, J. Fang, M. Li, M. G. Sendeku, X. Wang, H. Wu, Y. Li, J. Ge, Z. Zhuang, D. Zhou, Y. Kuang, X. Sun, *Joule* **2023**, *7*, 558.
[107] L. Zhang, H. Jang, H. Liu, M. G. Kim, D. Yang, S. Liu, X. Liu, J. Cho, *Angew. Chem.* **2021**, *133*, 18969.

[108] R. Li, J. Liu, M. Xiao, Y. Sun, F. Liu, J. Gan, S. Gao, *Small* **2024**, *20*, 2400095.
[109] Y. Wang, R. Ma, Z. Shi, H. Wu, S. Hou, Y. Wang, C. Liu, J. Ge, W. Xing, *Chem* **2023**, *9*, 2931.
[110] D. Jeon, D. Y. Kim, H. Kim, N. Kim, C. Lee, D. H. Seo, J. Ryu, *Adv. Mater.* **2024**, *36*, 2304468.
[111] J. Chen, Y. Ma, C. Cheng, T. Huang, R. Luo, J. Xu, X. Wang, T. Jiang, H. Liu, S. Liu, T. Huang, L. Zhang, W. Chen, *J. Am. Chem. Soc.* **2025**, *147*, 8720.
[112] F.-F. Zhang, C.-Q. Cheng, J.-Q. Wang, L. Shang, Y. Feng, Y. Zhang, J. Mao, Q.-J. Guo, Y.-M. Xie, C.-K. Dong, Y.-H. Cheng, H. Liu, X.-W. Du, *ACS Energy Lett.* **2021**, *6*, 1588.
[113] L. Deng, S.-F. Hung, S. Liu, S. Zhao, Z.-Y. Lin, C. Zhang, Y. Zhang, A.-Y. Wang, H.-Y. Chen, J. Peng, R. Ma, L. Jiao, F. Hu, L. Li, S. Peng, *J. Am. Chem. Soc.* **2024**, *146*, 23146.
[114] D. Chen, S. Mu, *Adv. Mater.* **2024**, *36*, 2408285.
[115] X. Cheng, S. Yin, J. Zhang, J. Yang, L. Chen, W. Wang, H. Liao, R. Huang, Y. Jiang, B. Zhang, S. Sun, *Adv. Mater.* **2025**, *37*, 2501707.
[116] T. Zhang, Q. Liu, H. Bao, M. Wang, N. Wang, B. Zhang, H. J. Fan, *Nat. Commun.* **2025**, *16*, 1037.
[117] Y. Liu, Y. Wang, H. Li, M. G. Kim, Z. Duan, K. Talat, J. Y. Lee, M. Wu, H. Lee, *Nat. Commun.* **2025**, *16*, 1717.
[118] C. Zheng, B. Huang, X. Liu, H. Wang, L. Guan, *Inorg. Chem. Front.* **2024**, *11*, 1912.
[119] S. Kaushik, D. Wu, Z. Zhang, X. Xiao, C. Zhen, W. Wang, N.-Y. Huang, M. Gu, Q. Xu, *Adv. Mater.* **2024**, *36*, 2401163.
[120] Y. Yuan, H. Fang, K. Chen, J. Huang, J. Chen, Z. Lu, H. Wang, Z. Zhao, W. Chen, Z. Wen, *Adv. Mater.* **2025**, *37*, 2501607.
[121] L. Hou, Z. Li, H. Jang, Y. Wang, X. Cui, X. Gu, M. G. Kim, L. Feng, S. Liu, X. Liu, *Adv. Energy Mater.* **2023**, *13*, 2300177.
[122] Z. L. Zhao, Q. Wang, X. Huang, Q. Feng, S. Gu, Z. Zhang, H. Xu, L. Zeng, M. Gu, H. Li, *Energy Environ. Sci.* **2020**, *13*, 5143.
[123] S. Song, J. Zhou, S. Zhang, L. Zhang, J. Li, Y. Wang, L. Han, Y. Long, Z. Hu, J.-Q. Wang, *Nano Res.* **2018**, *11*, 4796.
[124] C. Fan, X. Gao, P. Tang, Q. Wang, B. Li, *Adv. Sci.* **2025**, *12*, 2410784.
[125] S. S. Jeon, H. Jeon, J. Lee, R. Haaring, W. Lee, J. Nam, S. J. Cho, H. Lee, *ACS Catal.* **2025**, *15*, 4963.
[126] Y. Wang, L. Li, M. Shen, R. Tang, J. Zhou, L. Han, X. Zhang, L. Zhang, G. Kim, J.-Q. Wang, *Adv. Sci.* **2023**, *10*, 2303693.
[127] X. Li, G. Chen, Y. Liu, R. Lu, C. Ma, Z. Wang, Y. Han, D. Wang, *Energy Environ. Sci.* **2025**, *18*, 4200.
[128] Y. Wu, Y. Liu, K. Liu, L. Wang, L. Zhang, D. Wang, Z. Chai, W. Shi, *Green Energy Environ.* **2022**, *7*, 799.
[129] D. Chen, R. Yu, H. Zhao, J. Jiao, X. Mu, J. Yu, S. Mu, *Angew. Chem., Int. Ed.* **2024**, *63*, 202407577.
[130] D. Chen, R. Yu, K. Yu, R. Lu, H. Zhao, J. Jiao, Y. Yao, J. Zhu, J. Wu, S. Mu, *Nat. Commun.* **2024**, *15*, 3928.
[131] Y. Shi, Z. Lyu, M. Zhao, R. Chen, Q. N. Nguyen, Y. Xia, *Chem. Rev.* **2021**, *121*, 649.
[132] N. Kumada, *J. Ceram. Soc. Jpn.* **2013**, *121*, 135.
[133] G. C. Moss, T. Binninger, Z. S. H. S. Rajan, B. J. Itota, P. J. Kooyman, D. Susac, R. Mohamed, *Small* **2025**, *21*, 2412237.
[134] A. D. Bertelsen, M. Kløve, N. L. N. Broge, M. Bondesgaard, R. B. Stubkjær, A.-C. Dippel, Q. Li, R. Tilley, M. R. Vogel Jørgensen, B. B. Iversen, *J. Am. Chem. Soc.* **2024**, *146*, 23729.
[135] Y. Xiong, Y. Xia, *Adv. Mater.* **2007**, *19*, 3385.
[136] K. D. Gilroy, A. Ruditskiy, H.-C. Peng, D. Qin, Y. Xia, *Chem. Rev.* **2016**, *116*, 10414.
[137] Q. Ji, B. Tang, X. Zhang, C. Wang, H. Tan, J. Zhao, R. Liu, M. Sun, H. Liu, C. Jiang, J. Zeng, X. Cai, W. Yan, *Nat. Commun.* **2024**, *15*, 8089.
[138] K. Zhou, H. Liu, Z. Liu, X. Li, N. Wang, M. Wang, T. Xue, Y. Shen, H. Li, H. Li, C. Li, *Angew. Chem., Int. Ed.* **2025**, *64*, 202422707.
[139] B. Yuan, Q. Dang, H. Liu, M. G. Sendeku, J. Peng, Y. Fan, L. Cai, A. Cao, S. Chen, H. Li, Y. Kuang, F. Wang, X. Sun, *Nat. Commun.* **2025**, *16*, 4583.
[140] H. Choi, Ji Choi, H. Choi, G. Na, J. Lee, S.-Y. Kim, J. Kim, Y. Shin, Y.-H. Cho, Y.-E. Sung, *ChemElectroChem* **2025**, *12*, 202400682.
[141] W. Zhou, J. Xu, Z. Sun, C. Zhang, P. Zhou, H. Qin, Y. Lian, Y. Su, J. Bai, *Nano Res.* **2025**, *18*, 94907524.
[142] N. Wen, Y. Xia, H. Wang, D. Zhang, H. Wang, X. Wang, X. Jiao, D. Chen, *Adv. Sci.* **2022**, *9*, 2200529.
[143] Q. Hong, Y. Wang, R. Wang, Z. Chen, H. Yang, K. Yu, Y. Liu, H. Huang, Z. Kang, P. W. Menezes, *Small* **2023**, *19*, 2206723.
[144] J. Li, X. He, Y. Du, M. Jiang, Q. Hu, J. Yin, F. Yang, J. Zhang, *Chem. Eng. J.* **2023**, *475*, 146183.
[145] R. Deng, F. Liu, S. Gao, Z. Xia, R. Wu, J. Kong, J. Yang, J. Wen, X. Zhang, C. Lv, Y. Wang, X. Li, Z. Wang, *ACS Catal.* **2025**, *15*, 1782.
[146] Y.-K. Lv, K. Wang, W.-Y. Sun, P. Peng, S.-Q. Zang, *Adv. Sci.* **2023**, *10*, 2304656.
[147] Y. Wang, M. Wei, Q. Ding, H. Li, W. Ma, *Nano Lett.* **2024**, *24*, 4733.
[148] S. Shen, L. Zhao, J. Zhang, *Frontiers in Energy* **2022**, *16*, 537.
[149] Y. Yao, Z. Huang, P. Xie, S. D. Lacey, R. J. Jacob, H. Xie, F. Chen, A. Nie, T. Pu, M. Rehwoldt, D. Yu, M. R. Zachariah, C. Wang, R. Shahbazian-Yassar, J. Li, L. Hu, *Science* **2018**, *359*, 1489.
[150] Y. Yao, Z. Huang, P. Xie, L. Wu, L. Ma, T. Li, Z. Pang, M. Jiao, Z. Liang, J. Gao, Y. He, D. J. Kline, M. R. Zachariah, C. Wang, J. Lu, T. Wu, T. Li, C. Wang, R. Shahbazian-Yassar, L. Hu, *Nat. Nanotechnol.* **2019**, *14*, 851.
[151] C. Wan, X. Duan, *Matter* **2019**, *1*, 555.
[152] X. Hu, D. Zuo, S. Cheng, S. Chen, Y. Liu, W. Bao, S. Deng, S. J. Harris, J. Wan, *Chem. Soc. Rev.* **2023**, *52*, 1103.
[153] B. Zhou, K. Liu, K. Yu, Q. Zhou, Y. Gao, X. Gao, Z. Chen, W. Chen, P. Chen, *Small* **2025**, 2501917.
[154] K. M. Wyss, D. X. Luong, J. M. Tour, *Adv. Mater.* **2022**, *34*, 2106970.
[155] N. Fu, X. Liang, X. Wang, T. Gan, C. Ye, Z. Li, J.-C. Liu, Y. Li, *J. Am. Chem. Soc.* **2023**, *145*, 9540.
[156] H. Yuan, D. Jiang, Z. Li, X. Liu, Z. Tang, X. Zhang, L. Zhao, M. Huang, H. Liu, K. Song, W. Zhou, *Adv. Mater.* **2024**, *36*, 2305375.
[157] B. Wang, X. Zhu, X. Pei, W. Liu, Y. Leng, X. Yu, C. Wang, L. Hu, Q. Su, C. Wu, Y. Yao, Z. Lin, Z. Zou, *J. Am. Chem. Soc.* **2023**, *145*, 13788.
[158] N. Zhang, X. Liu, H. Zhong, W. Liu, D. Bao, J. Zeng, D. Wang, C. Ma, X. Zhang, *Angew. Chem., Int. Ed.* **2025**, *64*, 202503246.
[159] X. Wang, H. Zhong, S. Xi, W. S. V. Lee, J. Xue, *Adv. Mater.* **2022**, *34*, 2107956.
[160] L. An, C. Wei, M. Lu, H. Liu, Y. Chen, G. G. Scherer, A. C. Fisher, P. Xi, Z. J. Xu, C.-H. Yan, *Adv. Mater.* **2021**, *33*, 2006328.
[161] Y. Shen, X.-L. Zhang, M.-R. Qu, J. Ma, S. Zhu, Y.-L. Min, M.-R. Gao, S.-H. Yu, *Nat. Commun.* **2024**, *15*, 7861.
[162] G.-Y. Xu, M.-F. Yue, Z.-X. Qian, Z.-Y. Du, X.-Q. Xie, W.-P. Chen, Y.-J. Zhang, J.-F. Li, *J. Mater. Chem. A* **2023**, *11*, 15204.
[163] H. Y. Lin, W. J. Li, M. Y. Lin, H. G. Xu, S. R. Fang, Y. Lv, W. Li, J. Guo, H. Q. Fu, H. Y. Yuan, C. Sun, S. Dai, P. F. Liu, H. G. Yang, *Angew. Chem., Int. Ed.* **2025**, *64*, 202504212.
[164] D. Leybo, U. J. Etim, M. Monai, S. R. Bare, Z. Zhong, C. Vogt, *Chem. Soc. Rev.* **2024**, *53*, 10450.
[165] H.-S. Oh, H. N. Nong, T. Reier, A. Bergmann, M. Gliech, J. Ferreira de Araújo, E. Willinger, R. Schlögl, D. Teschner, P. Strasser, *J. Am. Chem. Soc.* **2016**, *138*, 12552.
[166] X. Jiang, J. Zhu, M. Jiang, P. Zhang, W. Wen, W. Cai, Y. Ding, P. Sun, M. Cao, *Adv. Mater.* **2025**, *37*, 2503354.
[167] J. Wang, H. Yang, F. Li, L. Li, J. Wu, S. Liu, T. Cheng, Y. Xu, Q. Shao, X. Huang, *Sci. Adv.* **2022**, *8*, abl9271.
[168] X. Cao, L. Miao, W. Jia, H. Qin, G. Lin, R. Ma, T. Jin, L. Jiao, *Nat. Commun.* **2025**, *16*, 6217.

[169] L. Zhang, H. Jang, H. Liu, M. G. Kim, D. Yang, S. Liu, X. Liu, J. Cho, *Angew. Chem., Int. Ed.* **2021**, *60*, 18821.
[170] M. Wang, Z. Wang, X. Li, X. Sun, H. Huang, H. Chen, H. Luo, L. Li, X. Zou, X. Zhao, *Adv. Mater.* **2025**, 11461.
[171] H. Li, Y. Pan, L. Wu, R. He, Z. Qin, S. Luo, L. Yang, J. Zeng, *Mol. Catal.* **2023**, *551*, 113619.
[172] H. Lv, S. Wang, J. Li, C. Shao, W. Zhou, X. Shen, M. Xue, C. Zhang, *Appl. Surf. Sci.* **2020**, *514*, 145943.
[173] S. Ramesh, K. Karuppasamy, A. Sivasamy, H.-S. Kim, H. M. Yadav, H. S. Kim, *J. Alloys Compd.* **2021**, *877*, 160297.
[174] W. Ma, L. Zhou, X. Wang, Q. Li, X. Lv, J. Dang, *Adv. Energy Mater.* **2025**, *15*, 2502367.
[175] J. Li, X. Yu, W.-H. Huang, Q. Zhang, K. Wei, X. Zhou, Y. Zhu, X. Zhong, M.-H. Yeh, N. Alonso-Vante, J. Ma, *Angew. Chem., Int. Ed.* **2025**, *64*, 202511750.
[176] Z.-H. Xue, J. Mahmood, Y. Shang, G. Li, S.-J. Kim, Y. Han, C. T. Yavuz, *J. Am. Chem. Soc.* **2025**, *147*, 17839.
[177] H. Ooka, J. Huang, K. S. Exner, *Front. Energy Res.* **2021**, *9*, 2021.
[178] C. F. Dickens, J. H. Montoya, A. R. Kulkarni, M. Bajdich, J. K. Nørskov, *Surf. Sci.* **2019**, *681*, 122.
[179] E. Knözinger, *Zeitschrift für Physikalische Chemie* **1998**, *206*, 281.
[180] S. Chen, H. Huang, P. Jiang, K. Yang, J. Diao, S. Gong, S. Liu, M. Huang, H. Wang, Q. Chen, *ACS Catal.* **2020**, *10*, 1152.
[181] X. Yang, W. Song, K. Liao, X. Wang, X. Wang, J. Zhang, H. Wang, Y. Chen, N. Yan, X. Han, J. Ding, W. Hu, *Nat. Commun.* **2024**, *15*, 8216.
[182] J. Shan, C. Guo, Y. Zhu, S. Chen, L. Song, M. Jaroniec, Y. Zheng, S.-Z. Qiao, *Chem* **2019**, *5*, 445.
[183] J. Wang, L. Han, B. Huang, Q. Shao, H. L. Xin, X. Huang, *Nat. Commun.* **2019**, *10*, 5692.
[184] Z. Hou, C. Cui, Y. Li, Y. Gao, D. Zhu, Y. Gu, G. Pan, Y. Zhu, T. Zhang, *Adv. Mater.* **2023**, *35*, 2209876.
[185] Y. Qin, T. Yu, S. Deng, X.-Y. Zhou, D. Lin, Q. Zhang, Z. Jin, D. Zhang, Y.-B. He, H.-J. Qiu, L. He, F. Kang, K. Li, T.-Y. Zhang, *Nat. Commun.* **2022**, *13*, 3784.
[186] C. Guan, X. Yue, Q. Xiang, *Adv. Mater.* **2025**, *37*, 2501209.
[187] Y. Liao, R. He, W. Pan, Y. Li, Y. Wang, J. Li, Y. Li, *Chem. Eng. J.* **2023**, *464*, 142669.
[188] H. Wang, Q. He, X. Gao, Y. Shang, W. Zhu, W. Zhao, Z. Chen, H. Gong, Y. Yang, *Adv. Mater.* **2024**, *36*, 2305453.
[189] W. Cheng, X. Zhao, H. Su, F. Tang, W. Che, H. Zhang, Q. Liu, *Nat. Energy* **2019**, *4*, 115.
[190] M. Tu, Z. Zhu, Y. He, S. Mathi, J. Deng, M. Naushad, Y. Huang, Y. wen Hu, M. S. Balogun, *Small* **2025**, *21*, 2500687.
[191] Q. Ji, Y. Kong, C. Wang, H. Tan, H. Duan, W. Hu, G. Li, Y. Lu, N. Li, Y. Wang, J. Tian, Z. Qi, Z. Sun, F. Hu, W. Yan, *ACS Catal.* **2020**, *10*, 5691.
[192] X. Du, Y. Sun, J. Cui, C. Wu, X. Yang, X. Chen, H. Tao, L. Liu, J. Ye, *Adv. Funct. Mater.* **2025**, *35*, 2506203.
[193] X. Ping, Y. Liu, L. Zheng, Y. Song, L. Guo, S. Chen, Z. Wei, *Nat. Commun.* **2024**, *15*, 2501.
[194] Y. Wan, W. Wei, L. Li, L. Wu, H. Qin, X. Yuan, *Small* **2025**, *21*, 2502039.
[195] Y.-J. Mao, F. Liu, Y.-H. Chen, X. Jiang, X.-S. Zhao, T. Sheng, J.-Y. Ye, H.-G. Liao, L. Wei, S.-G. Sun, *J. Mater. Chem. A* **2021**, *9*, 26277.
[196] R. R. Rao, M. J. Kolb, L. Giordano, A. F. Pedersen, Y. Katayama, J. Hwang, A. Mehta, H. You, J. R. Lunger, H. Zhou, N. B. Halck, T. Vegge, I. Chorkendorff, I. E. L. Stephens, Y. Shao-Horn, **2020**, *3*, 516.
[197] K. Klyukin, A. Zagalskaya, V. Alexandrov, *J. Phys. Chem. C* **2019**, *123*, 22151.
[198] Y. Wang, X. Lei, B. Zhang, B. Bai, P. Das, T. Azam, J. Xiao, Z.-S. Wu, *Angew. Chem., Int. Ed.* **2024**, *63*, 202316903.
[199] L. Li, G. Zhang, J. Xu, H. He, B. Wang, Z. Yang, S. Yang, *Adv. Funct. Mater.* **2023**, *33*, 2213304.
[200] L. Li, X. Cao, J. Huo, J. Qu, W. Chen, C. Liu, Y. Zhao, H. Liu, G. Wang, *J. Energy Chem.* **2023**, *76*, 195.
[201] A. Grimaud, O. Diaz-Morales, B. Han, W. T. Hong, Y.-L. Lee, L. Giordano, K. A. Stoerzinger, M. T. M. Koper, Y. Shao-Horn, *Nat. Chem.* **2017**, *9*, 457.
[202] Y. Xue, J. Zhao, L. Huang, Y.-R. Lu, A. Malek, G. Gao, Z. Zhuang, D. Wang, C. T. Yavuz, X. Lu, *Nat. Commun.* **2023**, *14*, 8093.
[203] C. Liu, B. Sheng, Q. Zhou, D. Cao, H. Ding, S. Chen, P. Zhang, Y. Xia, X. Wu, L. Song, *Nano Res.* **2022**, *15*, 7008.
[204] J. Kuang, B. Deng, Z. Jiang, Y. Wang, Z.-J. Jiang, *Adv. Mater.* **2024**, *36*, 2306934.
[205] J. Ruiz Esquius, D. J. Morgan, G. Algara Siller, D. Gianolio, M. Aramini, L. Lahn, O. Kasian, S. A. Kondrat, R. Schlögl, G. J. Hutchings, R. Arrigo, S. J. Freakley, *J. Am. Chem. Soc.* **2023**, *145*, 6398.
[206] J. Kim, P.-C. Shih, K.-C. Tsao, Y.-T. Pan, X. Yin, C.-J. Sun, H. Yang, *J. Am. Chem. Soc.* **2017**, *139*, 12076.
[207] A. Oh, H. Y. Kim, H. Baik, B. Kim, N. K. Chaudhari, S. H. Joo, K. Lee, *Adv. Mater.* **2019**, *31*, 1805546.
[208] N. Deka, T. E. Jones, L. J. Falling, L.-E. Sandoval-Diaz, T. Lunkenbein, J.-J. Velasco-Velez, T.-S. Chan, C.-H. Chuang, A. Knop-Gericke, R. V. Mom, *ACS Catal.* **2023**, *13*, 7488.
[209] Y. Chen, H. Li, J. Wang, Y. Du, S. Xi, Y. Sun, M. Sherburne, J. W. Ager, A. C. Fisher, Z. J. Xu, *Nat. Commun.* **2019**, *10*, 572.
[210] N. Zhang, X. Feng, D. Rao, X. Deng, L. Cai, B. Qiu, R. Long, Y. Xiong, Y. Lu, Y. Chai, *Nat. Commun.* **2020**, *11*, 4066.
[211] Y. a. Zhu, F. Wu, X. Zhang, Y. Lin, L. Zhang, T.-S. Chan, Q. Zhang, L. Chen, *Adv. Mater.* **2025**, *37*, 2500449.
[212] T. Takashima, K. Ishikawa, H. Irie, *ACS Catal.* **2019**, *9*, 9212.
[213] M. Liu, N. Li, X. Wang, J. Zhao, D.-C. Zhong, W. Li, X.-H. Bu, *Angew. Chem., Int. Ed.* **2023**, *62*, 202300507.
[214] L. Bai, S. Lee, X. Hu, *Angew. Chem., Int. Ed.* **2021**, *60*, 3095.
[215] J. Wang, C. Cheng, Q. Yuan, H. Yang, F. Meng, Q. Zhang, L. Gu, J. Cao, L. Li, S.-C. Haw, Q. Shao, L. Zhang, T. Cheng, F. Jiao, X. Huang, *Chem* **2022**, *8*, 1673.
[216] W. Hu, B. Huang, M. Sun, J. Du, Y. Hai, W. Yin, X. Wang, W. Gao, C. Zhao, Y. Yue, Z. Li, C. Li, *Adv. Mater.* **2025**, *37*, 2411709.
[217] G. Wan, J. W. Freeland, J. Kloppenburg, G. Petretto, J. N. Nelson, D.-Y. Kuo, C.-J. Sun, J. Wen, J. T. Diulus, G. S. Herman, Y. Dong, R. Kou, J. Sun, S. Chen, K. M. Shen, D. G. Schlom, G.-M. Rignanese, G. Hautier, D. D. Fong, Z. Feng, H. Zhou, J. Suntivich, *Sci. Adv.* **2021**, *7*, abc7323.
[218] Z.-F. Huang, J. Song, Y. Du, S. Xi, S. Dou, J. M. V. Nsanzimana, C. Wang, Z. J. Xu, X. Wang, *Nat. Energy* **2019**, *4*, 329.
[219] L. Deng, S.-F. Hung, S. Liu, S. Zhao, Z.-Y. Lin, C. Zhang, Y. Zhang, A.-Y. Wang, H.-Y. Chen, J. Peng, R. Ma, L. Jiao, F. Hu, L. Li, S. Peng, *J. Am. Chem. Soc.* **2024**, *146*, 23146.
[220] J. Wang, *Chem* **2023**, *9*, 1645.
[221] C. Lin, J.-L. Li, X. Li, S. Yang, W. Luo, Y. Zhang, S.-H. Kim, D.-H. Kim, S. S. Shinde, Y.-F. Li, Z.-P. Liu, Z. Jiang, J.-H. Lee, *Nat. Catal.* **2021**, *4*, 1012.
[222] F. Song, M. M. Busch, B. Lassalle-Kaiser, C.-S. Hsu, E. Petkucheva, M. Bensimon, H. M. Chen, C. Corminboeuf, X. Hu, *ACS Cent. Sci.* **2019**, *5*, 558.
[223] J. Chang, Y. Shi, H. Wu, J. Yu, W. Jing, S. Wang, G. I. N. Waterhouse, Z. Tang, S. Lu, *J. Am. Chem. Soc.* **2024**, *146*, 12958.
[224] L. Deng, H. Chen, S.-F. Hung, Y. Zhang, H. Yu, H.-Y. Chen, L. Li, S. Peng, *J. Am. Chem. Soc.* **2024**, *146*, 35438.
[225] L. Wu, W. Huang, D. Li, B. Zhao, H. Zhou, W. Luo, *Angew. Chem., Int. Ed.* **2025**, *64*, 202420848.
[226] Y.-H. Wang, S. Zheng, W.-M. Yang, R.-Y. Zhou, Q.-F. He, P. Radjenovic, J.-C. Dong, S. Li, J. Zheng, Z.-L. Yang, G. Attard, F. Pan, Z.-Q. Tian, J.-F. Li, *Nature* **2021**, *600*, 81.

[227] P. Li, Y. Jiang, Y. Hu, Y. Men, Y. Liu, W. Cai, S. Chen, *Nat. Catal.* **2022**, *5*, 900.
[228] X. Chen, X.-T. Wang, J.-B. Le, S.-M. Li, X. Wang, Y.-J. Zhang, P. Radjenovic, Y. Zhao, Y.-H. Wang, X.-M. Lin, J.-C. Dong, J.-F. Li, *Nat. Commun.* **2023**, *14*, 5289.
[229] C.-Y. Li, J.-B. Le, Y.-H. Wang, S. Chen, Z.-L. Yang, J.-F. Li, J. Cheng, Z.-Q. Tian, *Nat. Mater.* **2019**, *18*, 697.
[230] L.-F. Shen, B.-A. Lu, Y. Li, J. Liu, Z. Huang-fu, H. Peng, J.-Y. Ye, X.-M. Qu, J.-M. Zhang, *Angew. Chem., Int. Ed.* **2020**, *59*, 22397.
[231] Y. Ping, R. J. Nielsen, W. A. Goddard, *J. Am. Chem. Soc.* **2017**, *139*, 149.
[232] Q. Wen, J. Duan, W. Wang, D. Huang, Y. Liu, Y. Shi, J. Fang, A. Nie, H. Li, T. Zhai, *Angew. Chem., Int. Ed.* **2022**, *61*, 202206077.
[233] R. Verduci, F. Creazzo, F. Tavella, S. Abate, C. Ampelli, S. Luber, S. Perathoner, G. Cassone, G. Centi, D'G. Angelo, *J. Am. Chem. Soc.* **2024**, *146*, 18061.
[234] Y. Chen, C. Liu, J. Xu, C. Xia, P. Wang, B. Y. Xia, Y. Yan, X. Wang, *Small Struct.* **2023**, *4*, 2200130.
[235] X. Li, Y. Yao, Y. Tian, J. Jia, W. Ma, X. Yan, J. Liang, *Mater. Chem. Front.* **2024**, *8*, 2493.
[236] Q. Feng, X. Z. Yuan, G. Liu, B. Wei, Z. Zhang, H. Li, H. Wang, *J. Power Sources* **2017**, *366*, 33.
[237] C. Qiu, Z. Xu, F.-Y. Chen, H. Wang, *ACS Catal.* **2024**, *14*, 921.
[238] L. Wang, R. Du, Z. Zhao, M. Na, X. Li, X. Zhao, X. Wang, Y. A. Wu, S. Jana, Y. Zou, H. Chen, X. Zou, *Angew. Chem., Int. Ed.* **2025**, *64*, 202501744.
[239] J. K. Lee, F. Babbe, G. Wang, A. W. Tricker, R. Mukundan, A. Z. Weber, X. Peng, *Joule* **2024**, *8*, 2357.
[240] C. Liu, J. A. Wrubel, E. Padgett, G. Bender, *Appl. Energy* **2024**, *356*, 122274.
[241] C. Liu, M. Carmo, G. Bender, A. Everwand, T. Lickert, J. L. Young, T. Smolinka, D. Stolten, W. Lehnert, *Electrochem. Commun.* **2018**, *97*, 96.
[242] Z. Fan, H. Yu, G. Jiang, D. Yao, S. Sun, J. Chi, B. Qin, Z. Shao, *Int. J. Hydrogen Energy* **2022**, *47*, 18963.
[243] H. Ito, T. Maeda, A. Nakano, A. Kato, T. Yoshida, *Electrochim. Acta* **2013**, *100*, 242.
[244] X. Song, P. Pei, Z. Wang, P. Ren, X. Pu, Z. Lei, H. Wang, *Appl. Energy* **2025**, *401*, 126793.
[245] Z. Kang, T. Schuler, Y. Chen, M. Wang, F.-Y. Zhang, G. Bender, *Electrochim. Acta* **2022**, *429*, 140942.
[246] G. Mirshekari, R. Ouimet, Z. Zeng, H. Yu, S. Bliznakov, L. Bonville, A. Niedzwiecki, C. Capuano, K. Ayers, R. Maric, *Int. J. Hydrogen Energy* **2021**, *46*, 1526.
[247] M. Bernt, A. Hartig-Weiß, M. F. Tovini, H. A. El-Sayed, C. Schramm, J. Schröter, C. Gebauer, H. A. Gasteiger, *Chem. Ing. Tech.* **2020**, *92*, 31.
[248] R. J. Ouimet, J. R. Glenn, D. De Porcellinis, A. R. Motz, M. Carmo, K. E. Ayers, *ACS Catal.* **2022**, *12*, 6159.
[249] K. J. Ferner, S. Litster, *ACS Appl. Energy Mater.* **2024**, *7*, 8124.
[250] L. Tao, F. Lv, D. Wang, H. Luo, F. Lin, H. Gong, H. Mi, S. Wang, Q. Zhang, L. Gu, M. Luo, S. Guo, *Joule* **2024**, *8*, 450.
[251] Y. Yang, S. Louisia, S. Yu, J. Jin, I. Roh, C. Chen, M. V. Fonseca Guzman, J. Feijóo, P.-C. Chen, H. Wang, C. J. Pollock, X. Huang, Y.-T. Shao, C. Wang, D. A. Muller, H. D. Abruña, P. Yang, *Nature* **2023**, *614*, 262.
[252] P. Tukur, Y. Wei, Y. Zhang, H. Chen, Y. Lin, S. He, Y. Mo, J. Wei, *Small* **2025**, *21*, 2501946.
[253] Y. Lun, H. Chen, K. Wang, S. Song, Y. Wang, *Adv. Energy Mater.* **2025**, *15*, 2405657.

Qisheng Zeng obtained his B.S. from the University of Electronic Science and Technology of China in 2024 and subsequently worked there as a Research Assistant for one year. He is currently a Ph.D. student in the Department of Chemistry at the Chinese University of Hong Kong. He focuses on developing advanced electrocatalysts for oxygen evolution reaction (OER).

Jialin Tang is an Assistant Professor of Materials and Energy at the University of Electronic Science and Technology of China (UESTC). She obtained her Ph.D. in the University of Electronic Science and Technology of China. Her research interests include water electrolysis and the rational design of the oxygen evolution reaction (OER) electrocatalysts in acidic environment. She secured and led research grants from the National Natural Science Foundation of China (NSFC) Young Scientists Fund and the Sichuan Provincial Natural Science Foundation's Young Scientists Program.

Yuan Ji obtained his B.S. and master degree from Sichuan University in 2019 and 2022 respectively. He is currently pursuing his Ph.D. in Professor Chuan Xia's team at the University of Electronic Science and Technology of China. His research interests include waste plastic recycling and electrosynthesis of small moleculars.

Qiu Jiang is an associate professor in the School of Materials and Energy at the University of Electronic Science and Technology of China (UESTC). He obtained his Ph.D. at King Abdullah University of Science and Technology, Saudi Arabia. He is interested in developing functional nanomaterials for energy storage and conversion applications. He led research grants from the National Natural Science Foundation of China (NSFC) Young Scientists Fund and the Sichuan Provincial Natural Science Foundation's Young Scientists Program.

Chuan Xia is a Professor in the School of Energy and Materials at University of Electronic Science and Technology of China. His pioneering research focuses on the sustainable production of chemicals from CO_2. Over the past five years, he has published over 30 articles in prestigious journals such as Science and Nature Catalysis, and has been recognized as a Highly Cited Researcher in 2023–2024. His work was selected as China's Top 10 Scientific Advances (2022). He is also a recipient of the DAMO Academy Young Fellow (2024) and the CCS Young Chemist Award (2023). Group website: https://www.chuan-lab.com.